Order Number 9000072

Positronium reflection

Weber, Marc Herbert, Ph.D.

City University of New York, 1989

U·M·I
300 N. Zeeb Rd.
Ann Arbor, MI 48106

Positronium Reflection

by

Marc H. Weber

A dissertation submitted to the Graduate Faculty in Physics in partial fulfillment of the requirements for the degree of Doctor of Philosophy, The City University of New York.

1989

This manuscript has been read and accepted for the Graduate Faculty in Physics in satisfaction of the dissertation requirement for the degree of Doctor of Philosophy.

November 1, 1988
Date

Leonard O. Roellig
Chair of Examining Committee

Nov. 2, 1988
Date

Joel I. Gersten
Executive Officer

Marten L. den Boer

Karl F. Canter

Kelvin G. Lynn

Frederick W. Smith

Narkis Tzoar

Supervisory Committee

The City University of New York

Abstract

Positronium Reflection

by

Marc H. Weber

Advisor: Professor L.O. Roellig

A high intensity positron beam has been used to create a beam of monoenergetic positronium (Ps) atoms. The Ps beam was directed at surfaces to measure to measure the reflected fraction of Ps. The positron beam was based on ^{63}Cu irradiated with thermal neutrons in the High Flux Beam Reactor at Brookhaven National Laboratory to obtain the β^+ emitting isotope ^{64}Cu. Prepared as a single crystal the copper source also functions as the moderator for the positrons. The beam is accelerated and guided magnetically to a differentially pumped gas cell filled with $10^{-3} torr$ Ar. Positrons pick up electrons from the gas atoms to form a beam of Ps. The differential cross section is strongly forward directed. With the additional help of collimators a monoenergetic beam of Ps emanates from the cell. The Ps beam was scattered from a single crystal of LiF(100) and the reflected Ps fraction was observed as a function of the scattering angle as well as the Ps beam energy. A strong specularly reflected peak was observed. Below $8eV$ as much as 29% of the incident beam is reflected when the sample is heated to about $160°C$. At higher energies up to $56eV$ between 1% and 3% are reflected specularly. This thesis represents the first measurement of Ps reflection from a surface and is a major stepping stone towards the investigation of low energy Ps diffraction from ordered solid surfaces. Important new insights about surface structures can be expected from such a new probe.

Acknowledgement

I am indebted to many people without who I would not have succeeded with this thesis project. I sincerely appreciate the great effort by Professor L.O. Roellig that he invested in my education and direction. The insightful comments by and discussions with K.G. Lynn, K.F. Canter, A.P. Mills, Jr., and S. Berko will always be remembered. I am grateful for their concern with my progress in the project as well as for my welfare. B.L. Brown built the gas cell system and tested it. I was able to benefit from his experience with positrons in gasses. This work would have been impossible without the support of J.J. Hurst, A.R. Moodenbaugh, and A.J. Viescas which often went beyond the call of duty. Donuts during early Sunday morning sessions will always be gratefully remembered, Jim. J. Rutherford has taught me the first steps in work with UHV equipment. Thanks are extended to J. Zahradka who worked hard to keep the positron beam running and even improve upon it. When Jeff left the project M. Carroll took over some of his tasks. Instrumental was the support of the reactor staff and D. Rorer and T. Holmquist in particular. They would go through great length to accommodate my experimental needs. I appreciate the much needed pep talks by my friends who carried me through setbacks and endured all my moods. F. Frankl made my stay in New York a pleasant one. I wish to extend many thanks to J. Mulert and his staff from the Fulbright Commission in Bonn. They made my dream of studying abroad come true. Thanks a lot, Otti and Richard, for your tireless efforts to improve my English.

This work was supported in part by the National Science Foundation (Grant No. DMR-8315691) and also in part by the U.S. Department of Energy (Contract No. DE-AC02-76CH00016).

To

my parents

who invested their life in their children.

Table of Contents

List of Tables

List of Figures

1. Introduction

In recent years much progress was made in the study of matter and single crystals with positrons as the probe. In most cases the positrons are obtained from β^+ decaying isotopes of various metals. They are emitted with a broad range of energies which is suitable only for the study of bulk properties.[1] As an almost direct benefit the positrons could be moderated to thermal energies and then utilized in monoenergetic low energy beams. The efficiency of such a moderator can be as high as 10^{-3} of moderated positrons per produced energetic positrons. In spite of that as can be seen in figure 1.1 the more important intensity of such a source per energy interval can be dramatically increased. The extension of solid state research with positrons to surfaces and interfaces followed.[2] Low energy positron diffraction (LEPD) was proposed and demonstrated.[3–5]

Simultaneously positron beams were used to measure cross sections of positrons interacting with gasses. As the beam intensities increased work could be shifted from total cross section experiments to the investigation of the various partial cross sections.[6,7] Theoretical calculations[8] predicted a strongly forward directed Ps formation cross section. B.L. Brown suggested to take advantage of this feature and construct a beam of monoenergetic positronium atoms.[9] Such a beam was first constructed at University College London.[10]

Among the host of possible experiments with a Ps beam, investigating the possibility of low energy Ps diffraction (LEPSD) was proposed to be carried out by a group of scientists at Brookhaven National Laboratory (BNL).[4,11,12] Ps is

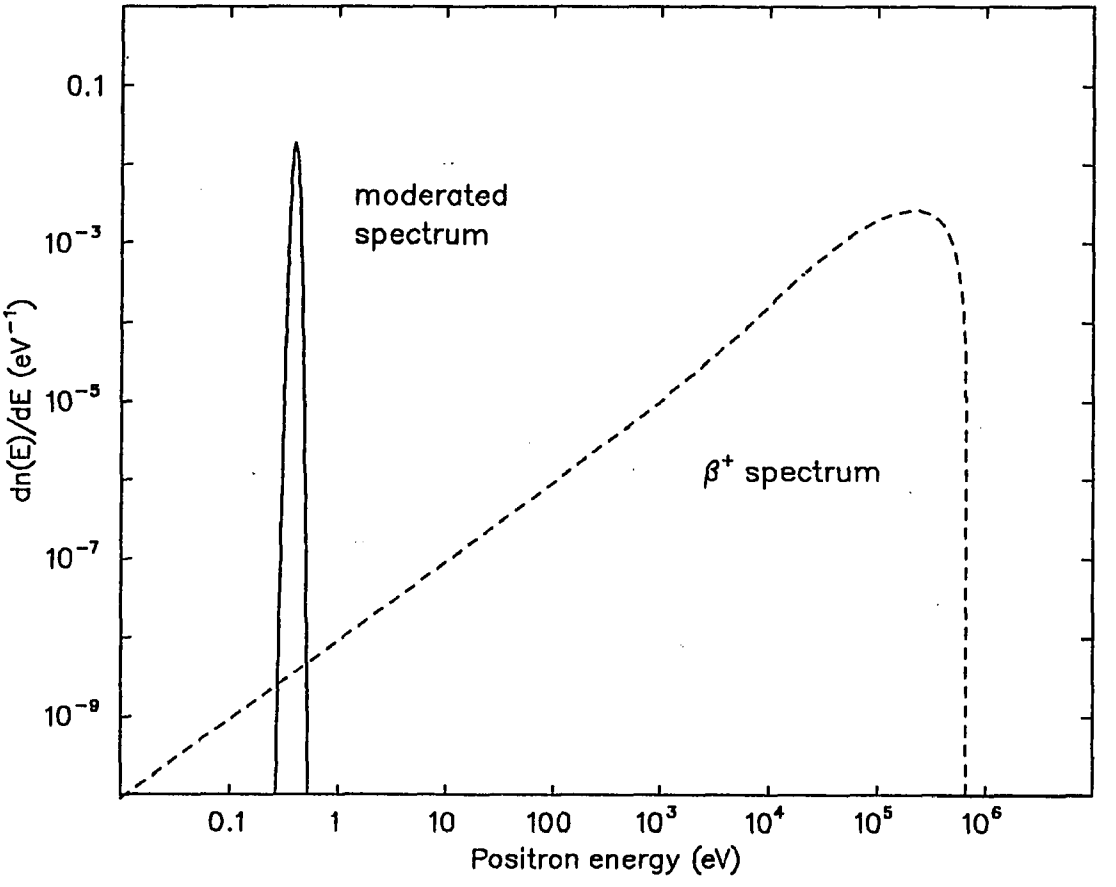

Figure 1.1 — Positron intensity per energy interval versus the positron intensity on a double log scale. Shown are the distribution for the β spectrum of ^{64}Cu and the distribution when this source has been moderated with an efficiency of $\epsilon = 10^{-3}$.

the lightest atom, which make it a unique candidate for diffraction experiments of ordered surfaces. A Ps atom with a de Broglie wavelength of 1Å needs to carry a kinetic energy of $75eV$. This compares favorably to He beams which need to be cooled to $0.02eV$ to obtain the same wavelength. At such low energies He atoms are unable to approach surfaces very closely. Ps can penetrate the surface potential barrier much deeper. It should provide more localized information about the surface potential, rather than He beams which see an average corrugated potential wall.[13] Contrary to electron and positron diffraction Ps diffraction is not complicated by the Coulomb interaction of the charged particles. It was found that Ps cannot exist

inside metals where the electron density is too large. Elastic scattering of Ps will be determined almost exclusively by the solid surface.

On the other hand Ps consists of a weakly bound state of a particle — the electron — and its antiparticle.[14] If energetic enough it can break up upon its collision with the surface. Above the band gap electronic excitations become possible. Ps has a finite lifetime and its ortho ground state (the electron and positron spins are aligned antiparallel) will decay with a lifetime of $142nsec$. The big question is whether Ps is scattered strongly enough to make Ps diffraction measurements possible given current flux limits. Also no theoretical work is available on the subject of Ps reflection for energies greater than $1eV$. For very low energies Pendry presented an estimates of the reflectivity for Ps from copper.[15] This work was initiated to investigate the feasibility of LEPSD. A beam of monoenergetic Ps atoms was constructed and directed at single crystal surfaces to measure the reflected intensity. The production process for Ps from a beam of positrons in a cell filled with a dilute gas was estimated to about 0.001 by B.L. Brown. He suggested the use of He gas at a pressure of $10^{-3}torr$. In order to reduce the background pressure at the sample differential pumping needs to be employed. The detectors for the Ps were located about $40cm$ from the gas cell. Along this path some of the Ps beam will decay in flight to the fraction of 0.3 at an energy of $60eV$. The Ps is detected by its annihilation radiation when it hits a metal target plate. Large amounts of shielding are required in order to reduce the radiation background from the gas cell. A quarter of the formed Ps in the ground state will be in the para state which decays with a half-life of $125psec$. That means most of it will decay already in the cell and contribute to the background. Background can be further reduced by registering the two opposing annihilation γ rays in coincidence. The efficiency of coincidence detection is estimated to about 1%. All factors are listed in table 1.1. That means that on the order of $3.3 \times 10^5 e^+ sec^{-1}$ are required to observe 1 Ps

atom in coincidence. That does not include the reduced beam intensity due to the less than total reflection. A reflection coefficient of 10% would make in excess of $3 \times 10^6 e^+ sec^{-1}$ necessary to observe one count per second.

Table 1.1: Efficiencies for Ps reflection

	Efficiency
Gas cell efficiency near $60eV$ Ps	0.001
Fraction surviving $40cm$ flight	0.3
Coincidence detection efficiency	0.01
Total efficiency at $60eV$	3×10^{-6}

Thus the success of this project was tied to the development of a high intensity positron beam. The novel idea of combining the positron moderator with the source promised beam intensities on the order of $10^8 e^+ sec^{-1}$. A pellet of copper isotopically enriched in ^{63}Cu is irradiated with thermal neutrons in the High Flux Beam Reactor at Brookhaven National Laboratory to produce the positron emitting isotope ^{64}Cu. Separate tests showed that copper performs well as a moderator.[16]

I was involved in the construction and development of this beam. Once positrons were available the gas cell section to generate the Ps beam could be built to study the reflection of Ps. In this thesis I discuss some of the physics of producing a self moderating source for a positron beam, the gas cell and my results from the Ps reflection measurements. As the project naturally falls into three parts I will divide my thesis along those lines rather than into the more traditional sections of theory, experiment and data analysis. Following this introduction are sections

on the positron beam, Ps formation in the gas cell and finally the reflection of Ps. Each section introduces the requirements necessary to continue in the next part. Once the positron beam has been characterized the efficiency of the gas cell can be mapped. For that section the reader may also refer to the thesis of B.L. Brown and the chapters on Ps formation in a gas therein.[17] In the last chapter on the reflection of Ps the measured Ps efficiency curve is used to obtain the reflection coefficients. In a brief summary I outline some of the planned work.

2. The Positron Beam

From the discovery of the positron in the early 1930s by Anderson[18] the field of positron physics has developed and expanded rapidly. The research effort was shifted from studies on the positron itself and its bound state with an electron to the use of positrons as a tool in solid state research. The understanding of the positrons's interaction with its environment in metals enabled the construction of positron beams, that over the years have become more and more intense.[19] Positrons emanating from β decays rapidly slow down to thermal energies inside the solid and begin to diffuse throughout it until they annihilate with an electron or they reach a surface. To extract the positron from the solid an energy equal to the work function, the sum of the chemical potential and a surface dipole potential. The dipole potential is created by conduction band electrons spilling out of the solid beyond the outermost ion cores. For positrons it is negative (i.e. pulling positrons out of the solid). In a number of materials, like W and Ni single crystals or MgO, the work function is negative. Positrons that reach the surface of these solids are expelled into the vacuum or they are trapped in the surface potential well. The expelled positrons gain a small amount of energy, the work function, and come off the surface in a cone which is strongly peaked in normal direction.

It is these positrons that can be accelerated to arbitrary energies and with the help of electric and magnetic fields they are guided in a beam to an experimental region. A continuously improving understanding of these processes increase the moderator efficiency, defined as the ratio of the low energy ("slow") positrons in a

beam to the number of produced positrons in a source, from an initial 10^{-6} to about 7×10^{-3} depending on the geometry at present.[20,21] Beams delivering on the order of 10^6 positrons per second are common. As source isotopes ^{22}Na and ^{58}Co are widely used. They can be deposited on tiny needles which in turn face moderators in various configurations. W and Ni single crystals are used for moderators in a backscattering geometry, where the positrons that return to the surface facing the source are utilized. In another geometry MgO powder is deposited on a venetian blind structure made of various metals.[22] Again the backscattered positrons are extracted and form the beam.

More recently thin foils measuring up to $1000nm$ in thickness were mounted in a transmission geometry.[23] Fast positrons from a source enter the single crystal foil on one side, and the thermalized positrons that diffuse to the opposite side are used. This method avoids the shadowing effect of the source holder, which blocks out a considerable fraction of the beam from a backscattering geometry. The stopping profile of positrons with the energy distribution of a β source (number of particles thermalized per unit volume) drops off exponentially with increasing distance from the source side.[24] The foil has to be thin enough to enable diffusion of the positrons through it. Materials with a high stopping power and a large diffusion constant are desirable.

In all cases most of the produced positrons never reach the moderator. The source itself stops positrons. They will annihilate in the source and be lost for the moderation process. This self absorbing effect becomes increasingly important with larger source sizes. In addition the source radiates in all directions, and the moderator geometries intercept only a small fraction of the emitted positrons. The remainder is lost. The closer source and moderator are placed together, the smaller these losses are. Since most moderators require some kind of heat treatment to improve their performance and the delicate source container does not withstand

great temperature differentials, the deposition of the source onto the moderator is technically not feasible.

Another possibility is to merge the source and the moderator together into one unit, a self moderator.[25] This method has been developed for the beam used in this project. The β^+ emitting isotope ^{64}Cu is embedded in a single crystal Cu(111) moderator. The efficiency of such a self moderator depends strongly on its thickness, it and is generally lower than that of a W(110) single crystal moderator. But this is more than compensated by the much improved geometry. Self absorption is now the source of thermalized positrons. Much larger sources can be used efficiently.

In this beam intensities as high as $10^8 e^+/sec$ have been observed and theoretical estimates reach $1.6 \times 10^8 e^+/sec$. Further improvements could be achieved by employing isotopic separation during the source deposition. The concentration of the ^{64}Cu atoms can be increased by factors on the order of 1000 by separating ^{63}Cu atoms from the activated copper with selective laser ionization methods.[26] An increase by more than an order of magnitude seems feasible. Such a source could be reduced in size.

Presently the only other way to obtain positron intensities in this range is to utilize pair production of bremsstrahlung from beam dumps of high energy electron accelerators.[27]

Self moderating sources have a couple of disadvantages. To produce a reasonable amount of source activity, neutron fluxes of more than $10^{14} n_0/cm^2 sec$ are necessary, which are rare. Even more important is the purity grade of the copper raw material. The slightest amounts of impurities of Al in the Cu for example drastically reduce the efficiency of the moderation process. The W crystal substrate could be a source of Carbon which will diffuse into the Copper layer during the evaporation and annealing processes. These effects are believed to weaken the intensity of the present beam to on the order of $10^7 e^+/sec$.

The combination of the recently discovered Neon moderators in combination with the Copper source will make the impurity problem irrelevant. The large moderation efficiency $\epsilon \approx 7 \times 10^{-3}$ and the near 100% reflection of thermal energy positrons by the solid neon layer enable beam intensities beyond those from a self moderator.

In this section I will confine myself to the copper source used in conjunction with the self moderating process, which was the starting point for my work on positronium (Ps) reflection. In the following I shall discuss the moderation and diffusion of positrons in more detail. We obtain ^{64}Cu source material by irradiating isotopically enriched copper ^{63}Cu with thermal neutrons in the High Flux Beam Reactor (HFBR) at Brookhaven National Laboratory (BNL). A section will discuss the physics of this process. The last two sections describe the source apparatus and the beam line and discuss the performance of the positron beam.

2.1. Positron Diffusion

Several things occur:

1) Positrons are implanted in the solid according to an implantation profile $p(z)$.
2) They move by diffusion throughout it. A diffusion constant D_+ describes this motion together with the diffusion equation

$$D_+ \frac{\partial^2}{\partial z^2} n(z) - \frac{1}{\tau_+} n(z) + R_0 p(z) = 0. \qquad (1)$$

Here $n(z)$ is the density distribution for the positrons, τ_+ is an average life time of the positrons in the material, and $R_0 p(z)$ is the product of positron beam intensity and a normalized implantation profile.

3) Eventually the positrons either annihilate inside the solid or they reach a surface from where they either get trapped in surface states, are emitted with an electron as Positronium (Ps), or are emitted as positrons.

4) If the surface is actually an interface then, depending on the work function between the two material, some positrons may actually be reflected back into the original material.

In all practical cases the time dependance of the intensity of the initial source of positrons is very much slower than that of the thermalization ($10^{-15} sec$) and diffusion ($10^{-12} sec$) processes inside the solid. A time independent diffusion equation adequately describes the ongoing process. A dynamic equilibriuin exists.

In the following and also in the diffusion equation (1) above I have assumed, that the solid under investigation has large area dimensions compared to its thickness and a one dimensional calculation is sufficient. Let me further assume a totally homogeneous solid which can have defects but they are distributed evenly across the whole extent of the solid. Then both D_+ and τ_+ are constant. The product of the two yields the square of the diffusion length L_+

$$L_+^2 = D_+ \tau_+. \tag{2}$$

Defining a function $i(z)$ proportional to the density function $n(z)$, which in this case is a one dimensional density

$$R_0 i(z) = D_+ n(z), \tag{3}$$

the diffusion equation can be rewritten as:

$$\left(L_+^2 \frac{\partial^2}{\partial z^2} - 1 \right) i(z) = -L_+^2 p(z). \tag{4}$$

The homogeneous part (the left side of equation (4)) has the two solutions

$$i_1(z) = exp\{z/L_+\} \tag{5a}$$

and

$$i_2(z) = exp\{-z/L_+\}. \tag{5b}$$

For each problem a set of boundary conditions apply that define the value of $i(z)$ or that of the first derivative of i, $\partial i(z)/\partial z$ at the boundary. The problem can then be solved with the help of the appropriate Green's Function

$$G(z,z') = \begin{cases} A_1(z')exp\{z/L_+\} + A_2(z')exp\{-z/L_+\}, & z \leq z' \\ B_1(z')exp\{z/L_+\} + B_2(z')exp\{-z/L_+\}, & z \geq z'. \end{cases} \tag{6}$$

$G(z,z')$ has to meet the same boundary conditions as the problem under investigation. In addition two more requirements have to be fulfilled. It is continuous at $z = z'$ and the first derivative with respect to z has a well defined step

$$G(z,z' = z - \epsilon) = G(z,z' = z + \epsilon), \text{ and} \tag{7a}$$

$$\frac{\partial}{\partial z'}G(z,z' = z - \epsilon) - \frac{\partial}{\partial z'}G(z,z' = z + \epsilon) = -\frac{1}{L_+^2}. \tag{7b}$$

The solution for the given boundary value problem is then given by

$$i(z) = -L_+^2 \int dz' G(z,z')p(z') \tag{8}$$

for any implantation profile $p(z')$. The flux at any point z_0 within the boundaries can be calculated from

$$\begin{aligned} j(z_0) &= -D_+ \frac{\partial}{\partial z}\Big|_{z=z_0} n(z) \\ &= -R_0 \frac{\partial}{\partial z}\Big|_{z=z_0} i(z). \end{aligned} \tag{9}$$

To determine the efficiency of a particular moderator one needs to calculate the positron flux j at the surface and consider the fraction that does not get trapped in a surface state or gets emitted with an electron as Ps. This fraction is the branching ratio Y_0, where the subindex stands for zero energy. Since I will only be talking about positrons I will drop the subindex "+" from now on and write L rather than L_+ for example.

Now the problem has been reduced to finding the appropriate functions A_1, A_2, and B_1, B_2, which only depend on z' and the particular boundary conditions. Two basic possibilities exist.

1) The surface is such that all the positrons escape the material as soon as they reach the surface (or the interface). This case I consider as given when, for example the positrons reach the vacuum surface of the copper moderator. The capture of positrons into a surface state or the expulsion with an electron as Ps is included into this case, since the positrons are lost to the diffusion process. Mathematically this means that the density of positrons vanishes at the surface and

$$i(z')\Big|_{\text{surface}} = 0. \tag{10}$$

2) No positron can pass the boundary. This condition does not necessarily apply to the flux of positrons in either direction. All positrons coming from one side of the boundary will be reflected and the flux, i.e. the first derivative vanish

$$\frac{\partial}{\partial z'} i(z')\Big|_{\text{surface}} = 0. \tag{11}$$

In the following I will combine these two conditions in a number of cases, which represent a number of moderator configurations.

1) The case of a free standing moderating foil. It shall have an area of dimensions that are very much larger than its thickness D.

$$i(0) = i(D) = 0 \tag{12}$$

This configuration is presently realized in the transmission moderator.

2) The thickness D of the above case can be increased towards infinity to simulate a thick solid ("thick" means that all positrons are stopped long before the far end surface could play a role in the diffusion process).

$$D \to \infty \tag{13}$$

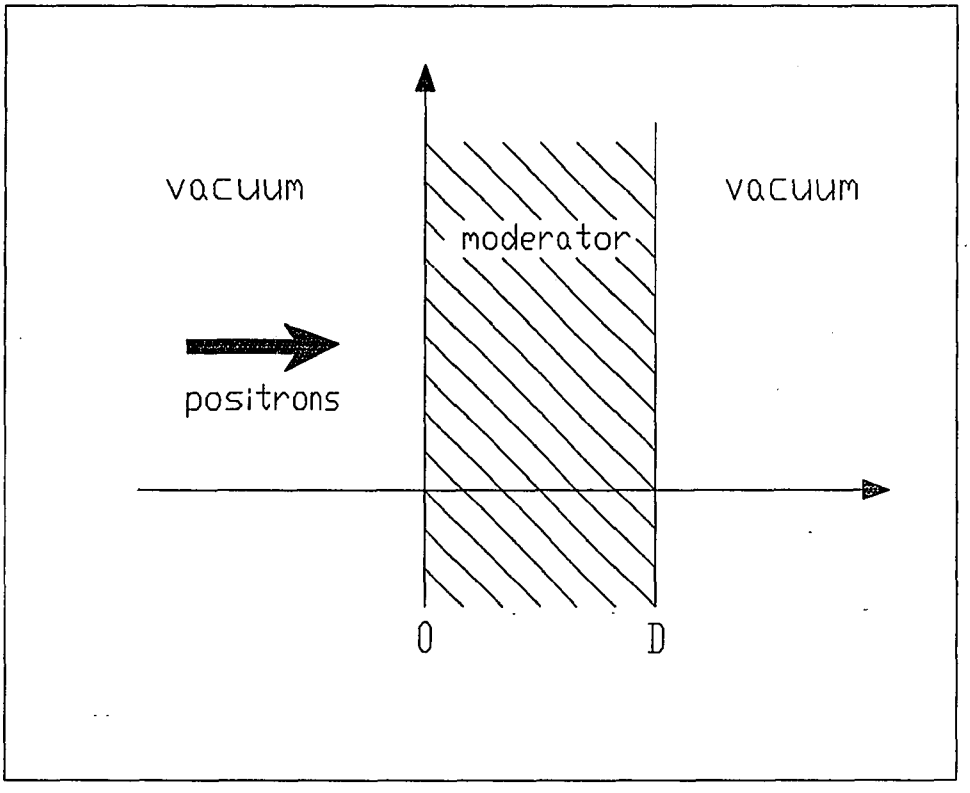

Figure 2.1 — Layout of a free standing self moderating foil. A monoenergetic beam of positrons is implanted into the foil from one side. Thermalized positrons will diffuse to either side. Some are emitted into the vacuum and can contribute to the beam of "slow" positrons.

3) The thin layer (case 1) is mounted on a substrate of infinite thickness. In addition I assume for this case that the work function for positrons passing from the substrate into the layer is negative. Both substances are moderating. In such a case the interface can be considered as a diode, permitting "slow" (i.e. thermal) positrons to pass only in the direction from the substrate into the overlayer, but not the other way. The flux across the interface must be negative (due to the chosen geometry in figure 2.2). For the calculation the problem can be split into two parts, the equations for the overlayer, and the equations describing the processes in the substrate. The four boundary

conditions are:

$$\begin{aligned} i(0) &= 0, \quad \text{and} \\ \frac{\partial}{\partial z} i(z)\Big|_{z=D} &= 0, \quad \text{for the overlayer part; and} \\ i(D) &= i(\infty) = 0, \quad \text{for the substrate part.} \end{aligned} \tag{14}$$

Once the flux out of the substrate is known, this can be used as input into the calculations for the overlayer.

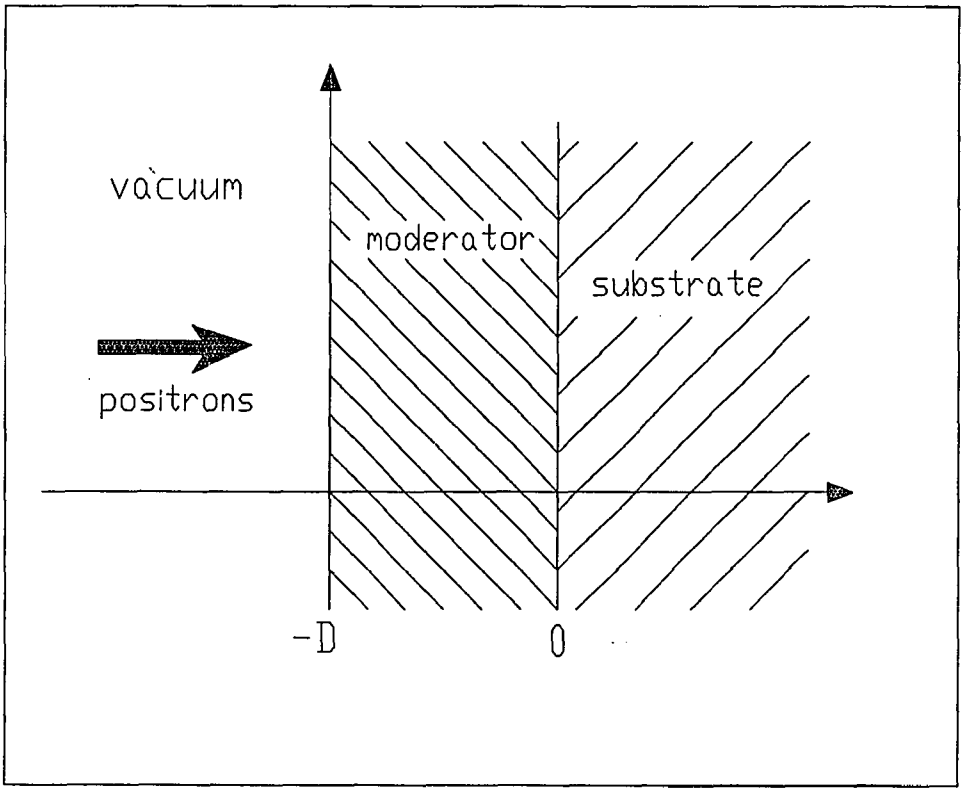

Figure 2.2 — Layout of a self moderator mounted on a substrate. Some positrons will be implanted into the substrate. A small fraction diffuses back to the vacuum surface of the overlayer. Thus the positron beam intensity will improve.

Let me now return to the first of the three problems:

At the front ($z_0 = 0$) as well as at the back ($z_0 = D$) of the layer the positron density vanishes.

$$i(0) = i(D) = 0 \tag{12}$$

Inserting this into the Green's Function ansatz, two of the unknown functions, $A_2(z')$ and $B_2(z')$, can be eliminated. Equation (6) appears in the simpler version

$$G(z,z') = \begin{cases} A(z')\Big(exp\{z/L\} - exp\{-z/L\}\Big), & z \le z' \\ B(z')\Big(exp\{z/L\} - exp\{(2D-z)/L\}\Big), & z \ge z' \end{cases} \tag{15}$$

Here I have omitted the subindices of A_1 and B_1 as well as that of the diffusion length L_+ for simplicity. The function is supposed to be continuous at $z = z'$ (see equation (7a))

$$\begin{aligned} &A(z)\Big(exp\{z/L\} - exp\{-z/L\}\Big) \\ &\qquad = B(z)\Big(exp\{z/L\} - exp\{(2D-z)/L\}\Big) \end{aligned} \tag{16a}$$

and the derivative jumps at the same location by the amount $-1/L^2$ (equation (7b))

$$\begin{aligned} &\frac{1}{L}A(z)\Big(exp\{z/L\} + exp\{-z/L\}\Big) \\ &\qquad -\frac{1}{L}B(z)\Big(exp\{z/L\} + exp\{(2D-z)/L\}\Big) \\ &\qquad = -\frac{1}{L^2}. \end{aligned} \tag{16b}$$

After multiplication of the second equation (16b) with

$$\Big(exp\{z/L\} - exp\{(2D-z)/L\}\Big)$$

and the elimination of on factor of $1/L$, then (16a) can be substituted into it. The the number of unknown functions is reduced to one.

$$\begin{aligned} A(z)\Big[&\Big(exp\{z/L\} + exp\{-z/L\}\Big)\Big(exp\{z/L\} - exp\{(2D-z)/L\}\Big) \\ &-\Big(exp\{z/L\} + exp\{(2D-z)/L\}\Big)\Big(exp\{z/L\} - exp\{-z/L\}\Big)\Big] \\ &= -\frac{1}{L}\Big(exp\{z/L\} - exp\{(2D-z)/L\}\Big) \end{aligned} \tag{17}$$

A number of terms cancel each other, when the products are multiplied out. The final solution for $A_1(z')$ (the subindex is used again) end up to be

$$A_1(z') = -\frac{1}{2L}\frac{exp\{(2D-z')/L\} - exp\{z'/L\}}{exp\{2D/L\} - 1} \tag{18a}$$

and for $B_1(z')$

$$B_1(z') = \frac{1}{2L}\frac{exp\{z'/L\} - exp\{-z'/L\}}{exp\{2D/L\} - 1}. \tag{18b}$$

This can now be plugged into the Green's Function ansatz to yield the result

$$G(z,z') = -\frac{1}{L}\frac{1}{sinh(D/L)}\times \begin{cases} sinh((D-z')/L)\,sinh(z/L), & z \le z' \\ sinh(z'/L)\,sinh((D-z)/L), & z \ge z'. \end{cases} \tag{19}$$

This can be inserted into the formula for the flux j at the location $z = z_0$

$$\begin{aligned} j(z_0) &= L^2 R_0 \frac{\partial}{\partial z}\Big|_{z=z_0} \int_0^D dz' G(z,z') p(z') \\ &= \frac{LR_0}{sinh(D/L)}\Big(\frac{\partial}{\partial z}\Big|_{z=z_0} \int_0^z dz' sinh(\frac{D-z}{L})\, sinh(z'/L)\, p(z') \\ &\quad + \frac{\partial}{\partial z}\Big|_{z=z_0} \int_z^D dz' sinh(z/L)\, sinh(\frac{D-z'}{L})\, p(z')\Big) \end{aligned} \tag{20}$$

The differentiation can be swapped with the integration and then performed.

$$\begin{aligned} = -\frac{R_0}{sinh(D/L)}\Big(&-cosh(\frac{D-z_0}{L}) \int_0^{z_0} dz' sinh(z'/L)\, p(z') \\ &+ Lsinh(\frac{D-z_0}{L})\, sinh(z_0/L)\, p(z_0) \\ &+ cosh(z_0/L) \int_{z_0}^D dz' sinh(\frac{D-z'}{L})\, p(z') \\ &- Lsinh(z_0/L)\, sinh(\frac{D-z_0}{L})\, p(z_0)\Big). \end{aligned} \tag{21}$$

Once again a couple of terms cancel each other and the flux at the two surfaces is directed out of the foil. At $z_0 = 0$ I get:

$$j(0) = \frac{-R_0}{sinh(D/L)} \int_0^D dz' sinh(\frac{D-z'}{L})\, p(z'). \tag{22}$$

At $z_0 = D$ the flux has the same form except for an opposite sign. The actual magnitude at each surface can differ depending only on the given implantation profile. Which side of the foil will eventually yield more slow positrons, depends not entirely on the implantation profile as equation (22) indicates. In the backscattering geometry the source in front of the foil will intercept a considerable fraction of the emanating positrons. On the other hand implantation profiles tend to be weighted on the side of the incident fast positrons as I will show later. The latter will put the transmission moderator geometry at a disadvantage.

The second of the above mentioned problems of a very thick moderator is basically a variation of the just solved scenario. All that remains to be done is to investigate the behavior of $j(0)$ as the foil approaches infinite thickness. I start from equation (22) and expand the *sinh* functions into the exponential function components. One part will become zero.

$$\begin{aligned}\lim_{D\to 0} j(0) = & R_0 \lim_{D\to 0} \left[\frac{1}{exp\{D/L\} - exp\{-D/L\}} \times \right. \\ & \Big(exp\{D/L\} \int_0^D dz' exp\{-z'/L\} p(z') \\ & \left. - exp\{-D/L\} \int_0^D dz' exp\{z'/L\} p(z') \Big) \right]\end{aligned} \tag{23}$$

The only remaining part is

$$j_\infty(0) = R_0 \int_0^\infty dz' exp\{-z'/L\} p(z') \tag{24}$$

which is the Laplace transform of the implantation profile. Here I have to assume that at some depth in the crystal the implantation profile will reach a maximum and eventually decrease back to zero. In all practical cases this is certainly the case, since the incident flux of fast positrons has to be finite.

The third and last of the problems can be split into two sections. One deals with the positrons in the substrate, and the other covers the overlayer. The work function at the interface is such that thermalized positrons can diffuse only in the direction towards the overlayer. Then the flux at the interface on the overlayer side for that section of the problem vanishes. The total flux is made up of the positrons diffusing back from the substrate side. For the substrate section of the calculations the interface can be considered as a vacuum surface. The density of thermalized positrons vanishes here just as it did in the previously considered case of a "thick" foil (equation 24). The subscript s will indicate the substrate:

$$-j_s = -R_0 \int_0^\infty dz' exp\{-z'/L_s\} p_s(z') \tag{25}$$

For the overlayer section the following boundary conditions apply:

$$i(z = -D) = 0 \quad \text{at the vacuum interface, and}$$

$$\frac{\partial}{\partial z}\Big|_{z\to 0} i(z) = \text{const.} \quad \text{at the substrate side.}$$

The diffusion equation is linear, and once more the problem can be simplified by splitting it into two parts. One of them may have the flux $j = 0$ at the substrate interface and contain the implantation profile. It will evaluate the fraction of positrons that thermalize in the overlayer and reach the vacuum surface. For the other part the flux is $j = j_s$ and the implantation profile vanishes. This second part merely describes the transport of the thermalized positrons from the substrate through the overlayer. Again the Green's Function ansatz needs to be made (equation 6).

$$G(z,z') = \begin{cases} A_1(z')exp\{z/L\} + A_2(z')exp\{-z/L\}, & z \le z' \\ B_1(z')exp\{z/L\} + B_2(z')exp\{-z/L\}, & z \ge z' \end{cases} \tag{6}$$

The condition $G(-D,z') = 0$ is met by setting

$$A_2(z') = -A_1(z')exp\{-2D/L\} = -A(z')exp\{-2D/L\} \tag{26}$$

and from

$$\frac{\partial}{\partial z}\Big|_{z=0} = \frac{1}{L}(B_1(z') - B_2(z')) = \frac{1}{L}B_0 \tag{27}$$

follows $B_2(z') = B_1(z') - B_0 = B(z') - B_0$. The requirement for continuity at $z = z'$ can be converted into the equation

$$\begin{aligned} A(z')\Big(exp\{z'/L\} - exp\{-(2D + z')/L\}\Big) \\ = B(z')\Big(exp\{z'/L\} + exp\{-z'/L\}\Big) - B_0 exp\{-z'/L\}. \end{aligned} \tag{28}$$

The defined step in the derivatives at $z = z'$ yields the last equation for the unique solution of A and B.

$$\begin{aligned} -\frac{1}{L^2} = &\frac{1}{L}A(z')\Big(exp\{z'/L\} + exp\{-(2D + z')/L\}\Big) \\ &-\frac{1}{L}B(z')\Big(exp\{z'/L\} - exp\{-z'/L\}\Big) - \frac{1}{L}B_0 exp\{-z'/L\} \end{aligned} \tag{29}$$

Again, multiplication of the above equation (29) with

$$L\Big(exp\{z'/L\} - exp\{-(2D + z')/L\}\Big)$$

makes the combination with the previous equation (28) easy. The results for $A(z')$ and $B(z')$ are then

$$A(z') = T(D/L)\left[B_0 - \frac{1}{2L}\Big(exp\{z'/L\} + exp\{-z'/L\}\Big)\right], \tag{30a}$$

and

$$B(z') = T(D/L)\left[B_0 - \frac{1}{2L}\Big(exp\{z'/L\} - exp\{-(2D + z')/L\}\Big)\right]. \tag{30b}$$

I defined the factor $T(D/L)$ as

$$\begin{aligned} T(D/L) &= \frac{1}{1 + exp\{-2D/L\}} \\ &= \frac{exp\{D/L\}}{exp\{D/L\} + exp\{-D/L\}} \\ &= \frac{1}{2}\frac{exp\{D/L\}}{\cosh(D/L)}. \end{aligned} \tag{30c}$$

The solved Green's Function is then

$$G(z,z') = \frac{1}{cosh(D/L)} \times$$
$$\begin{cases} \Big(B_0 - \frac{1}{L}cosh(z'/L)\Big) sinh((D+z)/L), & z \le z' \\ \Big(B_0 exp\{D/L\} - \frac{1}{L}sinh((D+z')L)\Big) cosh(z/L) & \\ \qquad - B_0 cosh(D/L) exp(-z/L), & z \ge z'. \end{cases} \tag{31}$$

For the flux $j(z_0)$ this means

$$j_l(z_0) = R_0 L_l^2 \frac{\partial}{\partial z}\Big|_{z=z_0} \int_{-D}^{0} dz' G(z,z')\, p_l(z'). \tag{32}$$

The index l indicates the overlayer. The solution for the Green's Function in equation (31) can be substituted into this.

$$\begin{aligned} j_l(z_0) = R_0 L_l^2 \frac{\partial}{\partial z}\Big|_{z=z_0} \times & \\ \Big[B_0 \Big(exp\{D/L_l\}\frac{cosh(z/L_l)}{cosh(D/L_l)} - exp\{-z/L_l\}\Big) \int_{-D}^{z} dz' p_l(z') & \\ + B_0 \frac{1}{cosh(D/L_l)} sinh(\frac{D+z}{L_l}) \int_{z}^{0} dz' p_l(z') & \\ - \frac{1/L_l}{cosh(D/L_l)} \Big(cosh(z/L_l) \int_{-D}^{z} dz' sinh(\frac{D+z'}{L_l}) p(z') & \\ + sinh(\frac{D+z}{L_l}) \int_{z}^{0} dz' cosh(z'/L_l)\, p(z')\Big)\Big] & \end{aligned} \tag{33}$$

Let me first deal with the terms, which contain the factor of B_0. The flux is only of interest at the vacuum surface where $z = -D$. A number of simplifications are possible, leaving

$$j_1(-D) = \frac{-R_0}{cosh(D/L_l)} \int_{-D}^{0} dz' cosh(z'/L_l) p(z'). \tag{34}$$

At the location $z = 0$ these terms of the flux add up to zero, and I do not need to consider them, while determining the value of B_0. So let me no look at the

remaining terms which contain the factor of B_0.

$$\begin{aligned} j_2(z_0) = B_0 \frac{R_0 L_l}{cosh(D/L_l)} \times \\ \Big[\Big(exp\{D/L_l\}\, sinh(z_0/L_l) + exp\{-z_0/L_l\} cosh(D/L_l)\Big) \int_{-D}^{z_0} dz' p_l(z') \\ + L_l \Big(exp\{D/L_l\}\, cosh(z_0/L_l) - exp\{-z_0/L_l\} cosh(D/L_l)\Big) p_l(z_0) \\ + cosh(\frac{D+z_0}{L_l}) \int_{z_0}^{0} dz' p_l(z') - L_l sinh(\frac{D+z_0}{L_l})\, p_l(z_0)\Big] \end{aligned} \tag{35}$$

This contribution to the flux has to match the flux of positrons coming from the substrate. That permits me to calculate the value of B_0 by setting $j_2(0) = j_s(0)$ and solving for B_0.

$$B_0 = -\frac{1}{L_l} \times \frac{\int_0^\infty dz' exp\{-z'/L_s\}\, p_s(z')}{\int_{-D}^{0} dz'\, p_l(z')} \tag{36}$$

This result can be plugged into equation (35) and when substituting $z_0 = -D$ I get

$$\begin{aligned} j_2(-D) &= -\frac{R_0}{cosh(D/L_l)} \int_0^\infty dz' exp\{-z'/L_s\}\, p_s(z') \\ &= \frac{1}{cosh(D/L_l)} j_s \end{aligned} \tag{37}$$

This means that the substrate contribution drops off as $cosh^{-1}(D/L_l)$ which is very fast since in most realistic cases of overlayers $D \gg L_l \approx 10^3 \text{Å} = 10^2 nm$. The sum of j_1 and j_2 from equations (35) and (37) forms the total flux of "slow" positrons out of the surface of the overlayer.

$$\begin{aligned} j(-D) = -\frac{R_0}{cosh(D/L_l)} \times \\ \Big(\int_0^\infty dz' exp\{-z'/L_s\}\, p(z') + \int_{-D}^{0} dz' cosh(z'/L_l)\, p_l(z')\Big) \end{aligned} \tag{38}$$

Finally I would like to summarize the results of the 3 problems: (noted are always the absolute values of the flux, which points out of the material in every case)

1) Backscattering from a self supporting foil of thickness D

$$j_b(D) = \frac{R_0}{sinh(D/L)} \int_0^D dz' sinh(\frac{d-z'}{L})\, p(z') \tag{22}$$

2) Transmission through the same foil

$$j_t(D) = \frac{R_0}{sinh(D/L)} \int_0^D dz' sinh(\frac{z'}{L})\, p(z') \tag{39}$$

3) Backscattering of "slow" positrons implanted into a thick ($D \rightarrow \infty$) crystal

$$j_\infty = R_0 \int_o^\infty dz' exp\{-z'/L\}\, p(z') \tag{24}$$

4) Backscattering from a layer (index l) of thickness D on top of a thick substrate (index s)

$$j_l(D) = \frac{R_0}{cosh(D/L_l)} \times \tag{38}$$
$$\Big(\int_0^\infty dz' exp\{-z'/L_s\}\, p(z') + \int_{-D}^0 dz' cosh(z'/L_l)\, p_l(z') \Big)$$

To determine the absolute values of the positron flux in each case, the knowledge of the implantation profile is required. I will deal with that in the following section.

2.2. Implantation Profiles

To estimate the intensity of a given source and moderator combination it is important to know the implantation profile of the positrons in the moderator. Thermal positrons diffuse only on the order of several 100Å to a few 1000Å in a single crystal. Thus the more positrons stop close to the surface of the moderator the higher the efficiency will be. This in turn also depends on the energy distribution of the particular source and on the stopping characteristics of the moderator. The former has been measured and the case of the β^+ emitter ^{64}Cu is shown in figure 2.3 below.[28]

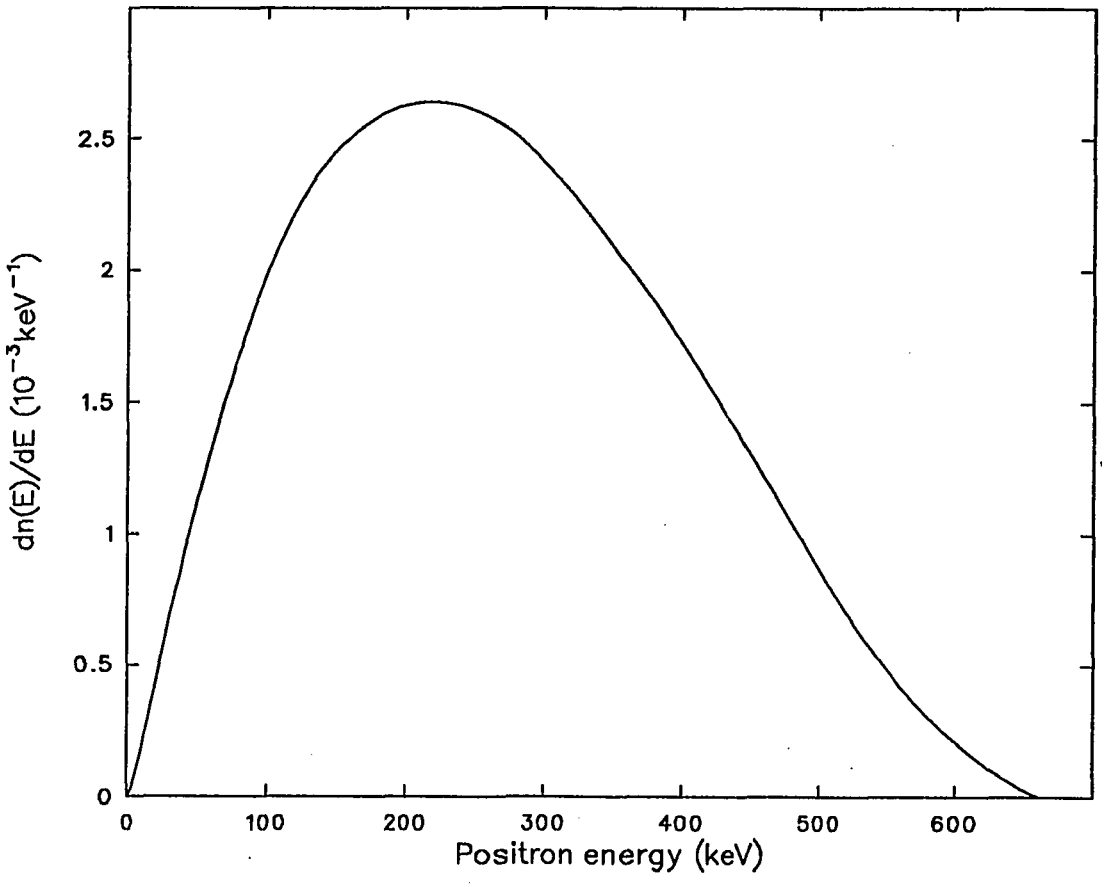

Figure 2.3 — Energy distribution of a β^+ source (in this case ^{64}Cu). The endpoint energy is $E_e = 658keV$.

More recent work with positron beams as well as Monte Carlo studies support an implantation profile shape for a monoenergetic beam that can closely be modeled by a Makhovian style profile[19,29–31]

$$p_m(z) = m\frac{z^{m-1}}{z_0^m} exp\{-(\frac{z}{z_0})^m\} \qquad (40a)$$

where m is a *shape* parameter. z_0 is a stopping length of the absorbing material, and it is related to the mean depth $\bar{z}$ and the beam energy.

$$z_0 = \frac{\bar{z}}{\Gamma(1+\frac{1}{m})} \quad ,\text{and} \quad \bar{z} = A\,E^n \qquad (40b)$$

The constants m, A and n have been determined experimentally to be

$$m \approx 1.9$$

$$A = 40nm \frac{g}{cm^3\, keV^n} \rho^{-1} \qquad (40c)$$

$$n = 1.6$$

and ρ is the density of the absorbing material. Several profiles of this shape are shown in figure 2.4 for various incident beam energies E.

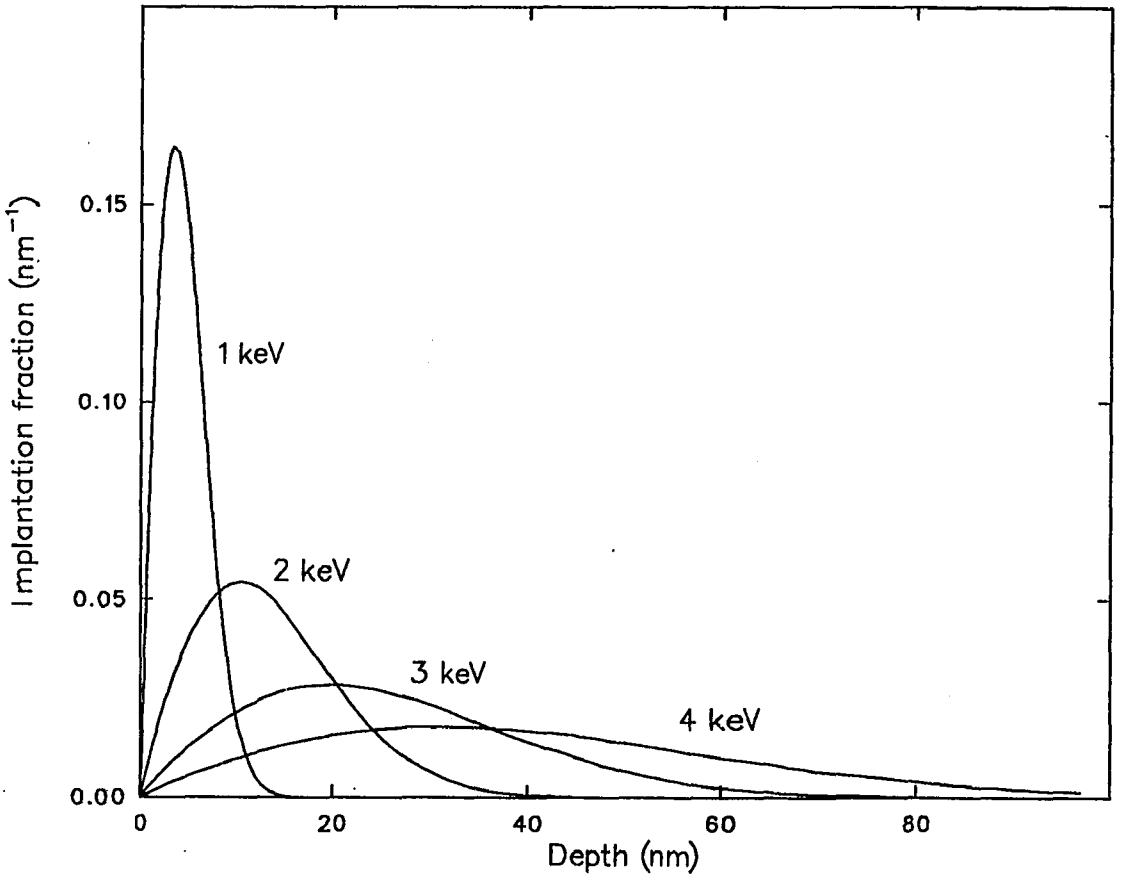

Figure 2.4 — Implantation profiles of monoenergetic positrons incident on a copper crystal. The different curves show the effect of the positron energy E.

The implantation profiles of a β^+ source have been measured to be close to an exponential shape.[24] To check this, I have convoluted the energy spectrum of a ^{64}Cu source with the implantation profile of monoenergetic sources to obtain the profile of the copper.

$$p_{cu}(z) = \int_0^{E_e} dE \frac{\partial n}{\partial E} p_m(z, E) \qquad (41)$$

$E_e = 0.658MeV$ is the endpoint energy for this source. I should note that the implantation profiles for monoenergetic positrons have only been measured for energies far below E_e and I had to assume that this dependance is true for all relevant energies. The result of this calculation is shown in figure 2.5 together with an exponential function that best fits the shape of the convoluted result. for both cases copper was chosen for the absorbing material.

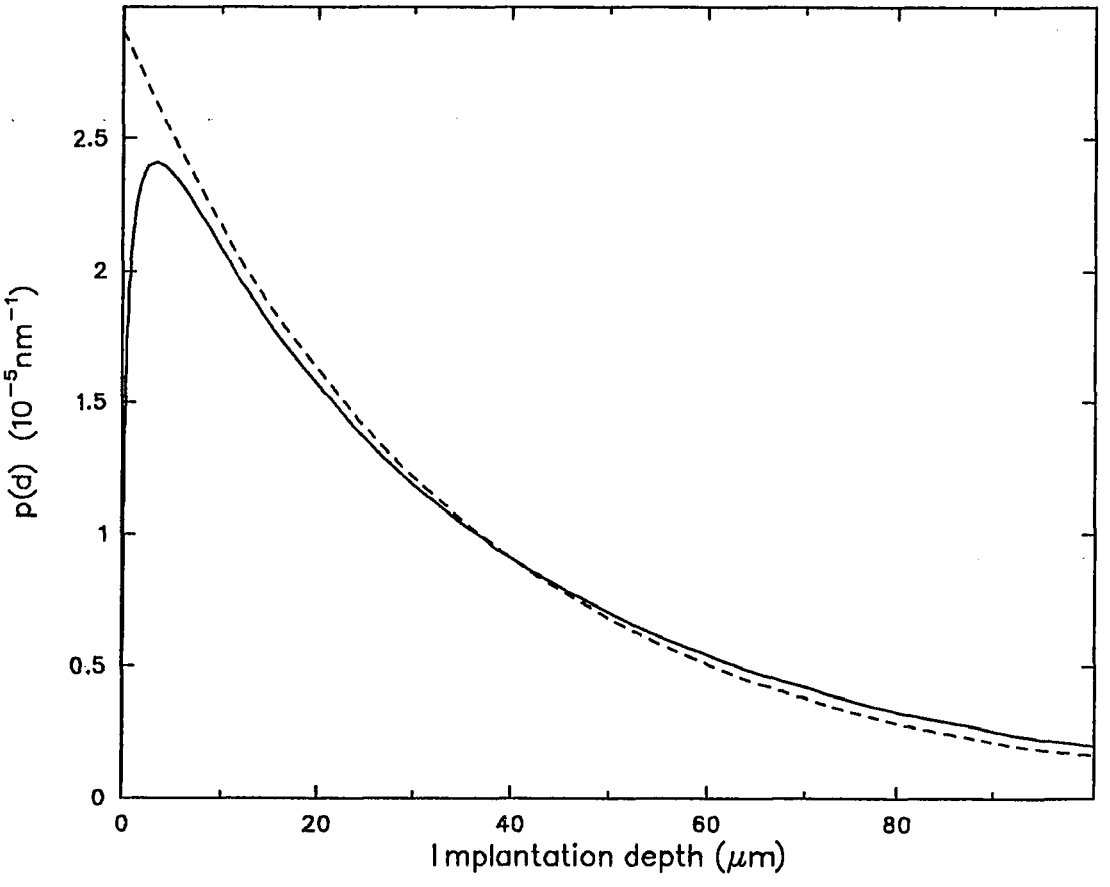

Figure 2.5 — Estimates of the implantation profile of positrons emanating from a ^{64}Cu source thermalizing in copper. Plotted is the fraction of the positrons generated that thermalize in a small layer of thickness Δd versus the implantation depth into the material d. The area under each curve was normalized to 1. The solid line represents the result of the convolution of the β^+ spectrum with the implantation profile of monoenergetic positrons, and the dashed line is an exponentially decreasing function that best fits the convolution result. Except at very shallow depth agreement is fairly good.

Considering the uncertainties in the convolution calculation the agreement between the two profiles is reasonably good, except at very shallow depths. Consequently I shall use an exponential function for the following calculations of the implantation profile of a material that is simultaneously the source and the moderator. Such a configuration I will refer to as a self moderator.

Positrons will leave a tiny volume element in the source isotropically in all directions and a fraction $p_s(r)$ will thermalize at the distance r from this volume element.

$$p_s(r) = \alpha \, exp\{-\alpha r\} \tag{42}$$

For these calculations I will consider a thin foil of thickness D and a surface area $Area = h^2$. The sides of the foil shall be large compared to its thickness ($h \gg D$). For this case the problem of the positrons thermalizing in the foil and their subsequent diffusion to a surface can be reduced to one dimension perpendicular to the surface of the foil. The foil itself will be mounted as an overlayer on a substrate. In this case I will consider the case of a copper layer with the positron emitting isotope ^{64}Cu on a W(110) single crystal substrate. Both parts are capable of moderating positrons. Figure 2.6 is a cross section of the foil and its substrate and also defines all the used parameter.

Let me summarize the assumptions, that I make in addition to restricting myself to a one dimensional case:

1) The source activity A is spread homogeneously across the foil. The activity density (activity per unit length in this case) is defined as

$$a = \frac{\text{activity}}{D}$$

2) There is no source material at $z < -D$ (i.e. in the substrate).

3) When encountering the interface, positrons get either reflected elastically or penetrate into the substrate without changing their momentum. The

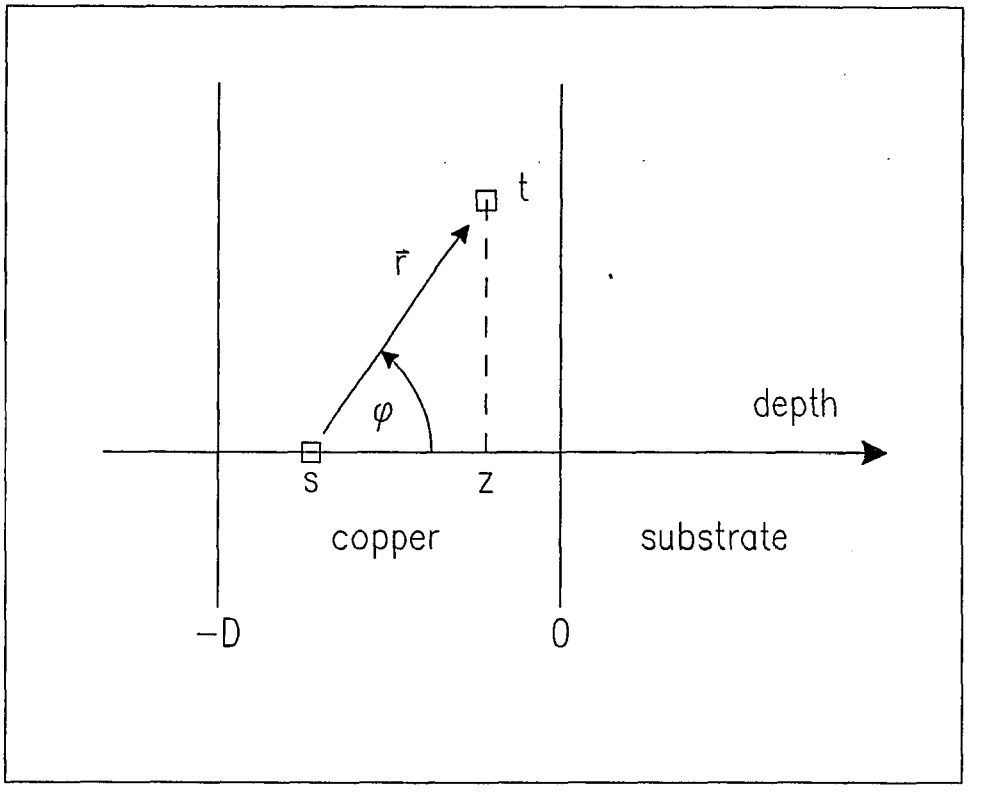

Figure 2.6 — Cross sectional sketch of the thin layer on a substrate. Positrons are emitted at a source volume element (s) and a certain fraction will thermalize at another element (t) at a distance r from (s). The vector r forms the angle φ with the z-axis. All the positrons stopping in the layer through z are integrated to yield the implantation profile as a function of z.

potential step between the materials is small compared to the energy of non thermal positrons.

4) The reflected fraction R is independent of the positron energy. This is not necessarily true. On the other hand the assumption seems reasonable for a first estimate of the implantation profile. The contribution of reflected positrons to the the fraction of positrons that will leave the source at thermal energies is small and thus any energy dependence of the reflection coefficient would have little effect.

Let me now calculate the implantation profile of this configuration. It is made up of two parts, the positrons that stop in the source layer itself makes up one

part, and the ones that enter the substrate constitute the other. All the positrons that thermalize at the depth z in the source or in the substrate are integrated (see figure 2.6). The radial coordinates used for the basic implantation profile (equation (27)) will be converted to cartesian coordinates, which are more suitable for the geometry of the source. Positrons originate in β^+ decays of ^{64}Cu atoms in the volume element dV_s at z' and a certain fraction will thermalize in a second volume element dV_t at $z'' = (z - z')$. The distance between the two volumes is

$$r = \frac{|z - z'|}{cos\varphi}. \tag{43}$$

At that distance a fraction according to equation (42) will thermalize in a sphere around the source volume. The common points on this sphere with the plane perpendicular to the z-axis and intersecting the axis at z forms a ring. I am interested in the volume elements that follow this ring and make up

$$\frac{1}{4\pi r^2 dr} 2\pi r \, sin\varphi \, r d\varphi dr = \frac{sin\varphi}{2} d\varphi \tag{44}$$

of the sphere around dV_s. To find the fraction of positrons that stop in the layer through z, I need to integrate over all the angle radius combinations that form a constant $z'' = (z - z')$ and then integrate over all $-D \leq z' \leq 0$.

$$\frac{a\alpha}{2} \int_0^{\pi/2} d\varphi dr \, sin\varphi \, exp\{-\alpha r\} \tag{45}$$

The integration over z'' will become easier once the coordinates are converted into cartesian coordinates (i.e. r and ϕ into z'' and t) with

$$r cos\varphi = z'', \text{ and } \quad cos\varphi = t$$

The necessary conversion factor can be calculated from the determinant of the Jacobian matrix.

$$dz'' \, dt \; = \; \left| \begin{vmatrix} \frac{\partial z}{\partial r} & \frac{\partial z}{\partial \varphi} \\ \frac{\partial t}{\partial r} & \frac{\partial t}{\partial \varphi} \end{vmatrix} \right| dr \, d\varphi$$

$$= \left| \begin{vmatrix} cos\varphi & -r\,sin\varphi \\ 0 & -sin\varphi \end{vmatrix} \right| dr\,d\varphi \tag{46}$$

$$= cos\varphi\, sin\varphi\, dr d\varphi$$

To obtain the total amount of positrons thermalizing at z, two integrations need to be performed. One is the integration over all possible values of t (formerly φ), and the other accumulates the contributions from all source volume elements along the z-axis.

$$p(z) = \frac{\alpha}{2D} \int_{-D}^{0} dz' \int_{0}^{1} dt \frac{1}{t} exp\{-\alpha \frac{|z - z'|}{t}\} \tag{47}$$

The order of two integral operations can be switched around and the z' integration is easy.

$$p(z) = \frac{1}{2D} \int_{0}^{1} dt \Big[2 - exp\{\alpha z/t\} - exp\{-\alpha(d + z)/t\}\Big] \tag{48}$$

The fraction F is the amount of positrons that stop inside the source.

$$F(D) = \int_{-D}^{0} dz\, p(z) \tag{49}$$

$$= 1 - \int_{0}^{1} dt \frac{t}{\alpha D} (1 - exp\{-\alpha D/t\})$$

In the case of ever increasing thicknesses ($D \rightarrow \infty$) this fraction will approach unity, i.e. all positrons will thermalize in the source. On the other hand, if one considers the positrons that escape thermalization inside of the source and emanate from one side, one gets

$$S(D) = \frac{1}{2} aD\,(1 - F(D))$$

$$= \frac{a}{2} \int_{0}^{1} dt \frac{t}{\alpha} (1 - exp\{\alpha D/t\}) \tag{50}$$

$$\Rightarrow \frac{a}{2\alpha} \quad \text{when} \quad D \rightarrow \infty.$$

That means that for large values of D the value of S will become a constant and an increase in activity of the source will not result in a more intense positron beam, if a moderator outside the source is used. This effect severely limits the intensity of

present slow positron beams. A second cause for inefficient use of the source activity is the distance of the moderator from it. Even though this was not included into the above calculations, the fast positrons leave the source isotropically in all directions, and the moderator intercepts only a small fraction of the full 4π sphere.

Let me now return to the implantation profile for positrons stopping inside the source and its substrate. In addition to the part calculated in equation (48) above some fast positrons will be reflected from the source-substrate interface and the thermalize in the source. To obtain that part of the profile, all that remains to be done is to substitute the distance between the two volume elements dV_s and dV_t. In this case

$$z'' = |z - z'| \Rightarrow |- z - z'|.$$

A fraction R of the positrons hitting the interface will be reflected. The other calculations are similar to the ones above and I get for the implantation profile contribution due to reflection

$$p_r(z) = \frac{1}{2} R \frac{\alpha}{D} \int_0^1 dt \, (1 - exp\{-\alpha D/t\}) \, exp\{\alpha z/t\}. \tag{51}$$

The part $(1 - R)$ of the positrons will penetrate into the substrate and thermalize according to

$$p_s(z) = \frac{1}{2} (1 - R) \frac{1}{D} \frac{\alpha_s}{\alpha} \int_0^1 dt \, (1 - exp\{-\alpha D/t\}) \, exp\{-\alpha_s z/t\}. \tag{52}$$

Here the distance is calculated according to $\alpha z'' = -\alpha z' + \alpha_s z$, where α_s is the stopping parameter in the substrate. The factor of α_s/α ensures that the total number of positrons remains unity.

Finally let me summarize the results so far. I have calculated the various contributions to the implantation profile in a layer of source material (i.e. copper in this case) of thickness D deposited on a substrate (made of tungsten in this case).

In the copper layer the implantation profile is:

$$p(z) = p_d(z) + p_r(z)\ , \text{and } -D \leq z \leq 0$$

$$p_d(z) = \frac{1}{2D}\int_0^1 dt\Big[2 - exp\{\alpha z/t\} - exp\{-\alpha(D+z)/t\}\Big] \tag{48}$$

$$p_r(z) = \frac{1}{2D}R\int_0^1 dt\Big[1 - exp\{\alpha D/t\}\Big]exp\{\alpha z/t\} \tag{51}$$

with $p_d(z)$ for the "direct" part and $p_r(z)$ for the reflected part.
And profile in the substrate amounts to:

$$p_s(z) = \frac{1}{2D}(1-R)\frac{\alpha_s}{\alpha}\int_0^1 dt\Big[1 - exp\{\alpha D/t\}\Big]exp\{\alpha_s z/t\} \tag{52}$$

for $0 \leq z$. Also, I have calculated the fraction of fast positrons that leave the layer of copper on the vacuum side and are available for moderation by an outside moderator.

$$s(D) = \frac{1}{2}\int_0^1 dt\frac{t}{\alpha D}(1 - exp\{-\alpha D/t\}) \tag{50}$$

In this equation the contribution from positrons, that are reflected at the substrate interface has been neglected. In most practical cases the source is too thick to worry about them.

The calculated implantation profiles resulting from a source layer of Cu(111) on a W(110) substrate are shown in figure 2.7. The copper layer is chosen to be $10^5 nm$ thick, and the reflection coefficient $R = 0.17$ was determined empirically.[24] The stopping parameters for copper and tungsten are $\alpha = 2.909 \times 10^{-5} nm^{-1}$ and $\alpha_s = 7.918 \times 10^{-5} nm^{-1}$ respectively[32] They were calculated according to the formula

$$\alpha = \mathrm{C}\rho \mathrm{Z}^{0.25}\bar{E}^{-1.58}, \text{ and } \quad \mathrm{C} = 1.1 cm^2 g^{-1} MeV^{1.58} \tag{53}$$

where $\rho = 8.96(19.3) g/cm^3$ is the density for Copper (Tungsten) and $\bar{E} = 0.2 MeV$ is the mean energy of the positrons coming from the copper source.

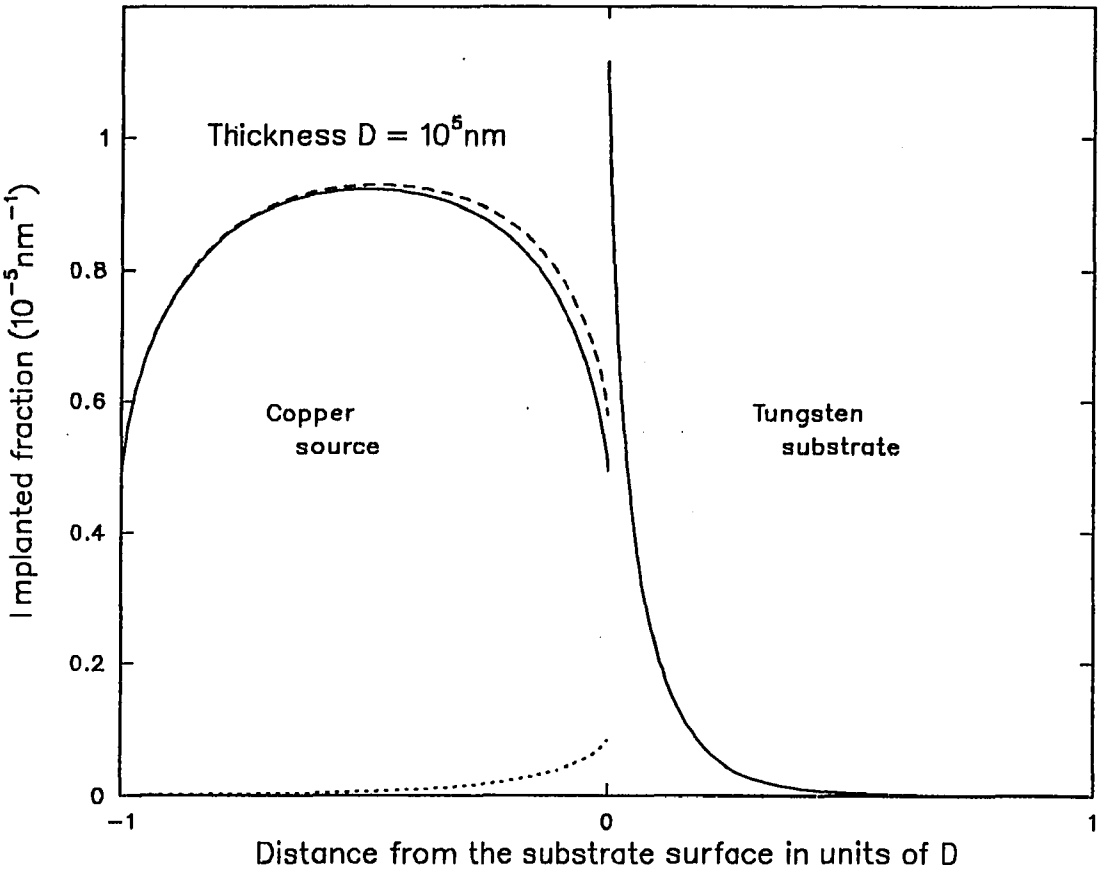

Figure 2.7 — Implantation profiles of a ^{64}Cu source in copper which has been evaporated onto a W single crystal. The distance from the substrate surface is given in units of the thickness D of the copper layer. The various lines represent: (- - -) the Copper layer alone, (· · ·) the backscattered part, and (—) the total or the part in the substrate.

2.3. Efficiency of a Self Moderator

The results of the sections on the implantation profile can be combined with the section on diffusion of positrons. In order for the self moderator to work, the source of ^{64}Cu in copper must be grown as a single crystal. The (111) orientation with sulphur on the surface (on the order of a monolayer) was found to be the best. It can be grown relatively easy on a W(110) substrate, which can also moderate positrons. If I assume that the copper tungsten interface is perfect and defects, if any, are distributed evenly across the source, then I can utilize the result from the diffusion equation calculations.

The fraction of slow positrons expelled from the Cu surface is proportional to the positron flux just inside the Cu. When traversing the surface, positrons can also pick up an electron to form thermal Ps or they can drop into a surface state. In the limit $E \rightarrow 0$ the fraction Y_0 will survive as positrons.

$$\begin{aligned}\varepsilon(D) &= \frac{Y_0}{R_0} j(D) \\ &= \frac{Y_0}{\cosh(D/L)} \left[\int_0^\infty dz\, exp\{-z/L_s\} p_s(z) \right. \\ &\qquad \left. + \int_{-D}^0 dz\, \cosh(z/L) \left(p_d(z) + p_r(z) \right) \right]\end{aligned} \tag{54}$$

Again the subindex s stands for the substrate, d for the part implanted directly in the source, and r for the reflected part. Each profile contains an integral, the execution of which can be swapped with the integration over z. The final versions from the implantation profiles, listed at the end of the previous section, can be inserted into these formulas. I will again treat the individual implantation profile contributions separately. One of the integrations in each part can be performed analytically. After that I tried to present the formulas for the efficiency in the form, that I used for the numerical integration. A number of difficulties were encountered due to divergences in the integrand.

For the direct part of positrons slowing down in the moderator and then diffusing toward the vacuum interface I get:

$$\epsilon_d(D) = \frac{1}{2}Y_0\alpha L\frac{1+exp\{-D/L\}}{1+exp\{-2D/L\}} \left[\frac{L}{D}\Big(1-exp\{-D/L\}\Big)ln\frac{1+\alpha L}{1-\alpha L} + \int_0^1 dt\frac{t}{\alpha D}\Big(1-exp\{-\alpha D/t\}\Big)\Big(\frac{1}{t-\alpha L}-\frac{1}{1+\alpha L}exp\{-D/L\}\Big)\right] \quad (55)$$

For very thick source moderators, this part will be the only contribution to the final positron beam. In reality this becomes the case for $D \gg L$.

$$\lim_{D\to\infty}\epsilon_d(D) = \frac{1}{2}Y_0\frac{L}{D}\alpha L\, ln(\frac{1+\alpha L}{1-\alpha L}) \quad (56)$$

Actually the efficiency drops of like D^{-1} but this will be compensated by the linearly increasing amount of source activity. Because of this it may be more convenient to discuss the product of absolute efficiency ϵ and the thickness of the source. This value has the unit of length and will be proportional to the intensity of the emerging positron beam.

$$E(D) = D\epsilon(D) \quad (57)$$

Returning to thinner sources, I calculate for the part reflects off the substrate interface prior to thermalization

$$\epsilon_r(D) = \frac{1}{2}Y_0R\alpha L\frac{1}{1+exp\{-2D/L\}}\int_0^1 dt\frac{t}{\alpha D}\Big(1-exp\{-\alpha D/t\}\Big) \left[\frac{1}{t+\alpha L}\Big(1-exp\{-D/L\}exp\{-\alpha D/t\}\Big)exp\{-D/L\} - \frac{1}{t-\alpha L}\Big(exp\{-D/L\}-exp\{-\alpha D/t\}\Big)\right] \quad (58)$$

and for the part thermalizing inside the substrate (assuming W for this case)

$$\epsilon_s(D) = Y_0(1-R)\alpha_s L_s\frac{exp\{-D/L\}}{1+exp\{-2D/L\}} \int_0^1 dt\frac{1}{t+\alpha_s L_s}\frac{t}{\alpha D}\Big(1-exp\{-\alpha D/t\}\Big) \quad (59)$$

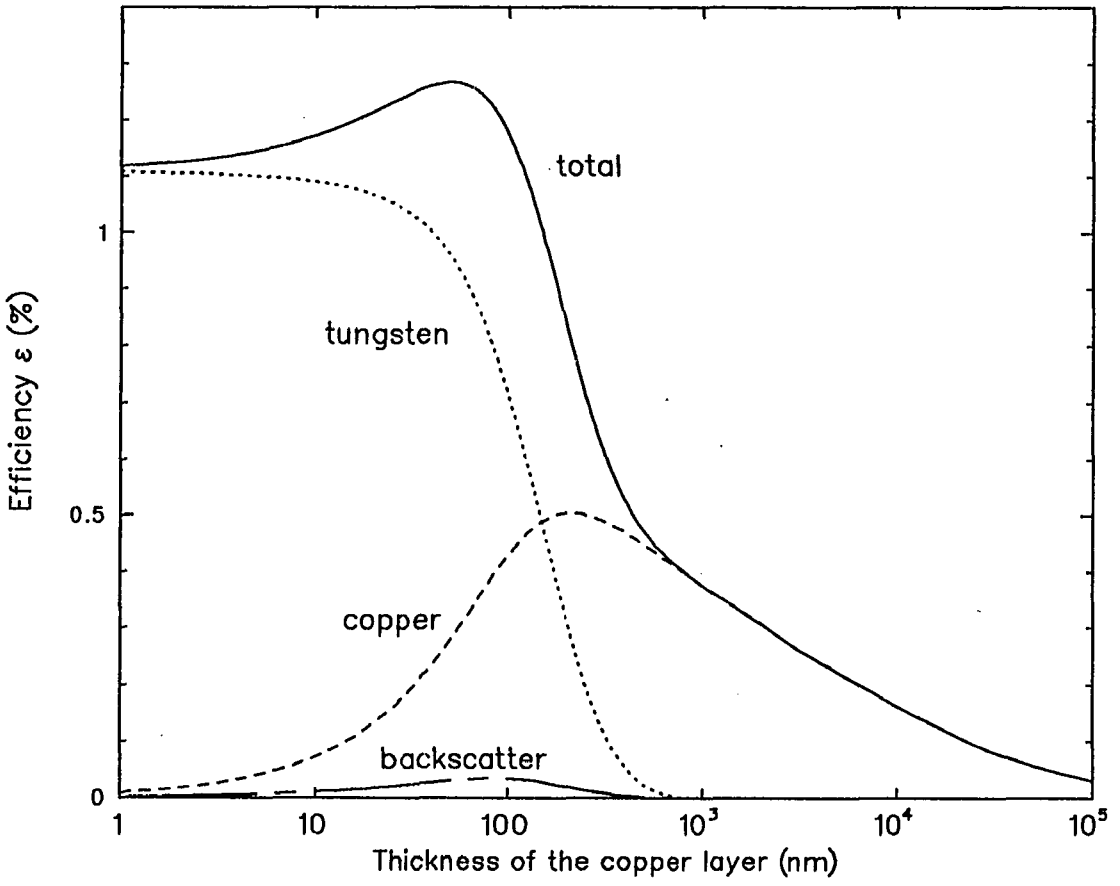

Figure 2.8 — The various components of the efficiency ϵ of a self moderating source of ^{64}Cu evaporated onto a W single crystal. Shown are the efficiency due to the Cu itself (- - -), the fraction due backscattering from the substrate (- — -), and the part that moderates in the W substrate(· · ·). The solid line represents the sum of the three components. All are plotted versus the thickness of the Cu layer on a semi log scale.

All three components of the efficiency of the self moderator were evaluated numerically and they are plotted in figure 2.8 as a function of the log of the thickness of the source in nm. The beam intensity I is given by

$$I = \epsilon D a$$

(a was defined as the activity per thickness). On a second figure (figure 2.9) the product ϵD, which is proportional to the beam intensity, is plotted versus the source thickness as mentioned in equation (57) on a log-log scale. It becomes more obvious on this kind of a plot, that the optimal thickness to obtain the most slow positrons

is not equivalent with the thickness of largest efficiency. On the other hand a factor of 1000 in source activity will only yield a factor of 10 more beam intensity.

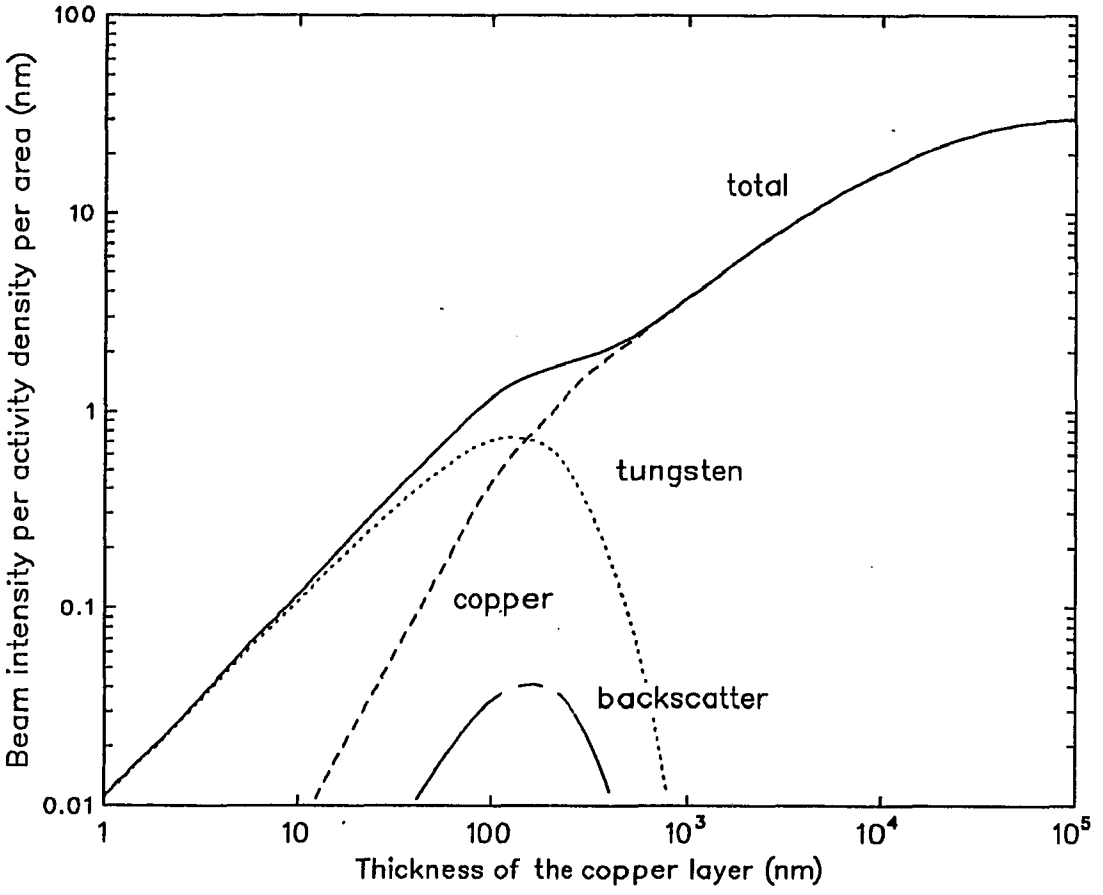

Figure 2.9 — Plots of the product of efficiency and thickness — which is proportional to the beam intensity — of the layer versus the Cu thickness on a double log scale. The symbols are as in the previous figure.

The contribution of the substrate (W) for very thin layers (on the order of $10nm$) is near 1%, which is comparable to other calculations for a W single crystal transmission moderator.[33] On the other hand the best W moderators in present beams yield on the order of 3×10^{-3} slow positrons of the original activity. This is largely due to the fact that the sources usually are not deposited directly on the moderator, but rather on a needle located a couple of mm away from the moderator. In that case a considerable fraction of fast positrons misses the moderator, and the

geometric factor becomes much less than 2π. In the above calculations I have assumed that the positrons thermalize in straight lines, which is only true for the statistical average. This assumption breaks down when one considers positrons being implanted at very shallow angles along the surface of the moderator. Once a scattering event directs a positron out of the crystal, it is lost to the moderation process. On the other hand, the largest fraction of moderated positrons comes from the region closest to the surface. Finally I should mention again that I considered a perfectly homogeneous layer of Cu and a Cu W interface with no additional defects.

2.4. Activation of the Copper Source

In the previous sections I discussed the advantages of using a source of positrons that is also capable of moderating the β-spectrum and of emitting thermal positrons. ^{64}Cu is such a material. It has a rather short half-life of $12.7 hours$ and needs to be produced close to the beam apparatus. In this section I will summarize the properties of Cu and ^{64}Cu in particular as they are related to their use as a self moderating source of positrons. All the relevant parameters are listed in the table 2.1 below. Figure 2.10 shows the decay scheme of ^{64}Cu.[34]

The positron emitting isotope ^{64}Cu is produced in the reaction

$$^{64}\mathrm{Cu}(\mathrm{n},\gamma)^{63}\mathrm{Cu}.$$

^{63}Cu occurs in natural copper with an abundance of 69.1%. It is also available commercially as highly enriched isotopic copper from Oak Ridge National Laboratory (ORNL). The cross section σ to absorb thermal neutrons, n_0, is $4.5 \times 10^{-24} cm^2$.

Since ^{64}Cu decays with a half-life of $t_h = 12.7 hours$, a high flux of thermal neutrons is required to produce reasonable amounts of this isotope. A system of two coupled differential equations describes these competing processes of production

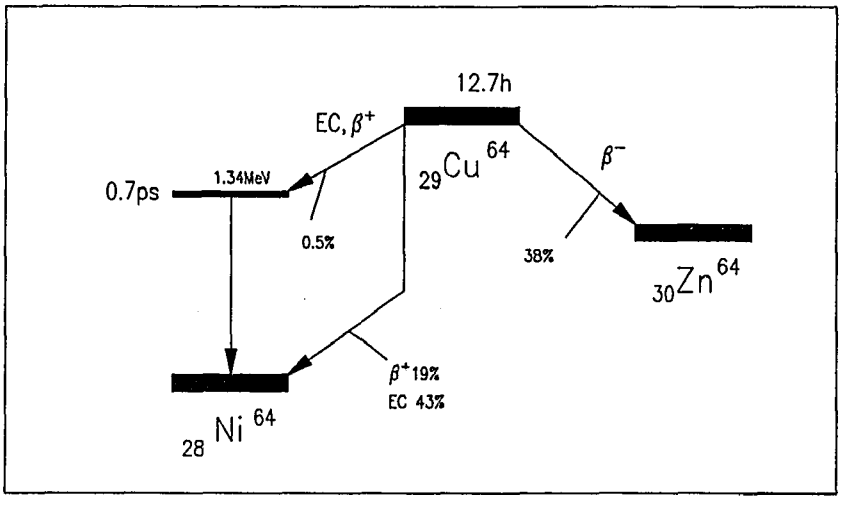

Figure 2.10 — Energy level scheme of ^{64}Cu and its decay products. The data are from Ref. 34

and decay. If n_i is the number of atoms of the kind ^{6i}Cu and λ_p and λ_d are the production and decay rates for ^{63}Cu and ^{64}Cu respectively (the subscript i is 3 or 4 for ^{63}Cu or ^{64}Cu respectively), then

$$dn_3 = -\lambda_p n_3\, dt \tag{60}$$
$$dn_4 = \left(\lambda_p n_3 - \lambda_d n_4\right) dt$$

with the definitions

$$\lambda_p = f\sigma = 8.3 \times 10^{14} \frac{n_0}{cm^2 sec} 4.5 \times 10^{-24} cm^2 = 3.74 \times 10^{-9} sec^{-1}$$
$$\lambda_d = \frac{ln2}{t_h} = 1.52 \times 10^{-5} sec^{-1} \gg \lambda_p. \tag{61}$$

In these equations f is the thermal neutron flux in the HFBR[35] and σ is the thermal neutron capture cross section. If N_3 atoms are available at $t = 0$ and no atoms of ^{64}Cu are present at that time, the solution is

$$n_3(t) = N_3 exp\{-\lambda_p t\} \tag{62}$$
$$n_4(t) = N_3 \frac{\lambda_p}{\lambda_d - \lambda_p} exp\{-\lambda_p t\}\left(1 - exp\{-(\lambda_d - \lambda_p)t\}\right)$$

Table 2.1: Properties of Copper

Property	Value
Density ρ	$8.96 g/cm^3$
Atomic weight M	$63.54 g/mol$
Melting point	$1083°C$
Boiling point	$2595°C$
Abundance of ^{63}Cu in natural Cu	0.691
Nuclear reaction used	$^{63}Cu(n_0,\gamma)^{64}Cu$
Thermal neutron capture cross section σ	$4.5 \times 10^{-24} cm^2$
Half-life of ^{64}Cu τ_h	$12.7h$
Decays to (fraction)	^{64}Ni (0.62) and ^{64}Zn (0.38)
β^+ fraction	0.19/decay
EC conversion fraction	0.43
β^- decay fraction	0.38
γ-rays of ^{64}Cu	0.005/decay @ $1.35 MeV$

for the irradiation time t. The number of atoms in a sample of weight m is determined by the atomic weight of Cu $M = 63.54 g/mol$, Avogadro's Number $N_a =$

$6.0225 \times 10^{23} 1/mol$, and the isotopic concentration of ^{63}Cu which is $c_3 = 69.1\%$ for natural Cu.

$$N_3 = c_3 \frac{m}{M} N_a = m\, 9.48 \times 10^{21} g^{-1} \quad \text{for isotopic Cu, and} \qquad (63)$$
$$= m\, 6.55 \times 10^{21} g^{-1} \quad \text{for natural Cu.}$$

After the source has been pulled out of the neutron flux, it will continue to decay. The decay rate r_4 is then governed by the time since the end of the end of the irradiation Δt.

$$\begin{aligned} r_4(\Delta t) &= R(t) exp\{-\lambda_d \Delta t\} \\ R(t) &= N_3 \frac{\lambda_p \lambda_d}{\lambda_d - \lambda_p} exp\{-\lambda_p t\}\Big(1 - exp\{-(\lambda_d - \lambda_p)t\}\Big) \\ &\approx N_3 \lambda_p \Big(1 - exp\{-\lambda_d t\}\Big) \end{aligned} \qquad (64)$$

Only 19% of all decays of ^{64}Cu result in a free positron. The remainder of the disintegrations yield 38% β^- events and 43% electron conversion events. The approximation in the last part of the above equation (64) is valid for the case of $\lambda_d \gg \lambda_p$ and $\lambda_p t \ll 1$, which is the case as long as the irradiation times are shorter than about 30 days. An irradiation time t_{max} is required, to obtain the highest concentration of ^{64}Cu isotope atoms.

$$t_{max} = \frac{1}{\lambda_d - \lambda_p} ln\Big(\frac{\lambda_d}{\lambda_p}\Big) = 6.34 \text{ days} \qquad (65)$$

The largest activity is also reached after this irradiation time. But most of this peak values ($\geq 95\%$) is already produces after only 2 to 3 days of activation as can be seen in figure figure 2.11. Here the source activity is plotted versus the irradiation time for 1 gram of isotopically enriched copper. Natural copper will yield 69.1% of that activity after equal irradiation times. The following figure shows the same function but with the irradiation time given on a log scale. A typical source pellet weighs about 100mg and is enriched in ^{63}Cu to 100%. It is irradiated for two days and generates $6.2 \times 10^{11} e^+/sec = 16.8 Ci\, e^+/sec$.

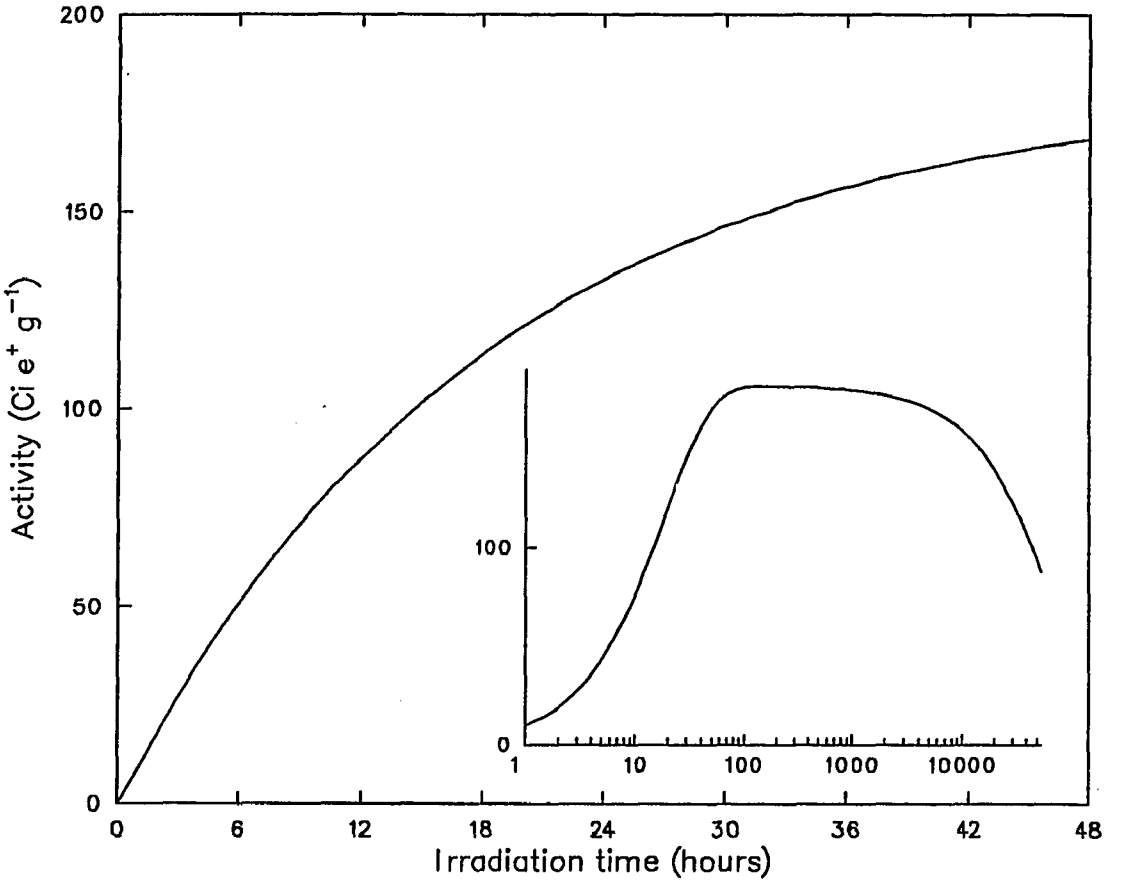

Figure 2.11 — Activity of an isotopically enriched ^{64}Cu source ($1g$) versus the irradiation time. the inset shows the long term dependence. Eventually the source material is exhausted and the activity will decay away faster than it can be generated by the neutron flux of $8.3 \times 10^{14} n_0/cm^2 sec$.

On the next figure the maximal activity is plotted as a function of the thermal neutron flux on a double log scale. A irradiation time is noted in several cases, which is required to reach this activity. The curve levels off only when the production rate λ_p becomes comparable to the decay rate λ_d. This limit is far out of reach for the present state of reactor technology. All present reactors fall into the region where the activity is proportional to the flux of neutrons.

All of the above calculations have been performed with the assumption of an energy independent thermal neutron cross section, which is probably adequate with the accuracy of the knowledge of the neutron flux in the reactor.

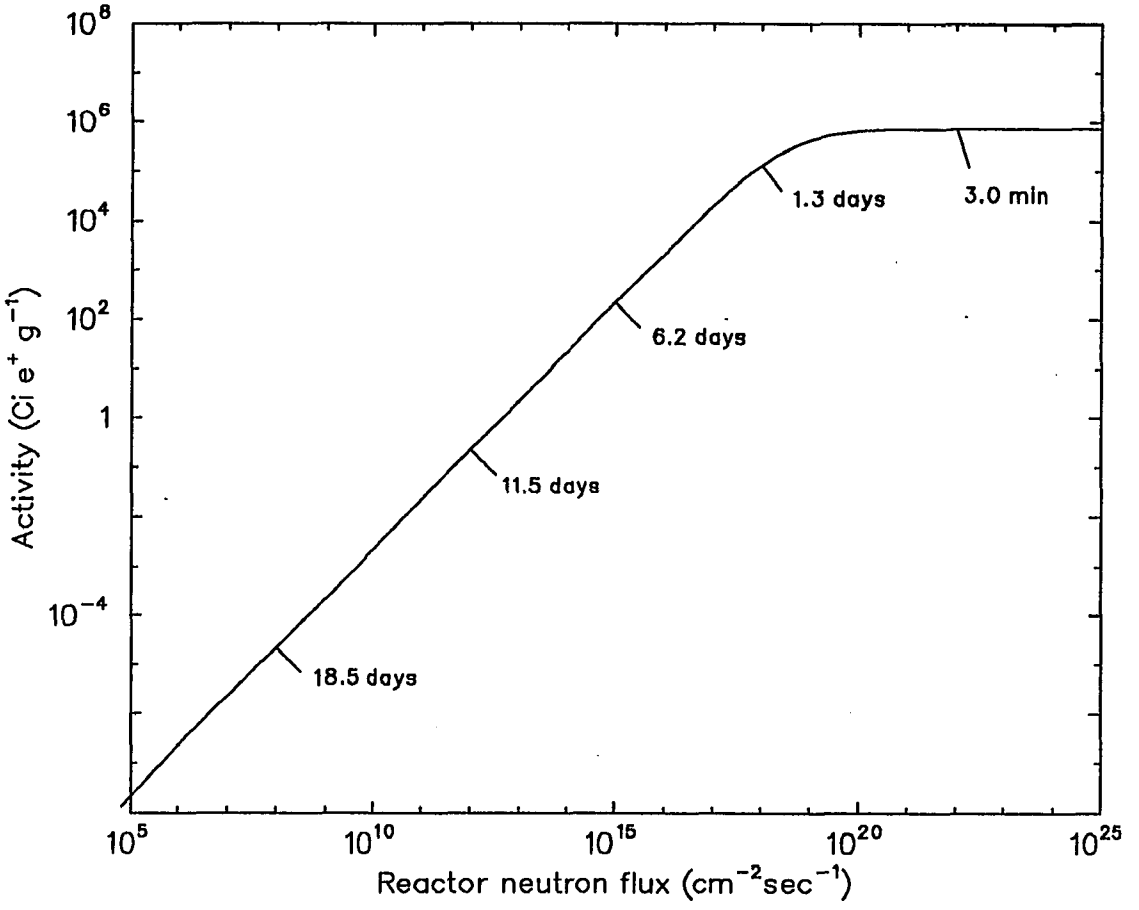

Figure 2.12 — The maximum activity of a given source as a function of the neutron flux. For a few cases the irradiation times necessary are displayed.

2.5. Description of the Positron Beam

In this section I will discuss the experimental setup of a positron beam with a self moderating ^{64}Cu source. This beam was utilized in the experiments to measure the reflection coefficient of Ps from a LiF single crystal. During the course of this section, I will follow a typical copper source from its initial preparation and irradiation in the High Flux Beam Reactor (HFBR) at Brookhaven National Laboratory (BNL) to its utilization as a positron source in a ultra high vacuum (UHV) system. The performance of the beam will be discussed and a number of possible improvements will be pointed out, which are presently under construction or being investigated.

The starting material is copper of very high chemical purity. If the copper is enriched in the isotope ^{63}Cu, the activity density of the source increases by about 43%. It is necessary to avoid chemical impurities for two reasons. First, some elements, like Al, will prevent the correct crystal growth of the source moderator, and thus reduce the efficiency of the source. Second, any impurities will be activated in the reactor and may be converted into long lived isotopes that emit energetic γ-rays. If their half-life is appreciable than that of ^{64}Cu, they will cause unnecessary radiation risks during routine maintenance work near or at the source chamber of the positron beam.

From the raw Cu material small round pellets of about $130mg$ are fabricated. To irradiate them in the reactor, they are inserted into Al capsules, coated with a thin layer of copper foil and sealed with a copper plug. The plug is e-beam welded to the capsule to make the assembly leakproof. A special design for the plug makes it possible to rip part of it off the capsule with about $140psi$ after irradiation, to let the pellet drop out. Both the plug and the foil, were fabricated from oxygen free material. They are etched in aqua regia and then rinsed in acetone, alcohol and distilled water prior to their use.

The completed assembly is welded to the end of a $40ft$ long Al tube and is inserted into the reactor through special irradiation thimbles to a location about one foot from the center of the core. Here the thermal neutron flux peaks at a level close to $10^{15}n_0/cm^2sec$ (see figure 2.13). Overheating is avoided by circulating water through the thimble from a supply separate from the reactor cooling system. After a typical irradiation time of two to three days the pellet has been activated to about $100Ci$ and the much heavier capsule radiates several thousand rad. From now on heavy shielding and remote handling are necessary. For this purpose the mechanism that opens the capsule and transfers the pellet into the vacuum system as well as

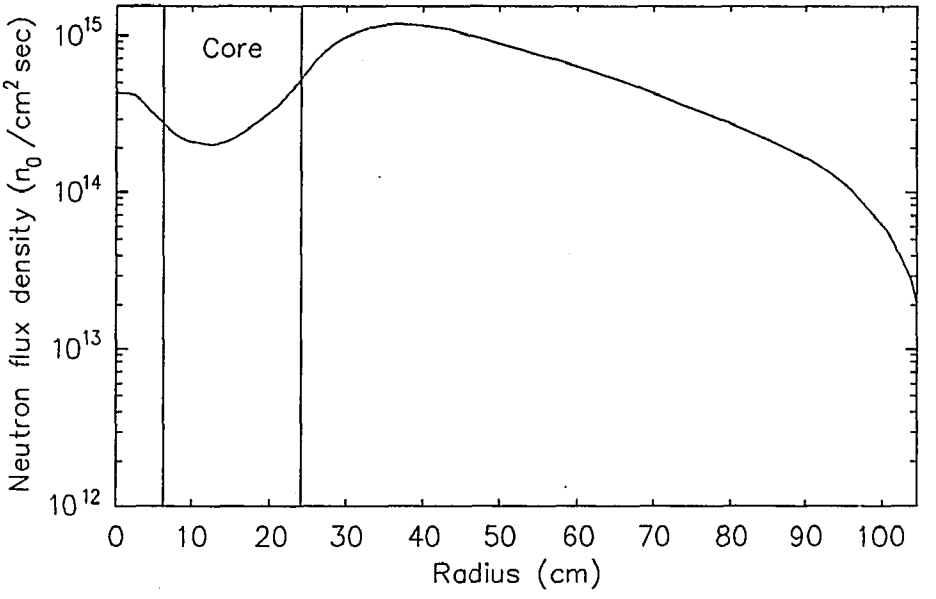

Figure 2.13 — The neutron flux as a function of the distance from the reactor core center for several neutron energies. The thermal flux used in the activation of ^{63}Cu peaks just outside of the core. (From the HFBR handbook in Ref. 35).

the source chamber of the positron beam are surrounded by a shielding house, the "blockhouse", made of $2ft$ thick dense concrete.

The activated capsule with the the "hot" pellet is dropped into an opening on the top of the blockhouse. It falls into a dryer where hot air evaporates any secondary cooling water, which is usually circulated in the irradiation thimbles. The next stage is the so called "shear", where the capsule is ripped open, and the pellet can fall out of it towards an airlock. The used capsule parts are directed into a separate lead container, where they are left to let most of the radioactive isotopes decay away.

The pellet, commonly known as the "beebee", is guided into a crucible in the source chamber located under the shear mechanism. A thin W(110) single crystal is rotated over the crucible and the copper is evaporated onto it. The W crystal is used to induce crystal growth in the Cu(111) direction and, in case of very thin Cu layers, to contribute to the moderation of fast positrons. Subsequent annealing of

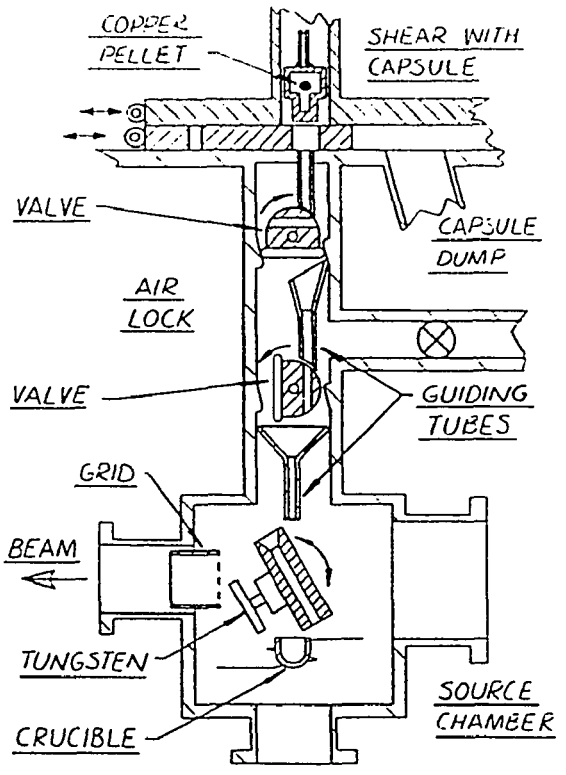

Figure 2.14 — Side view of the source transfer mechanism to separate the "beebee" from its container and to evaporate the copper onto the W(110) substrate. (See the text for explanations).

the Cu by resistively heating the W crystal and the deposition of a monolayer of S improve the moderation efficiency of the source. A schematic of this transfer region is shown in figure 2.14.

The fraction of moderated positrons that escape being trapped in surface states or emission as positronium (Ps) emanate from the surface in normal direction with an energy of its work function. External electric fields accelerate them to the desired beam energy and a magnetic field guides them out of the blockhouse to the experimental chamber. Additional grids near the source improve the momentum distribution of the positron beam, which in turn can influence the angular Ps distribution. The moderated, "slow", positrons are separated from the energetic,

"fast", positrons, which were not moderated, in a region of crossed electric and magnetic fields. In this $\vec{E} \times \vec{B}$ filter charged particles drift perpendicular to the fields. Only the "slow" positrons spend enough time in the filter to translate to an aperture offset from the initial beam axis. The "fast" positrons annihilate at a chamber wall and most γ-radiation is absorbed by lead shielding. The "slow" positrons are guided to an electrically floated chamber, the "gas cell", where Ps is formed. Grids at either end of the cell can be biassed to repel the positron beam. A schematic of the positron beam line is shown in figure 2.15. I will discuss the apparatus dealing with the Ps beam and the reflection experiment in a subsequent section.

Slow evaporation rates and careful annealings improve the performance of the moderator, but on the other hand this takes time during which the source will decay. A compromise has to be found. On average the source transfer from the initial drop into the blockhouse to the operating positron beam takes on the order of 2 hours. In that time about 10% of the source has decayed.

In the previous sections I have estimated the positron intensity to be in excess of $10^8 e^+/sec$. This rate has been reached during experiments not related to the Ps reflection measurements made for this work, for which rates of $4.5 \times 10^6 e^+/sec$ were available. Since then some modifications have been made on the beam line. The number of grids in the beam was increased to 6, each of which has an optical transmission of 90%. That alone will reduce the beam intensity to about 53%. The magnetic guiding field was tuned to optimize the energy distribution of the positrons and not the intensity. But all this does not explain the dramatic loss in intensity by much more than an order of magnitude. The source moderator may well cause these losses. Its performance is very sensitive to impurities. On the other hand a large number of factors could reduce the nominal purity of the used copper.

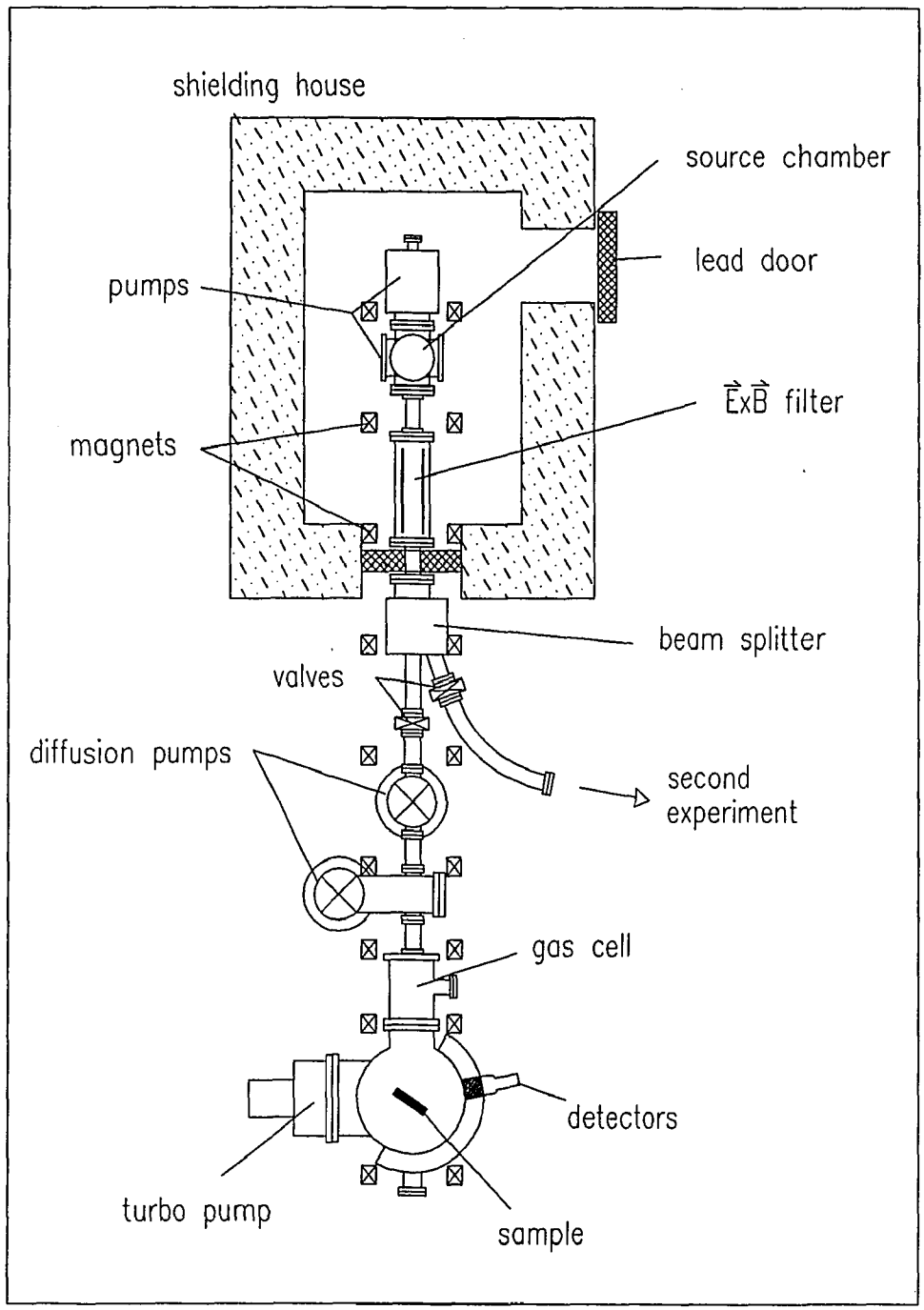

Figure 2.15 — Schematic view of the positron beam source and transport region as seen from above. The very "hot" source is shielded by the "blockhouse". Slow positrons emanating from the self moderating source are accelerated by an electric field between the source and a grid in front of it. A magnetic guiding field of $\approx 80 gauss$ transports the positrons towards one of two experimental regions (not shown here). In an $\vec{E} \times \vec{B}$ filter the positrons drift upwards and are separated from unmoderated fast positrons and γ-radiation which are blocked off by lead shielding.

Also Carbon may diffuse from the W substrate into the source during the final evaporation or annealing. The investigation of this problem is still underway.

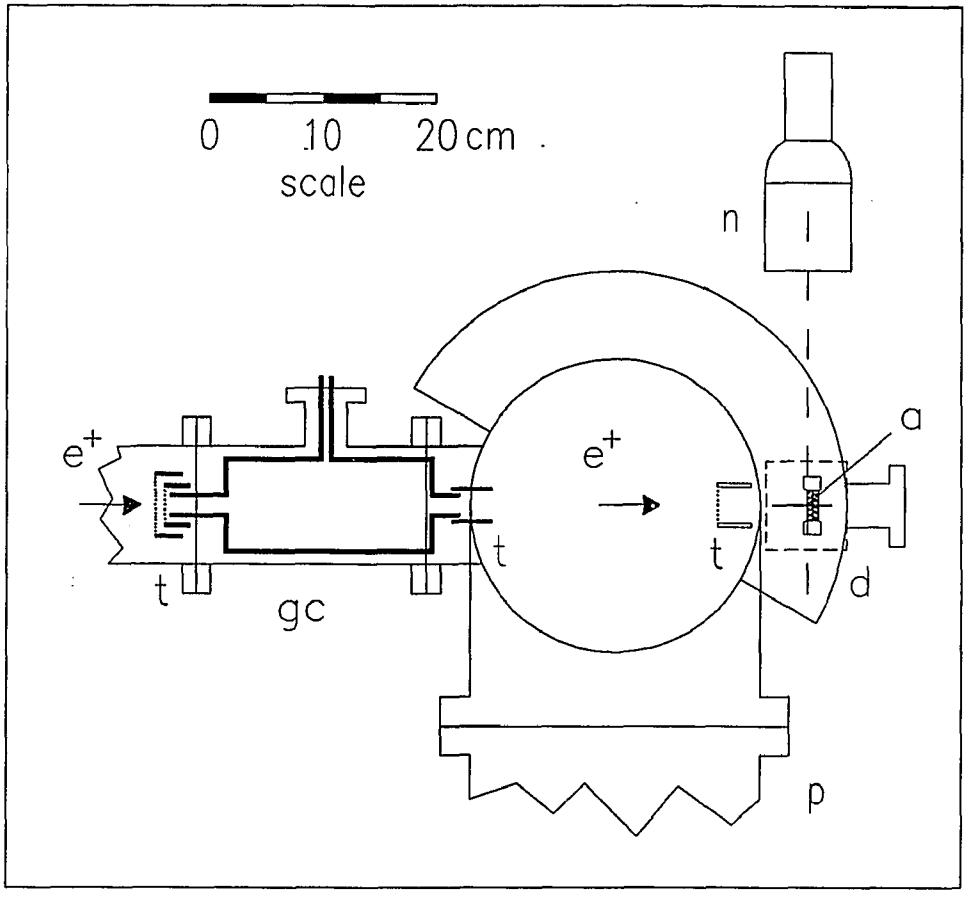

Figure 2.16 — Set up to measure the positron beam intensity and its energy distribution. The intensity of the $511keV$ annihilation peak of a spectrum measured with a NaI (n) scintillator is registered. Positrons with a momentum large enough to pass the potential barrier (gc) reach the annihilation plate (a). Various grids and tubes (t) improve the applied electric fields. (p) is a large turbo molecular pump. (gc) is normally used as the gas cell to form Ps. For the positron transmission experiments the cell is evacuated.

The positron intensity and the energy distribution of the beam are measured with a NaI detector (see figure 2.16). The grids and potential barriers at the exit of the gas cell are grounded to let the positron beam through. The positrons will annihilate on the surface of a Channelplate and their annihilation radiation of 511keV can be detected with a NaI detector placed 14″ from the plate. The

distance has to be kept large in order to prevent pile up effects in the electronics. The counting rate in an energy window was kept below $10^4 sec^{-1}$ for a fresh source of several million positrons. The detector was calibrated with a γ ray standard of ^{22}Na positioned on the Channelplate in order to obtain an absolute value for the positron intensity. If the potential of a grid in front of the plate is ramped, an integral spectrum of the square of the momentum component parallel to the magnetic guiding field can be measured. If the normal component is small this is a measurement of the energy distribution. Such an integral spectrum of the "longitudinal energy component" of the positrons is shown in figure figure 2.17. The negative of the first derivative of this function shows the distribution of this component (see the insert in figure 2.17). The full width at half the peak height (FWHM) is a measure of how well the beam is tuned. for most of the experimental runs in this thesis the spread was $\Delta E/E = 2\%$.

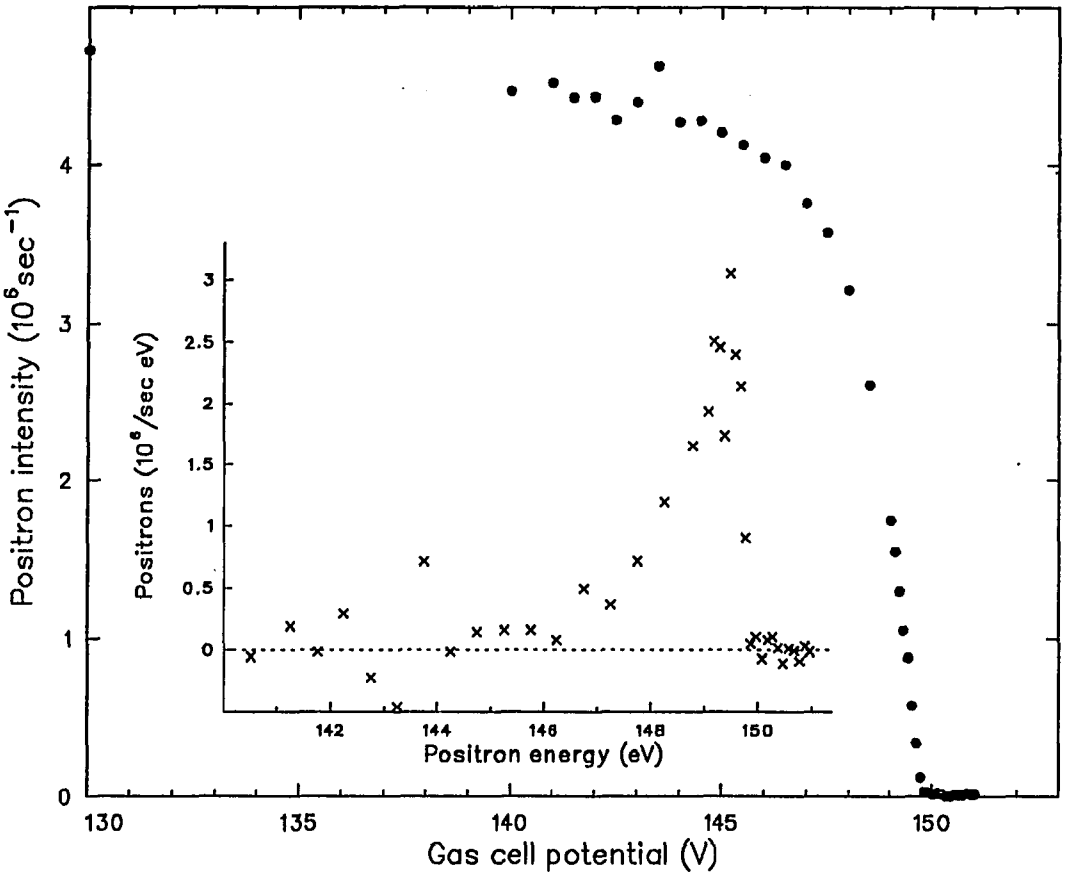

Figure 2.17 — Integral spectrum of the longitudinal energy distribution of the positron beam. The results from a measurement with the NaI scintillator have been corrected for its efficiency. Shown is the transmitted positron intensity as a function of the gas cell potential (•). The insert shows the energy distribution obtained by plotting the negative of the first derivative of the integral data (×). The cut off coincides with the beam energy and the FWHM is less than $2eV$ in this case.

3. The Positronium Beam

A number of positronium (Ps) formation mechanisms have been investigated experimentally prior to this work. Most extensively studied had been the formation of Ps during positron gas atom scattering events.[36] Calculations for Ps formation cross sections have been performed for light atoms like atomic hydrogen and helium and differential cross sections are available.[8,37–39] In experimental investigations Laricchia et.al. found evidence that the differential Ps formation cross section for Ar is also peaked in forward direction for positron energies below $100eV$.[10] In other experiments Ps formation was observed when positrons were incident upon single crystal surfaces at glancing angles.[40,41] A.P. Mills, jr. directed energetic positrons at a thin foil of carbon and could detect Ps as well as the negative ion Ps^-.[42,43] While the positrons pass the foil, they pick up one or two electrons from it to form the Ps or Ps^-. Ps^- has the advantage to be charged and it can be accelerated easily to a desired energy. Then the excess electron would have to be stripped off. This could be accomplished with a laser which is tuned to the ionization energy for Ps^- for example. Another proposed path to obtain Ps is to condense a gas on a very thin foil and to produce Ps in the solid gas layer.[44]

The advantages and disadvantages of each of these methods was weighed against the requirements for a Ps beam capable of supporting reasonable Ps reflection measurements. The Ps beam needed to be as intense as possible. Keeping in mind that the next step after measuring the reflection coefficient for Ps from various surfaces is to search for diffraction peaks, the beam should be monoenergetic and

variable in energy. If that is impossible or not feasible then some kind of energy detection system has to be employed. Finally it should be mentioned that the better the Ps formation process is understood the more resources can be concentrated on the reflection measurement rather than the development of Ps beams.

In the sections of this chapter I will briefly review some of the properties of Ps as they become important for my work. I will discuss in more detail the various Ps production mechanisms and specially the formation in a gas, which was the choice for this work. Theoretical calculations of Ps formation cross sections in helium will be reviewed briefly. I will present the design of the gas cell and estimate the effects of the various parameters on the Ps beam characteristics. The Ps detection system will be explained together with measurements of the Ps beam performance as a function of the gas cell pressure and the positron energy. Most measurements last on the order of a half-life of the ^{64}Cu source. Hence the results need to be corrected for the changing beam intensity of positrons and thus Ps atoms during the experiments. I will cover this topic with the description of the detector system.

3.1. Positronium (Ps)

Positronium (Ps) is the atom-like bound state of an electron and its antiparticle the positron. Even more so than the simplest atom, H, Ps is an ideal proving ground for test on QED. It is a purely leptonic two body system and involves only weak electromagnetic interactions. No strong forces complicate the calculations as is the case for hydrogen. Research on Ps up to date in theory as well as in experiments has been covered in a number of review articles.[14,45,46] In Ps the positron replaces the proton of H. The two main differences of the two atoms are the very different masses of the proton m_p and that of the positron, which is equal to that of the electron m_e, and the fact that the positron is the antiparticle of the electron.

The reduced mass of the two body system

$$\mu = \frac{m_a m_b}{m_a + m_b} \tag{66}$$

yields a value for Ps of half that for H, which will reduce the energy levels of Ps to half the values of H. Thus the binding energy is 6.8eV and the first excited state level lies 5.1eV above the ground state.

The spins of the electron and the positron can align in two orientations — parallel or antiparallel — to add up to a total spin of 1 for triplet (ortho) Ps or to a 0 spin for singlet (para) Ps respectively. Because positron and electron are the antiparticle of each other, Ps annihilates into two ore more γ-rays. A one γ-ray annihilation is forbidden for free Ps because momentum and energy cannot be conserved at the same time. Annihilations into larger numbers of photons are restricted by selection rules. Charge conjugation requires that a Ps atom with the angular momentum l and total spin s can annihilate into n photons only if

$$(-1)^{l+s} = (-1)^n. \tag{67}$$

Thus the singlet ground state of Ps can only annihilate into even numbers of γ-rays, while its triplet counterpart disintegrates into odd numbers of photons starting at three. This was first derived from the principle of invariance under spacial rotation and charge conjugation by Yang.[47] A number of lowest order Feynman diagrams describing these annihilations are shown in figure 3.1.[46] These diagrams alone illustrate that the annihilation rate for the triplet state will be much reduced compared to the singlet state, or the lifetime is much longer by a factor of the coupling constant for the electromagnetic interaction α. In fact, as was calculated by Ore and Powell in 1949,[48] the ortho-Ps lifetime in ratio to the para-Ps lifetime is much longer than this simple factor predicts. The singlet Ps lifetime had been calculated by J. Pirenne in 1944 in his thesis and by J.A. Wheeler[49] to be

$$^1\tau = 2\frac{\hbar}{m_e c^2}\frac{1}{\alpha^5} \approx 0.125 nsec. \tag{68a}$$

Ore and Powell calculated for the triplet lifetime a value of

$$^3\tau = \frac{9\pi}{2(\pi^2-9)}\frac{\hbar}{m_e c^2}\frac{1}{\alpha^6} \approx 141.8 nsec. \qquad (68b)$$

Since then higher order radiative corrections have been added to these values which can also be expressed in higher order Feynman Diagrams. Recent high precision measurements indicate, that there might be a small discrepancy between theoretical and experimental values for the triplet state.[50] Even higher orders of the coupling constant α are involved in annihilations into more than 3γ-rays, making those events very rare. For all practical purposes only 2 and 3γ events need to be considered.

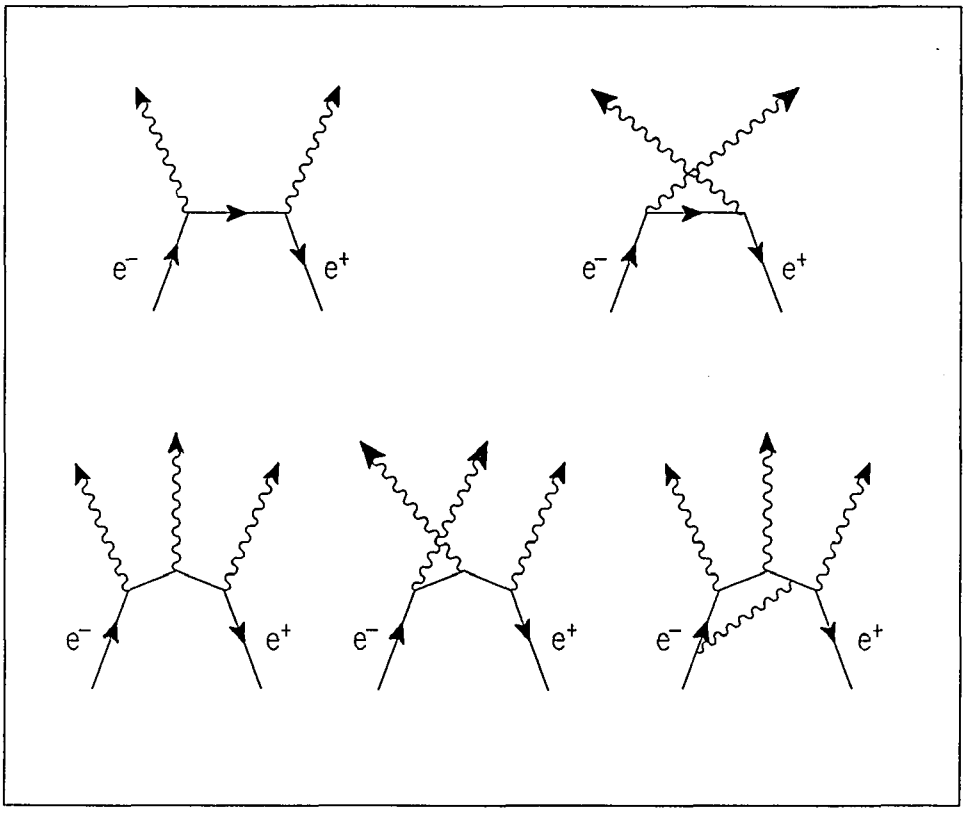

Figure 3.1 — Low order Feynman diagrams for two and three γ annihilations of Ps atoms. The last one illustrates one contribution to radiative corrections of the order α.

Annihilation rates have been calculated also for excited states. In the $n = 2$ state the situation is very different for the P state and the S state. For the 2P state

optical transition rates to the 1S state are very much faster than the calculated annihilation rates, making the former the main channel of depletion of this state. The decay of 2S Ps into the ground state is a forbidden transition ($\Delta l = \pm 1$). The lifetimes for triplet and singlet state $1.14\mu sec$ and $1.0nsec$ respectively, much longer than the appropriate ground state values, which can be explained by the further separation of the wavefunctions of electron and positron. Bohr's simple model of hydrogen like atoms predicts a radius of $n^2 = 4$ times that of the ground state. In figure 3.2 an energy level schematic of the ground state and $n = 2$ state Ps is reproduced.[51] Also listed are the annihilation and transition lifetimes for the various levels.

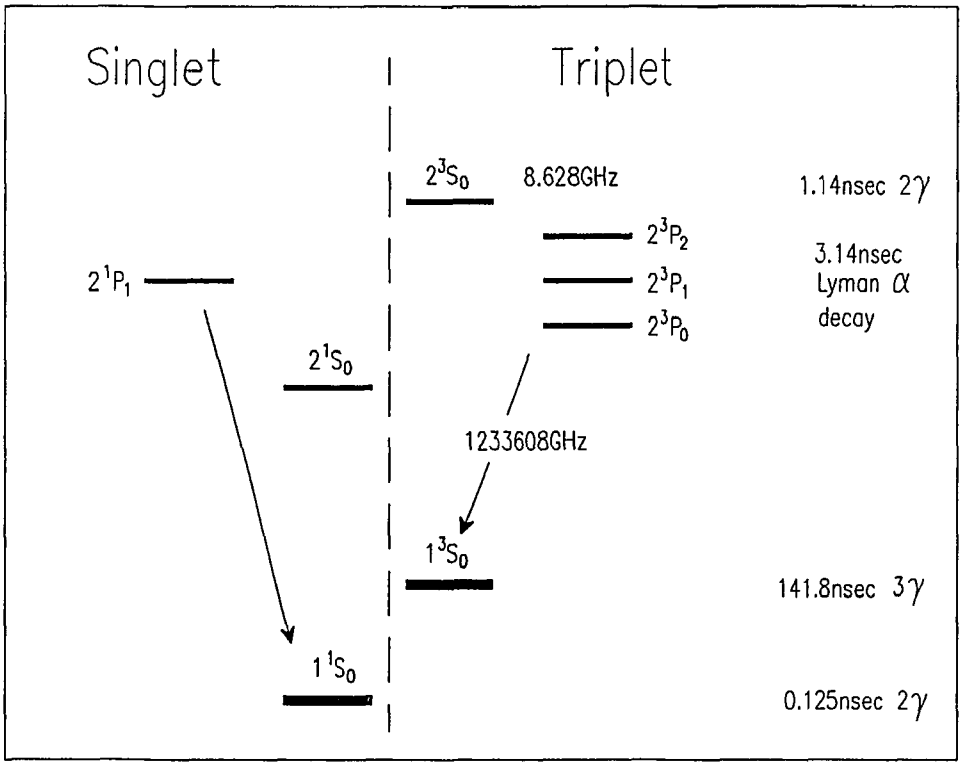

Figure 3.2 — Schematic of the energy levels $n = 1$ and $n = 2$ for Ps. Included are annihilation or decay rates (on the right side).

The conservation of energy and momentum requires for 2γ annihilations that the photons carry equal energy ($E_\gamma = m_e c^2 \approx 511keV$) and opposite momentum

in the rest frame. Positron and electron velocities occurring throughout this work are small fractions of the speed of light (c) and cause only minute deviations of the colinearity of the two photons in the lab frame. A monoenergetic γ-ray spectrum is the result. However, a broad range of energies are allowed in three γ annihilations of ortho-Ps. Only the total energy and momentum need be conserved. The ideal spectra for the two γ annihilations would be a delta function at $511keV$. The three γ case is shown in figure figure 3.3.[52] Adkins included the $O(\alpha)$ correction into his calculation of this differential decay rate.[53] The distribution was measured most accurately by Chang and collaborators.[54] In a measurement these spectra will be convoluted with the finite the detector resolution. Also various photon atom interactions, like compton events, will cause additional features because not all of the γ-ray energy is deposited in the detector.

Once the Ps approaches a solid surface like a metal, the probability for the positron to annihilate with an electron from the surface increases dramatically. The "density" of the electron bound to the positron (one in a sphere of radius $2a_0$) becomes comparable to that of the electrons of the solid. On the order of half of the surface electrons will have a spin opposite to that of the positron. Two γ annihilations will become the predominant channel.

I take advantage of this effect in order to detect the Ps atom. It will strike a Channelplate and get trapped in the tiny holes, where it rattles around until the positron annihilates with a surface electron rather than with the electron it is bound to. Also some Ps may be converted to the singlet state by spin exchange processes and subsequently decay much faster. This part can be detected with the same apparatus.

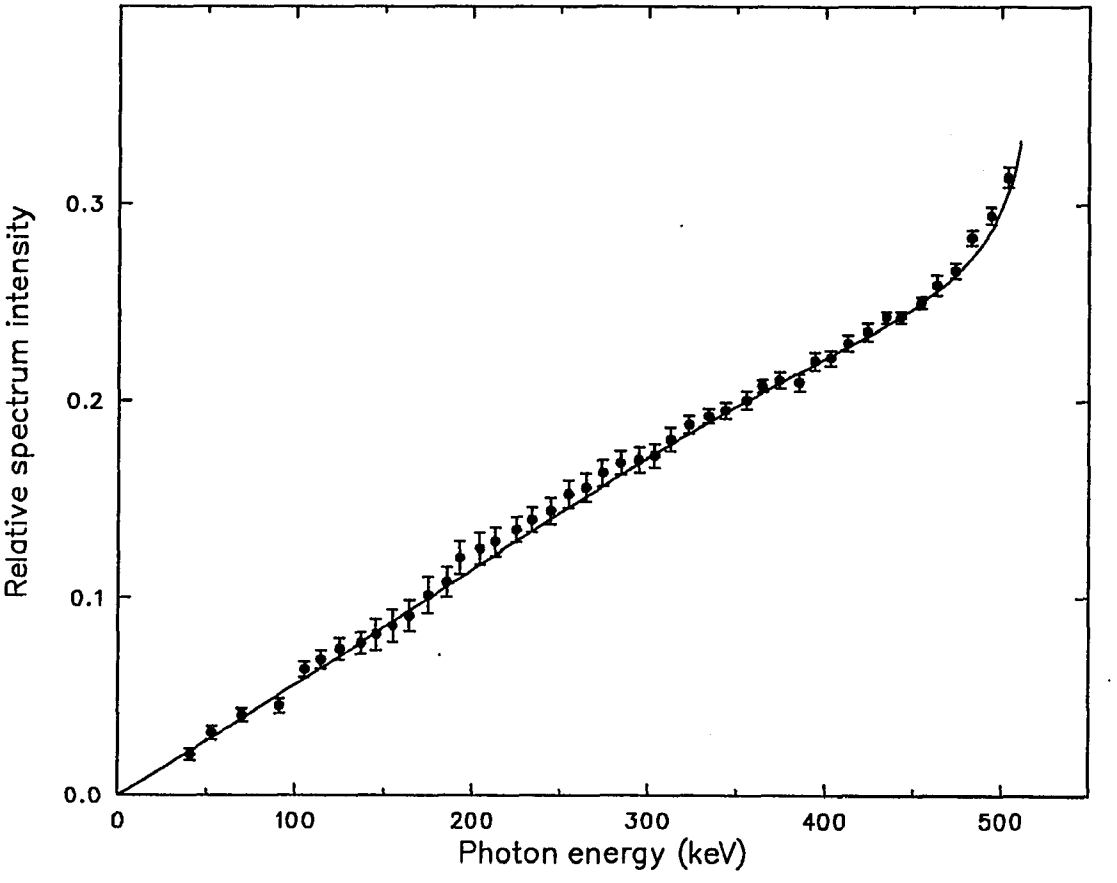

Figure 3.3 — Spectra in the rest frame for 3γ annihilations of Ps. Plotted is the intensity of photons in the energy region ΔE and at the energy E versus the photon energy in units of $m_e c^2$. (from Ref. 53). The data are from Ref. 54.

3.2. Formation of Ps

When positrons are moderated and leave the solid, a fraction of them will pick up an electron while passing the surface to form positronium. A.P. Mills, Jr. for example measured the energy distribution of Ps atoms emanating from a Cu(111) surface coated with a monolayer of S.[55] He found a thermal distribution, indicating that the positrons enter the solid, thermalize and pick up an electron on their way out. Later, in 1981, he directed a $400eV$ positron beam onto a 40Å carbon foil and detected Ps^- ions coming from the opposite side.[43] The ions were accelerated by an electric field and a blue shifted γ-ray line was observed. The production efficiency was determined to be $\epsilon = (2.8 \pm 0.3) \times 10^{-4}$. To separate an electron from Ps^-

an energy of only $E_b = 0.3266eV$ is sufficient.[49] The 2γ annihilation lifetime is $\tau_{2\gamma}(Ps^-) = 0.502nsec$. Since Ps^- is charged, it can be accelerated to a desired energy. Then it would have to be stripped off its second electron in such a way that triplet Ps remains. More promising is that Ps is also formed when fast positrons traverse the same thin foil of carbon.[43] The Ps atoms move roughly in forward direction with an energy distribution that decreases approximately as $E^{-3/2}$. The efficiency is about 0.5% times the detector solid angle of the incident positron flux. The broad spectrum of energies makes a time-of-flight measurement necessary for experiments such as Ps diffraction. In yet another experiment Gidley et.al. observed Ps formation when a beam of positrons strikes single crystal surfaces at glancing angles.[40,41] An energetic positron beam ($\leq 400eV$) was scattered off surfaces of Al(110) and Cu(100) at glancing angles around 6°. Up to 5% of the incident beam was neutralized by forming Ps, which came off in a cone of $\approx 20°$ FWHM. No energy analysis was performed but the authors argue that the process is nearly elastic on kinematic grounds. Most of the angular spread can be explained by the additional momentum parallel to the surface from the captured electrons. In figure 3.4 these methods of forming Ps are outlined schematically.

By far the greatest control over positron atom interactions can be exerted when positrons traverse a dilute gas. The Ps formation process involves only a single atom and its small number of electrons in the outer shells. The He and H atoms are the simplest cases available for cross section calculations. Positrons collide with the very much heavier gas atoms and – if energetic enough – can pick up an electron from the atom via charge transfer. The Ps atom retains the energy distribution of the positron to a large degree. Theoretical calculations indicate that the differential formation cross section is forward directed.[37,8,38,39] Thus a monoenergetic beam of positrons will result in a monoenergetic "beam" of Ps atoms. Figure 3.5 illustrates the principle of a Ps beam based on a "gas cell". for this work the gas cell method

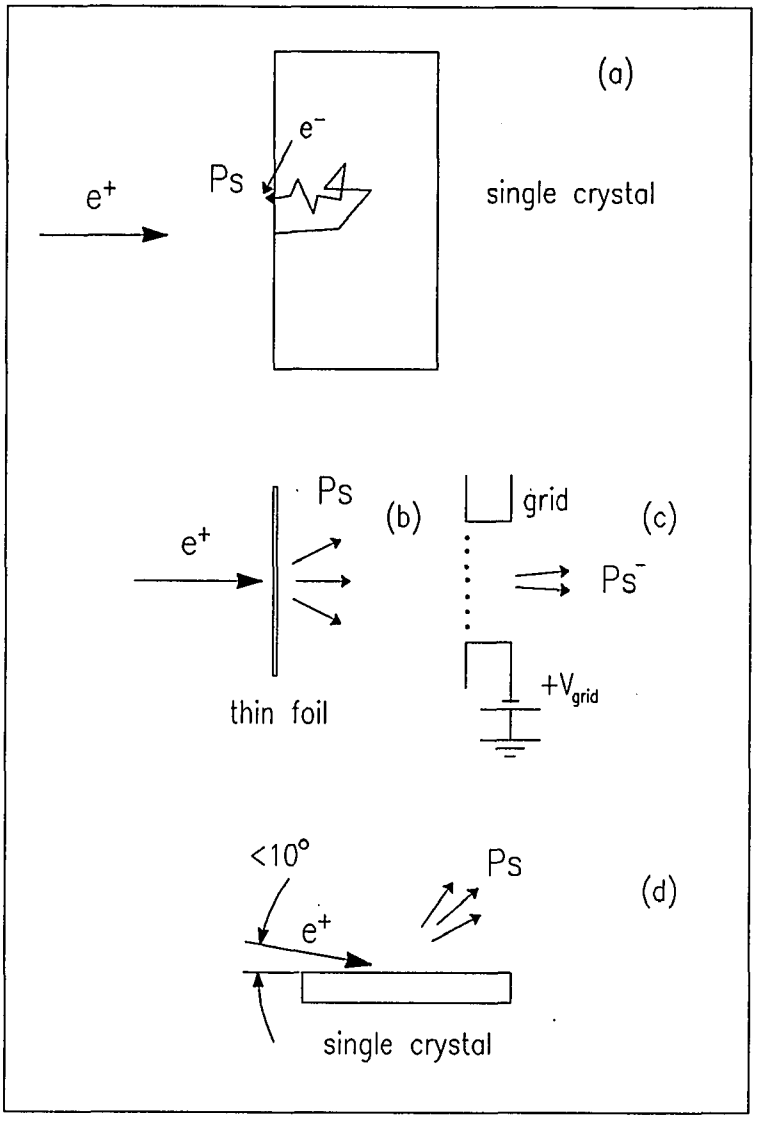

Figure 3.4 — Various methods of generating beams of Ps atoms. They involve reemission of thermalized positrons from surfaces where they may pick up an electron (a); fast positrons striking thin foils of carbon to form Ps (b) and Ps^- which can be accelerated and then has to be neutralized (c); and last a collimated beam of positrons scattering from surfaces of single crystal surfaces at glancing angles (d).

was chosen over the other methods because no time-of-flight apparatus was required and the efficiency was expected to be on the order of $< 1\%$ in a narrow cone. Also the other approaches were still in a rather developmental stage and involved more

technological challenges. In the following I will discuss the gas cell approach in more detail.

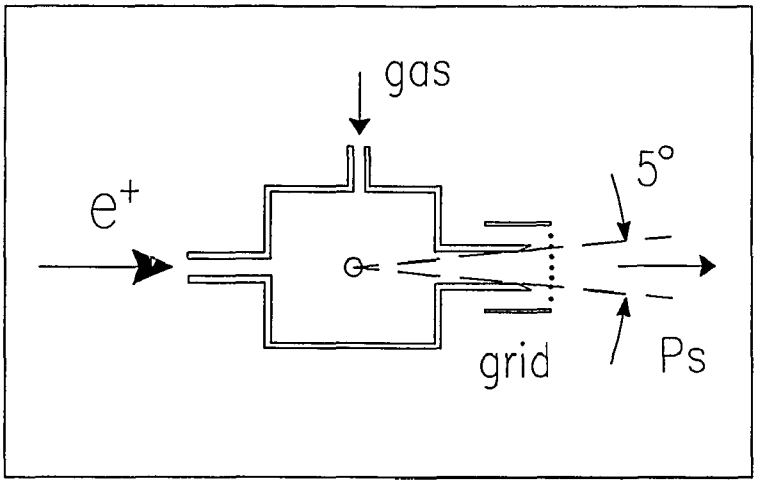

Figure 3.5 — Schematic of Ps formation in a gas cell via a charge exchange reaction. A large fraction of the Ps is formed in a narrow cone of about 5°.

When positrons (e^+) collide with atoms of the kind "A", a number of interactions can take place, provided the positron atom system contains enough energy. They are listed in table 3.1 below. The corresponding energy thresholds for He and for Ar are included in the table. The reactions are listed according to the energy threshold beyond which they are allowed energetically. Associated with every channel is a partial cross section and a different differential cross section. Channel number 2 is the primary Ps formation channel with the largest cross section. The other two channels that involve the formation of Ps are considered to be secondary and cause an energy contamination of the primary beam. In the following let me consider each reaction in a little more detail as far as it is relevant for the Ps beam.

Elastic collisions (channel 1) can occur at any energy. Since the mass of the positron is so much smaller than that of the gas atom (for example He or Ar, the two gasses used in this work), the main outcome of such a collision is a directional

Table 3.1: Positron atom interactions

#	Reaction channel	Threshold energy (eV)	
		He	Ar
1	$e^+ + A \rightarrow e^+ + A$	0.0	0.0
2	$e^+ + A \rightarrow Ps + A^+$	17.7	8.9
3	$e^+ + A \rightarrow e^+ + A^*$	21.2	11.8*)
4	$e^+ + A \rightarrow Ps^* + A^+$	22.8	14.0*)
5	$e^+ + A \rightarrow e^+ + e^- + A^+$	24.5	15.7
6	$e^+ + 2A \rightarrow Ps + A^* + A^+$	38.9	20.7*)

*) The first excited state $n = 2$ is meant for Ps as well as the atom A.

change of the positron momentum. In the center of mass (CM) frame this is always the case. The CM frame almost coincides with the lab frame due to the extreme mass ratio $M/m \approx 7.3 \times 10^3$ for He and about 10 times larger than this for Ar. M and m are the masses of the gas atom and the positron.

$$\vec{v}_{cm} = \frac{m\vec{v}_p + M\vec{v}_A}{m+M}, \tag{69a}$$

$$\vec{v}_p^{\,cm} = \frac{M}{m+M}(\vec{v}_p - \vec{v}_A) \tag{69b}$$

where $\vec{v}_p$ and $\vec{v}_A$ are the positron and atom velocities respectively in the lab frame, or with the superscript ^{cm} in the CM frame. At room temperature ($293K$) the most

likely velocity in a gas is

$$v_A = \sqrt{2\frac{kT}{M}} \approx \sqrt{\frac{50meV}{7.3 \times 10^3 m_e}} \approx 1.1 \times 10^3 \frac{m}{s} \tag{70}$$

for He and $\approx 3.5 \times 10^2 m/s$ for Ar. A positron with a kinetic energy of 1eV speeds through the gas with

$$v_p \approx 1.41\sqrt{\frac{eV}{m_e}} \approx 4.2 \times 10^5 \frac{m}{s} \tag{71}$$

and 10 times faster at 100eV. The 1eV positron moves about 200 times faster than the CM system. The ratio becomes even larger for more energetic positrons or when they collide with Ar atoms. In this case a "head on" collision was considered.

In "head on" collisions the transfer of energy peaks. I consider such a case to estimate the amount of energy transferred ΔE. As long as $Mv_A \geq mv_p$ (i.e. the positron energy $E_p \leq 183eV$ for He collisions) the CM frame moves towards the positron and the energy change is

$$\begin{aligned} \Delta E =& |E_f - E_p| = \frac{1}{2}m|\vec{v}_f^2 - \vec{v}_p^2| \\ =& \frac{1}{2}m|(|\vec{v}_p^{cm}|\vec{e}_f + \vec{v}_{cm})^2 - \vec{v}_p^2|, \end{aligned} \tag{72}$$

where $\vec{e}_f$ is a unit vector representing the final direction of the positron in the CM frame. With the definition $R = m/M$, the relative energy change of the positron is

$$\frac{\Delta E}{E_p} = 4R\left|1 - \sqrt{\frac{kT}{RE_p}}\right|. \tag{73}$$

In table 3.2 a couple of cases are listed. In all cases ΔE is small compared to the energy of the positron. These calculations still hold for the inelastic channels like the Ps formation reactions. Thus effects due to recoil can be neglected except for changes in the direction of the positron momentum.

Several of the inelastic channels of e^+ atom collisions result in the formation of Ps. The desired, and primary, one of them is listed under number 2 in table 3.1.

$$e^+ + A \rightarrow Ps + A^+ \tag{74}$$

Table 3.2: Relative energy change in elastic "head on" collisions

E_p (eV)	$\Delta E/E_p$ (10^{-3})	
	He	Ar
1	6.9	2.3
100	0.2	0.18

with a total cross section of σ_{Ps}. This cross section has been measured for noble gases and many other molecular gases.[56-60]

In figure 3.6 σ_{Ps} for He and Ar is shown.[56,61,62] For the purpose of making a Ps beam it is also of importance to know the differential cross sections. For the differential Ps formation cross section some calculations were made for light atoms as H, He and Li.[8,38,39,63] The calculated values are strongly peaked in forward direction parallel to the incident positron. The width of the peak narrows with increasing positron energy in the examined energy range from threshold to about $100eV$ some of which are reproduced in figure 3.7. The energy of the produced Ps is simply that of the positron minus the amount necessary to form the Ps atom, and the spread of energies is defined by that of the incident positron beam, given a negligible effect of the recoil. This argument and the forward directed cone of the differential cross section were the reasons to proceed with a gas cell as the source of the Ps beam.

The calculations of differential cross sections are not straight forward because even for atomic hydrogen three bodies are involved. The situation becomes even

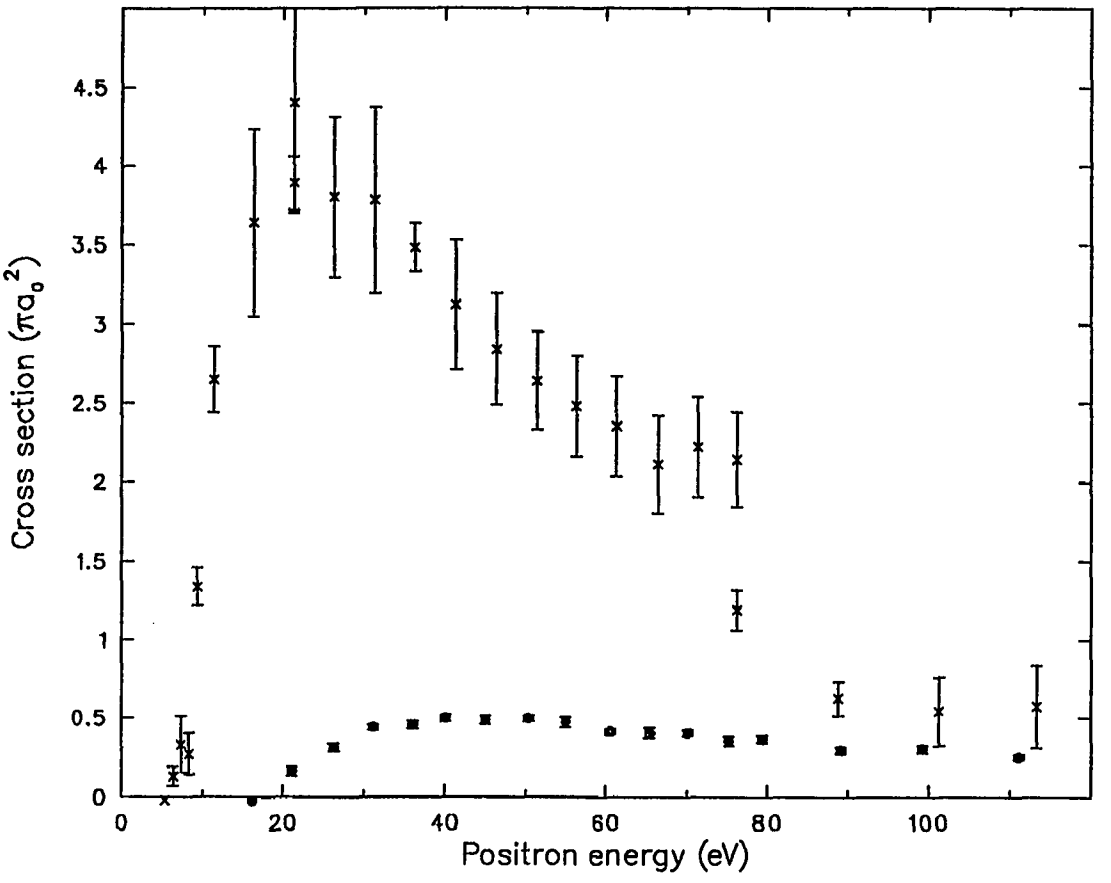

Figure 3.6 — Total Ps formation cross section as a function of the incident positron energy for He (•) and Ar (×) (from Ref. 56, Ref. 61 and Ref. 62). The cross sections are given in units of $\pi a_0^2 \approx 0.879 \times 10^{-16}\text{cm}^2$.

more complicated for atoms with more electrons than He. In general the matrix element of the initial wavefunctions of the positron and the atom and the Ps wave function for the final state is calculated with the Coulomb potential for the interaction between the various charges. To arrive at some computable solution various assumptions can be made. The first order Born approximation is the simplest of all but it breaks down at low energies. More sophisticated calculations include polarization effects caused by the positron when it approaches the atom. The minima at angles near 30° arise from the opposite forces between the positron and the nucleus on the one hand and the positron and the electron(s) on the other hand. They tend

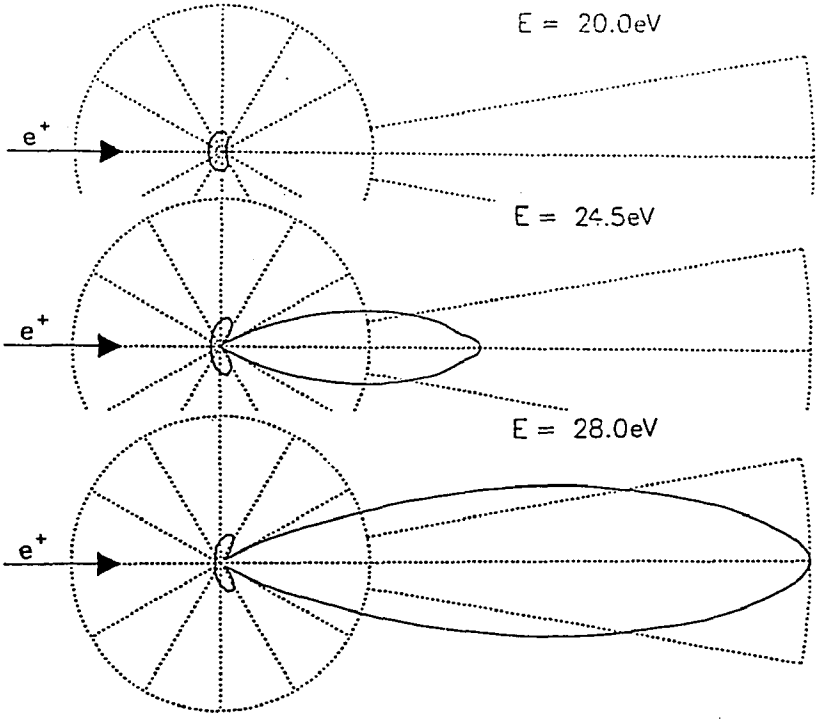

Figure 3.7 — Differential Ps formation cross section for various energy positrons. The spokes of the wheel represent 30° steps for the inner circle and 10° for the wedge. The inner circle represents an value of 0.5π per sterad and the outer circle is 2π per sterad. The data are from Ref. 38.

to become more pronounced with increasing energy of the positron relative to the atom.

In He and in Ar as well as in many other gases the inelastic process requiring the smallest amount of energy is Ps formation in the ground state. A small energy gap exists in which this reaction is the only possible one. This is the Ore gap. The energy threshold for Ps formation is determined by the energy required to ionize the gas atom (E_I) and the binding energy ($E_b = 6.8eV$) gained when Ps is formed ($E_{th} = E_I - E_b$). The threshold for the formation of excited state Ps lies 5.1eV above the ground state threshold since the binding energy if $n = 2$ Ps* is only $6.8eV - 5.1eV = 1.7eV$, and even less for higher excited states. In this 5.1eV gap

the Ps energy distribution depends only on that of the incident positrons (given a negligible recoil contribution). Once Ps* can be formed (channel 4 in table 2.1), energy "contamination" of the Ps becomes possible. Some calculations exists for the formation of excited state Ps ($n = 2$) formation in H and He.[64,65] The calculated cross sections relative to the ground state cross sections is reproduced in figure 3.8 for the 2S fraction as well as for the 2P part. The singlet fraction of the $n = 2$ Ps will either decay to the singlet ground state and annihilate rapidly (the 2^1P_1 state) or annihilate directly in a relatively short time of $\tau(2^1S_0) = 1.0nsec$. In either case these Ps atoms will not influence the measurement. A different story pertains to the triplet $n = 2$ states. Only the 2^3P states can decay radiatively to the ground state, while selection rules prohibit this for the 2^3S_1 state ($\Delta l = \pm 1$). This contributes to the meta stable nature of the 2^3S_1 state with a half-life of $\tau = 1.14\mu sec$ which is about 8 times longer than the ground state lifetime. On its own this fact would greatly increase the ratio of $n = 2$ Ps compared to ground state Ps, except for two other factors. First it can be reasoned that any excited state of Ps would increase the size of the atom (the Bohr radius increases by an factor of n^2 compared to the ground state). Collision cross sections can be expected to be much increased and due to the small binding energy of $n = 2$ Ps ($1.7eV$) much of it will break up inside the formation region. The second argument involves the lower kinetic energy of Ps* which is reduced by the amount necessary for the excitation. The increased flight time to a target will counteract the larger lifetime somewhat. Consequently I assume that the fraction of excited (and thus lower kinetic energy) Ps* in the beam that reaches the detectors will be less than 5%. T. Griffith and his collaborators are currently investigating the contamination of the Ps beam Ps*. He indicated recently that this value may be an underestimate.[66]

A second source of Ps with different kinetic energies than the "primary" beam of Ps becomes possible when the positrons can undergo inelastic collisions

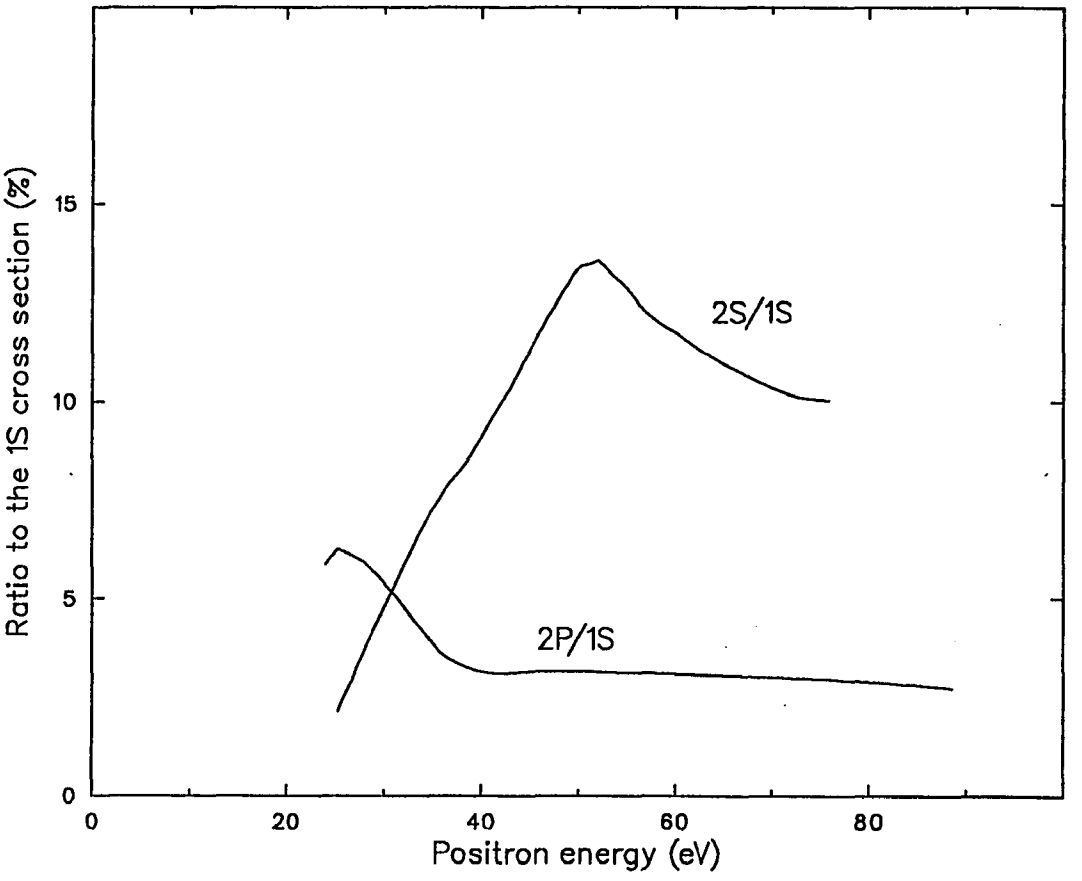

Figure 3.8 — Ratios of the various Ps formation cross section for the first excided states (2S and 2P) to the ground state cross section (see Ref. 65).

like the excitation of an atom and still retain enough energy to form Ps in a second collision. This channel opens up at a positron energy of $38.9eV$ for He and at $20.7eV$ for Ar. Ps atoms will be produced with a kinetic energy reduced by the excitation energy of the atom ($21.2eV$ and $11.8eV$ respectively). This effect can be regulated by keeping the gas pressure low enough to make multiple collisions unlikely.

If the primary beam of positrons has an intensity I_0 then the number of positrons that collide with a gas atom in the volume element $dV = Adx$ is

$$dI = -I(x)\sigma_{in}ndx \tag{75}$$

where n is the density of gas atoms and σ_{in} the sum of all inelastic cross sections for positron atom collisions, which are the values for Ps formation atom excitation

and its ionization.

$$\sigma_{in} = \sigma_{Ps} + \sigma_{ex} + \sigma_{ion} \tag{76}$$

In elastic collisions the positron energy does not change (neglecting the recoil effect). Only the distribution of the momentum components parallel and perpendicular the the magnetic guiding field changes. Similar ansätze can be made to obtain the functions for the number of Ps atoms formed in single and double collision events. The results are given a fixed formation region of length L

$$I_{Ps} = I_0 \frac{\sigma_{Ps}}{\sigma_{in}} \Big(1 - exp\{-n\sigma_{in}L\} \Big) \approx n\sigma_{Ps} L I_0; \qquad n\sigma_{in}L \ll 1 \tag{77}$$

for Ps formation in just one collision, and

$$\begin{aligned} I^2_{Ps} =& I_0 \frac{\sigma_{Ps}(\sigma_{in} - \sigma_{Ps})}{\sigma^2_{in}} \Big[1 - (1 + n\sigma_{in}L) exp\{-n\sigma_{in}L\} \Big] \\ \approx& \frac{1}{2} (n\sigma_{Ps}L)^2 \frac{(\sigma_{in} - \sigma_{Ps})}{\sigma_{Ps}} I_0; \qquad n\sigma_{in}L \ll 1 \end{aligned} \tag{78}$$

for Ps formation in a second collision after an inelastic event other than Ps formation. The next order in the expansion of the exponential term will present an estimate of the error in these values. Choosing low pressures and short formation regions will clearly reduce contamination of a Ps beam by Ps atoms produced after multiple collisions. If I consider the case for $50eV$ positrons directed into a $L = 20cm$ long formation region filled with $10^{-3}torr$ He ($n \approx 3.5 \times 10^{13} cm^{-3}$) for example, I get[67]

$$\begin{aligned} \sigma_{in} =& \sigma_{tot} - \sigma_{el} = (1.1 - 0.2) \times 10^{-16} cm^2 = 0.9 \times 10^{-16} cm^2, \text{ and} \\ \sigma_{Ps} =& 0.48 \times 10^{-16} cm^2 \end{aligned} \tag{79}$$

and the Ps formation fraction in a single collision and in a second collision are roughly

$$\begin{aligned} I_{Ps}/I_0 &= 3.4\%, \text{ and} \\ I^2_{Ps}/I_0 &= 4.9 \times 10^{-4} \approx 1.5 \times 10^{-2} I_{Ps}. \end{aligned} \tag{80}$$

During the flight from the formation region to a detector ($D \approx 40cm$) this ratio improves even further by a factor of 2.3 due to the larger energy loss in a double collision process ($50eV - 17.7eV$ vs. $50eV - 38.9eV$ see table 3.1).

This is not the only problem associated with large gas cell and high pressures. Ps atoms themselves have some probability of colliding with the gas atoms and consequently be deflected from their initial flight path or break-up can occur. Some calculations exist for Ps-H[68,69] and Ps-He[70,71] scattering, but not for Ps-Ar cross sections. Arguments similar to those for the break-up of Ps* can be made. The wave function of Ps extends much further than the classical size of a positrons. Thus the total cross section for Ps atom interactions should be larger than that for positrons. Incorporating such a break-up cross section σ_{br} (which may include the elastic cross section) into the result for Ps formation yields

$$I_{Ps} = \frac{\sigma_{Ps}}{\sigma_{in} - \sigma_{br}} I_0 \Big(exp\{-n\sigma_{br}L\} - exp\{-n\sigma_{in}L\} \Big) \qquad (81)$$

Such a break-up cross section could be estimated by measuring the Ps intensity as a function of the pressure in the gas cell. B.L. Brown has attempted to extract Ps-He cross sections from his data on Ps formation in a gas cell[72] Direct measurements are currently being carried out at University College London.[73]

Neglected in all these considerations are the effects of elastic scattering of positrons from gas atoms. These collisions will convert longitudinal momentum (parallel to the magnetic guiding field) into transverse momentum. As a result more Ps will be formed in directions away from the sample and the detectors causing a reduction in the detected Ps intensity. This effect will become stronger with increasing pressure. With the above detection system I cannot distinguish between losses in the Ps rate due to elastic scattering and those induced by Ps break-up.

3.3. The Experimental Apparatus

The design of a gas cell that was used in this work is shown in figure 3.9. Also shown is the arrangement of the sample in the Ps beam and the detection system. The monoenergetic beam of typically $150eV$ positrons is directed into a stainless steel cell of $22cm$ length, which can be filled with the interaction gas. Ar at $10^{-3}torr$ was used for all reflection measurements because of its larger total Ps formation cross section relative to He. In order to make comparisons with some calculations on the efficiency of the cell possible I used He in some Ps formation measurements. Baffles on either side of the cell restrict the gas flow. Two $940l/s$ (for air) for diffusion pumps with cold traps provide differential pumping on the source side of the gas cell, and a large turbo molecular pump ($1500l/s$ for N_2) maintains a background pressure in the experimental chamber of 1% of that in the gas cell, which is mounted right on to the gas cell. Rather poor vacuum conditions for modern standards had to be accepted in order to limit losses of Ps intensity due to decay in flight. Since inert noble gasses of 99.995% and better nominal purity are used the situation is not as bad as a typical pressure of $10^{-5}torr$ would indicate.

The cell can be floated electrically to the potential V_2 to change the kinetic energy of the positrons and thus the Ps energy. This method was chosen rather than adjusting the complete beamline for every positron energy. Potential barriers in the form of two 90% optical transmission grids fabricated from tungsten at the entrance of the cell (V_1) and a tube at the exit (V_3) control the flux of positrons. The second of the grids is connected to the gas cell, while the first one can be grounded to permit the positron beam into the cell ("beam on" mode), or when a voltage V_1 is applied to inhibit them from doing so ("beam off" mode). The implementation of two grids makes the electric field more homogeneous. A voltage V_3, similar to V_1, is applied to the tube to prevent positrons from entering the experimental chamber.

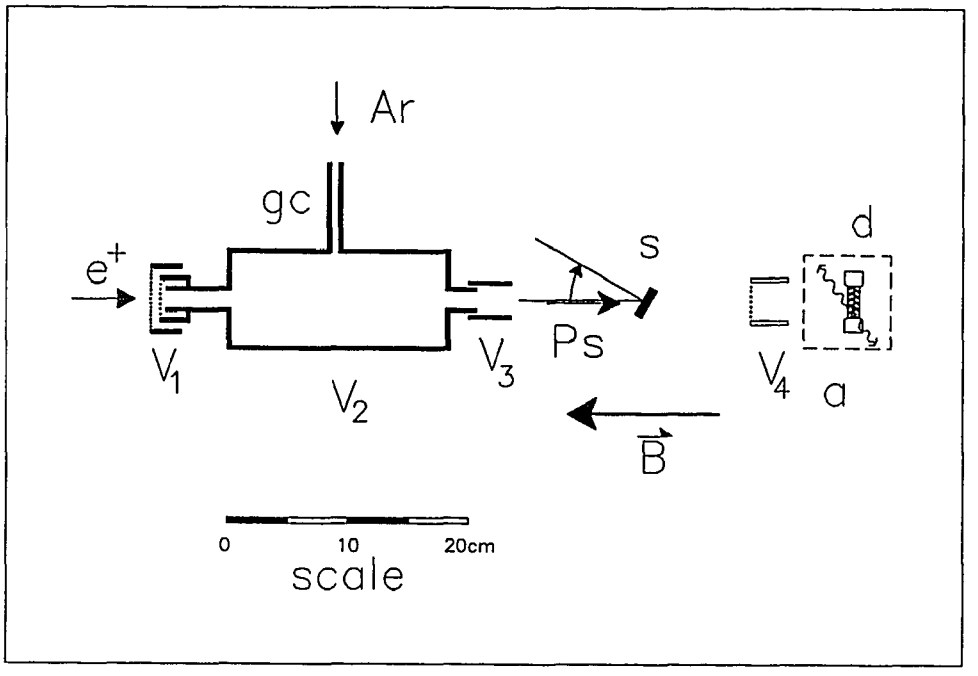

Figure 3.9 — Top view of the gas cell and the experimental chamber. Positrons enter the gas cell, which is held at a potential V_2 above ground, and some form Ps, via an electron transfer reaction with gas atoms in the cell. A potential V_3 repels the positrons at the end of the cell while the Ps passes an aperture (combined with V_3) and strikes a rotatable sample in the center of the experimental chamber. A detection system can be rotated around the sample for angle dependent reflection measurements of Ps, or, with the sample removed it can monitor the incident Ps beam intensity. Another potential barrier, V_4, bars any positrons from the detection region that may result from break-up of Ps. Pb and W shields reduce the γ-radiation background. (Details of the detector are shown in figure 3.10.)

For a $150eV$ positron beam a typical "beam off" voltage is $200V$ on the first grid as well as the tube.

A rotatable sample can be moved into the Ps beam $15cm$ after the gas cell. A detection system (or short the detector) can be rotated around the sample at a radius of $16cm$. Thus any Ps atom that strikes the sample and reaches the detector will fly across the same distance of $31cm$, independent of the chosen sample angle and detector position. The angle between the axes from the gas cell to the sample position and from the sample to the detector is defined as ψ. In the $\psi = 180°$ position and with the sample removed the detector monitors the Ps intensity, or if so desired the positron beam. The magnetic guiding field for the positrons extends

beyond the experimental chamber for the latter purpose and also to keep positrons from Ps break up away from the detector in the case of $\psi < 180°$.

The detector (see figure 3.10) consists of a plate (a Channelplate (CEMA), referred to as the annihilation plate) inside the vacuum system, and two scintillators outside of it. Positrons or Ps atoms strike the plate and annihilate The annihilation radiation can be detected by the scintillators in coincidence. The annihilation plate is mounted on a rotatable cart that extends into a protrusion (bulge) of the experimental chamber. A combination of a tube and a 90% transmission grid can be floated at a potential V_4 to inhibit positrons from reaching the annihilation plate. Radiation shields fabricated from sintered W and Cu powders ("Heavy metal") are mounted on the cart to reduce the background from annihilations at the sample. The scintillators are arranged above and below the plate to observe the two annihilation γ-rays in coincidence. Two rather than three photons can be observed because the probability of the positron in the Ps atom to annihilate with an electron from the plate is much larger than for annihilation with the bound electron of the Ps. Bismuth germanate ($Bi_3Ge_4O_{12}$, titled BGO) was chosen as the scintillator material for its superior stopping power for $511keV$ γ-rays, which is about 2.5 times better than that for NaI.[74] The BGO scintillators are attached to R2238 photomultipliers supplied by Hamamatsu. These tubes employ an array of grids rather than a dynode chain to multiply the electron output signal of the photocathode. Such a photomultiplier is far less sensitive to magnetic fields than the more common version with arrays of plates. While other photomultipliers loose most of their gain in a longitudinal magnetic field of $80gauss$ the gain of these tubes changes only by a few percent. Long lightpipes are not required any more.

A quarter of the Ps formed in the ground state will be in the para Ps state and decay rapidly into 2 γ rays before much of it can leave the gas cell. Close to 20% of the positron beam will strike the grids at the entrance of the gas cell and

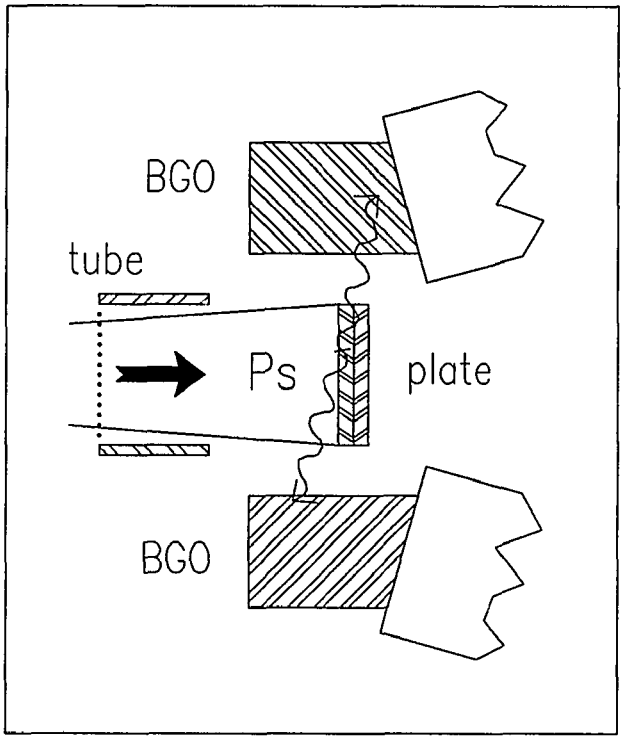

Figure 3.10 — Side view of the detection system. An annihilation plate is mounted on a cart inside the vacuum system. Positively charged particles are barred from reaching the plate by a positively charged grid in front of it. Above and below the plate BGO scintillators can monitor positron annihilation γ-rays in coincidence. Lead and tungsten shields on the cart and around the scintillators reduce the radiation background.

annihilate. These two sources of $511keV\gamma$ radiation will contribute considerably to the radiation background. Up to 4inches of lead shield the BGO detectors from these sources and also reduce the γ ray background from the nearby nuclear reactor. The "bulge" permits the use of the BGO detectors outside of the vacuum chamber, and access to them becomes very much easier without introducing great distances between them and the annihilation plate.

The cart that carries the annihilation plate is inserted into the chamber from below while the sample manipulator is mounted onto a port at the top of the chamber. The turbo pump is attached to a $12inches$ port at the side. This did

not restrict the angular range of possible reflection measurements because of the symmetry of the reflection process.

Although in principle the BGO detectors could be used to monitor the positron beam intensity, this is not done. They are mounted about $4cm$ from the center of annihilation plate and if the positron beam is permitted to reach this plate the detectors and the electronics would saturate completely due to very high counting rates. A new copper source will deliver on the order of $4 \times 10^6 e^+/sec$. An energy spectrum obtained with the BGO detectors at this time will be totally dominated by pile-up events. During a test the used multi channel analyzer indicated dead times in excess of 80% and the spectrum approached a flat line. Instead a (3×3)NaI detector was mounted off to the side from the annihilation plate (when it is located at the $\psi = 180°$ position) at a fixed distance of generally $36cm$. At this distance the much smaller solid angle reduces the rate of γ-rays to comfortable levels. The NaI scintillator is shielded from background radiation by additional lead bricks. To obtain the positron intensity the sample is removed from the beam line, the cart with the annihilation plate rotated to the $\psi = 180°$ position, and the gas cell is evacuated. The potentials V_3 and V_4 that normally inhibit positrons from entering the experimental chamber are grounded. The gas cell potential can now be used for a retarding field analysis of the longitudinal positron beam energy as explained in chapter 2.

The CEMA was not used as a detector but only as an annihilation plate because the pressure in the chamber exceeded $10^{-6} torr$. Electrical breakdown may occur and destroy the CEMA. In early versions of the experiment a Channeltron (CEM) was used in place of the Channelplate. It can be operated as an electron multiplier in much higher pressures than the CEMA. At that time triple coincidence measurements were considered to further improve the signal to noise ratio for the detection of Ps atoms. Unexpectedly large background rates rendered this scheme

useless. It was determined that the CEM was sensitive to gas atoms which left the gas cell almost as a jet. Also the channeltron seemed to be very inefficient in detecting low energy Ps atoms (below a threshold of about $7eV$). I speculate that the Ps atom has to break up in order to be detected by the channeltron. Similar observations were made by another group working with a Ps beam.[75]

The use of a plate has the advantage that it can be mounted a plane through the center of the two scintillators. If Ps is reflected from the flat sample surface that can also occur at the annihilation plate. The Channelplate was used to reduce this effect. About half of its surface is covered with tiny holes (the diameter is $2.5\mu m$). Thus the Ps can rattle around in the holes until is annihilates or breaks up. In the latter case an attractive potential of $-300V$ across the CEMA will accelerate the positron into a wall, where it can annihilate and be detected.

3.4. The Analysis of the Formation Data

In this section I will discuss the effect of a rather rapidly decaying source of positrons on the measurement. The observed signal also depends on the various efficiencies of the detectors. Their efficiency will be evaluated afterwards for the "singles" channel as well as for two scintillators in coincidence.

3.4.1. Effects of the decaying source — Because the positron source ^{64}Cu has a half-life of $12.7hours$, which is comparable to or less than the duration of most measurements of Ps formation or Ps reflection, the decay of the source has to be taken into account. For example 5.3% of the source activity decays within one hour. One parameter is varied during one measurement, while all others are held constant. Counts from various detectors are collected for a certain time (t_d the dwell time). In

a brief waiting period t_w the variable is changed, and then data for the next point are collected. A number of N points each including a dwell time and a waiting period make up one sweep. Optionally the waiting time between points can also contain a second data collection time of duration t_d. Then the beam will be turned off to obtain a measure of the background noise level. One measurement consists of M sweeps, which are all separated by a second waiting time, t_e. A counter capable of accumulating pulses in four registers was used. A program was written for a micro computer to control each experimental run and collect the data.

In a measurement of the Ps intensity for example the voltage on the gas cell is changed, and thereby the energy of the formed Ps. The windows of single channel analyzers, SCA, are set around the 511keV peak region of the two BGOs and the output counts are accumulated in two channels of a quad counter. The remaining two channels are register the coincidences between the BGOs and for the 511keV window output of a separate SCA connected to a NaI detector. Events from the two BGOs are considered coincidences when they fall within a $5 \times 10^{-8} sec$ time window. To obtain a "beam off" rate, the voltage on the grid before the gas cell is raised to prevent the positrons from entering the gas cell. Assuming that annihilations from positrons or para-Ps in the gas cell can be neglected, then the difference between "beam on" and "beam off" is a signal proportional to the Ps intensity at the detectors.

The dwell time is typically set to $100sec$, and the waiting time between points, including the "beam off" period of another $100sec$, is $110sec$. The power supply output stabilizes during the additional $10sec$ waiting period. Counts are accumulated for on the order of 30 points, depending on the positron intensity. 13 sweeps will last about 1 day. At the end of this measurement the source has decayed to 1/4 of its initial intensity.

Because any background radiation not related to the positron beam is assumed to be constant and the part that is related to the source has changed less than 0.2% in 100sec, the "beam off" data can be subtracted directly from the "beam on" data. The result is a signal that depends in time only on the positron intensity. Here a constant background radiation level is meant as constant during one sweep. If I further assume that the positron beam intensity is only a function of the decaying source, the conversion to a counting rate at a given time t_0 becomes simple. Other factors that can influence the positron intensity are for example fluctuations in the magnetic guiding fields or changes in the detector electronics. Since the power supplies that run the magnets are set in current control mode, and the electronics were permitted to warm up for a substantial time prior to any measurement, I will neglect such effects.

Several factors are involved in the elimination of the effect of a decaying source of positrons during a measurement. Once that is done and the signal has been normalized with the positron intensity at that time, Comparison with other measurements taken with different sources becomes straight forward.

First the source will decay in the time between the reference time t_0 for which the positron intensity is known, and the start of the measurement at t_s.

$$F_1 = exp\{\frac{t_s - t_0}{t_h} ln2\}. \tag{82}$$

From the beginning of one sweep to the start of the next the time Δt_s elapses. It consists of the dwell times (t_d) for each point and the various waiting periods (t_w between "on" and "off" points, and t_e between sweeps).

$$\Delta t_s = N(t_d + t_w) + t_e. \tag{83}$$

Until the start of the i-th sweep the source will decay to the fraction

$$exp\{-(i-1)\frac{\Delta t_s}{t_h} ln2\}. \tag{84}$$

The total counts accumulated at one point j in the run can be expressed in terms of the initial intensity during the first sweep R_j^0 as

$$R_j = R_j^0 \sum_{i=1}^{M} exp\{-(i-1)\frac{\Delta t_s}{t_h} ln2\} \tag{85}$$
$$= \frac{q^M - 1}{q-1} R_j^0, \qquad q^i = exp\{-(i-1)\frac{\Delta t_s}{t_h} ln2\}$$

The inverse of this sum of a geometric series relates the total accumulated counts at point j to an average number of counts of one sweep at the start of the measurement.

$$F_2 = \frac{q-1}{q^M - 1}. \tag{86}$$

The inverse of the factor that converts the number of counts accumulated in one dwell time into a rate at the beginning of that period is

$$F_3^{-1} = \frac{t_h}{ln2}(1 - exp\{-\frac{t_d}{t_h} ln2\}) \tag{87}$$

A factor of t_d cancels out when the number of accumulated counts in the dwell time are converted into a rate per time unit. A final factor will shift the rate at each point of the first sweep to the start of the run. This factor is the only one that is different for each point in a sweep. The difference between points is only minute, but becomes considerable during the course of some long sweeps. For the point j it is

$$^jF_4 = exp\{(j-1)\frac{t_d + t_w}{t_h} ln2\}. \tag{88}$$

To obtain a rate at the reference time t_0 each point needs to be multiplied with the product of these factors. Since the initial positron intensities for the various sources are not necessarily the same the data need to be normalized by the individual intensity for comparison. The positron intensity can be obtained with the same detection system. The gas cell is evacuated and the potentials V_3 and V_4 are grounded allow the initial positron beam strike the annihilation plate. Now the positron intensity as a function of the gas cell potential can be measured.

The efficiency of the moderator can change during the course of the experiment. That would effectively alter the decay time of the source. This was checked occasionally. Half-lifes within 10% of the literature value were measured.

3.4.2. Efficiency of a scintillation detector — Once a positron or Ps atom strikes a solid surface it rapidly annihilates with an electron provided from that surface. Applied electric potentials prevent it from "bouncing" off the surface. The center of mass motion of the positron electron pair is small compared to the speed of light and the two annihilation γ-rays will come off in opposite direction. Either one can be detected by the scintillator. The probability to detect a positron is

$$p = 2\Omega s\epsilon \tag{89}$$

where Ω is the solid angle covered by the scintillator, s is the fraction of γ-rays that do not get attenuated by air or any other objects like the chamber walls between the source of the radiation and the detector, and ϵ is the efficiency of the detection system. Included in ϵ are the intrinsic efficiency in the photopeak of the scintillator and the energy window in which pulses are considered. The factor of 2 comes about because 2 undistinguishable photons are generated with each annihilation of a positron. If the distance R from the radiation source is large compared to the detector dimensions, the solid angle will become proportional to R^{-2}.

$$\Omega = \frac{A}{4\pi R^2} \tag{90}$$

Here A is the area of the detector facing the source.

At closer distances the situation becomes a little more tedious to calculate. One needs to consider the solid angle subtended by the detector and also some edge

effects. For a circular cross section of the detector with a diameter D and a small point source the geometric part is given by

$$\Omega = \frac{1}{2}(1 - \cos\theta), \quad \text{and} \quad \tan\theta = D/2R. \tag{91}$$

The edge effects come about because the scintillator itself is slightly less efficient in detecting a γ-ray that strikes it near the edges. Less material is available to interact with the photon. To avoid this one can collimate the solid angle with lead shields to utilize only those photons that hit the central part of the scintillator.

With the use of a calibrated check source the overall efficiency of a detection system E can be measured directly. It becomes unnecessary to measure all the separate factors. In this case I used a source of ^{22}Na. Two things need consideration. First of all not all of the decays involve the emission of a positron. The branching ratio for ^{22}Na is $b = 0.9$. This factor needs to be included into the determination of the efficiency. Second the isotope also emits a high energy γ-ray, which will cause a Compton background on top of the source unrelated background. This contribution can be estimated from the Compton background level just above the $511keV$ spectrum of positron annihilation photon if only the peak events are considered in the efficiency determination. If the total $511keV$ spectrum is used it is more advantageous to use another γ-ray standard with a similar energy like ^{137}Cs, for example.

Only the photo peak rate of a (3×3)NaI detector was used for the determination of the positron intensity. The detector was located at $36cm$ distance from the annihilation plate. At this distance the R^{-2} approximation of the solid angle is valid and the source can be considered pointlike. Then the number of counts accumulated in a time interval Δt in a small window of $\approx 56keV$ around the $511keV$ peak can be expressed as

$$\frac{1}{\Delta t}N = \Omega(2bs_1\epsilon_1 + s_h\epsilon_h)R_0. \tag{92}$$

s_1 and ϵ_1 are the attenuation and efficiency factors for the $511keV$ and, with the subscript $_h$, for the $1.27MeV$ photons of the ^{22}Na source respectively. R_0 is the decay rate of the source. Such a spectrum is shown in figure 3.11. Further I can approximate the ratio of the contribution of Compton events of the high energy photons to the rate in the narrow $511keV$, defined as r by the Compton rate in an equal size window just beyond the $511keV$ peak on the high energy side N_h^*

$$r = \frac{s_h \epsilon_h}{1.8 s_1 \epsilon_1 + s_h \epsilon_h} \approx \frac{N_h^*}{N + N_h^*}, \tag{93}$$

where N_i is the number of counts from each individual contribution.

$$\begin{aligned} N_1 &= \Omega s_1 \epsilon_1 b R_0 \Delta t, \quad \text{and} \\ N_h &= \Omega s_h \epsilon_h R_0 \Delta t \approx N_h^*. \end{aligned} \tag{94}$$

Now the overall efficiency $E_1 = \Omega s_1 \epsilon_1$ in the $511keV$ peak can be determined from the known rate R_0

$$\frac{N}{\Delta t} = 0.9 \frac{1}{1 - r} R_0 E_1. \tag{95}$$

3.4.3. Efficiency of a coincidence system — If the annihilation γ-rays are measured in coincidence there is no need, in principal, to measure the efficiency of the system with a check source, if the solid angle Ω is known. In reality this is complicated somewhat because usually a coincidence system is used to improve the signal to noise ratio. In order to obtain the efficiency of the system on the other hand an exact knowledge of the radiation background independent of the source of coincident γ rays is necessary. This can be controlled much better with a check

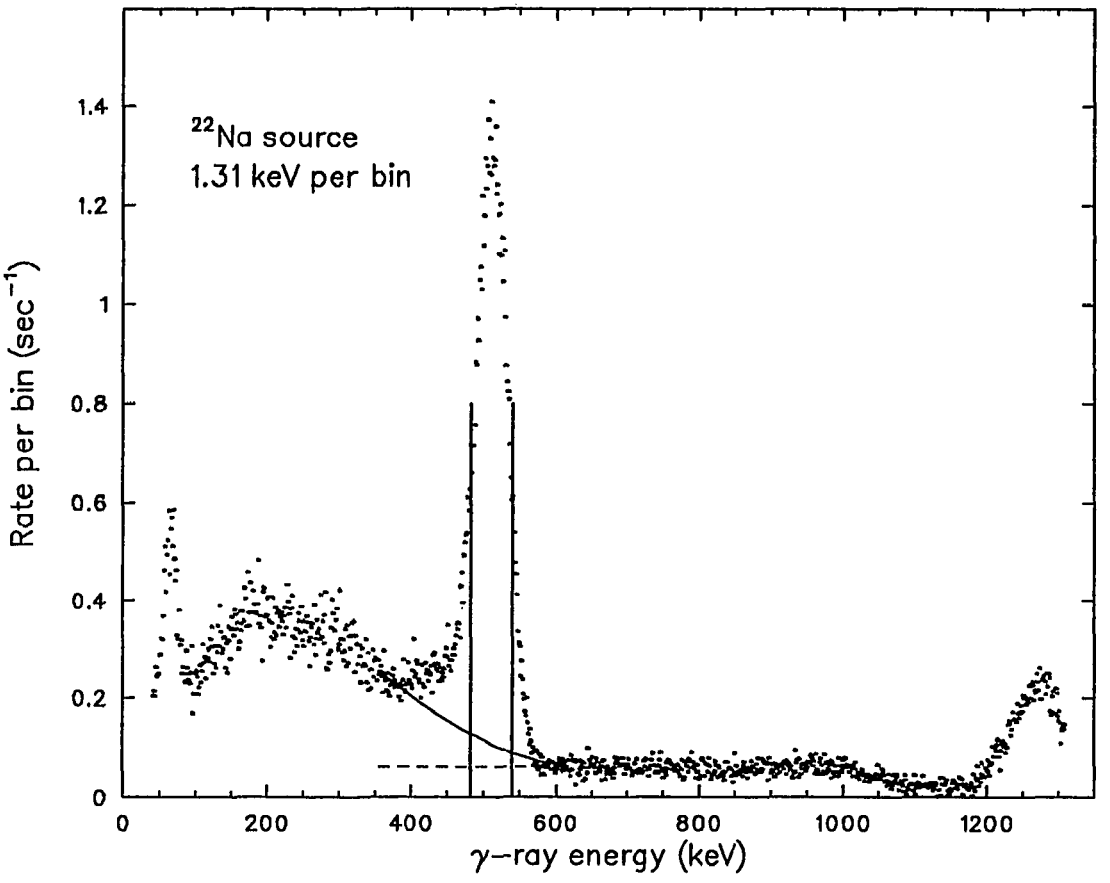

Figure 3.11 — γ-ray spectrum of a ^{22}Na source measured with a NaI scintillator at about 14″ distance. Shown are the counts per second per energy window versus the energy. The solid vertical bars represent the energy window that was used for the peak efficiency calculations. the dashed line is a continuation of the Compton background due to the high energy photon, and the solid line represents a fit of the spectrum without the $511keV$ peak with a second order polynomial.

source than during the true experimental conditions. Analog to the equations for a single detector the individual counting rates are for the detectors 1 and 2 and their coincidence rate

$$\begin{aligned} \frac{N_1}{\Delta t} &= 2\Omega s \epsilon_1 R_0 \\ \frac{N_2}{\Delta t} &= 2\Omega s \epsilon_2 R_0 \\ \frac{N_c}{\Delta t} &= 2f\Omega s^2 \epsilon_1 \epsilon_2 R_0 \end{aligned} \tag{96}$$

where I assume that the geometries and attenuation factors are the same for both detectors. Only their efficiencies and the effect of the electronics are different. Because neither the detectors nor the electronics have perfect timing characteristics, the interval between the two coincidence events will not always be the same. If one displays them on a time scale like in figure 3.12 they display an almost gaussian distribution on top of a constant background of random coincidences. Most coincidence units permit the user to set a time window of 2τ into which pulses from either detector have to fall to be considered a coincidence event and be counted. The factor f represents the fraction of counts in this window to the total coincidence peak counts. When the coincidence circuit receives a pulse from a detector, it converts this pulse into a new one with the width τ. In order to be considered a coincidence the two pulses of now equal width have to overlap at least in part. One of them can be delayed in time over a range of 2τ and still have a fraction in common with the other pulse. Thus the time widow of 2τ above.

Returning to the three count rates I can evaluate the various ratios to determine the efficiencies of the detectors $s\epsilon_i$ and either the rate of coincidences R_0 or the solid angle Ω

$$\frac{N_c}{N_1} = fs\epsilon_2, \quad \frac{N_c}{N_2} = fs\epsilon_1, \tag{97}$$

and

$$\frac{N_1 N_2}{N_c} = \frac{2\Omega}{f} R_0 \Delta t \tag{98}$$

provided f can be measured or is equal to 1 because the full coincidence peak is counted.

Just like the singles events the coincidence rate will contain some fraction of noise. Three contributions play a more or less important role. One is purely random. There is a finite probability that one detector observes a γ-ray from one annihilation while the other detector receives a photon from a second annihilation

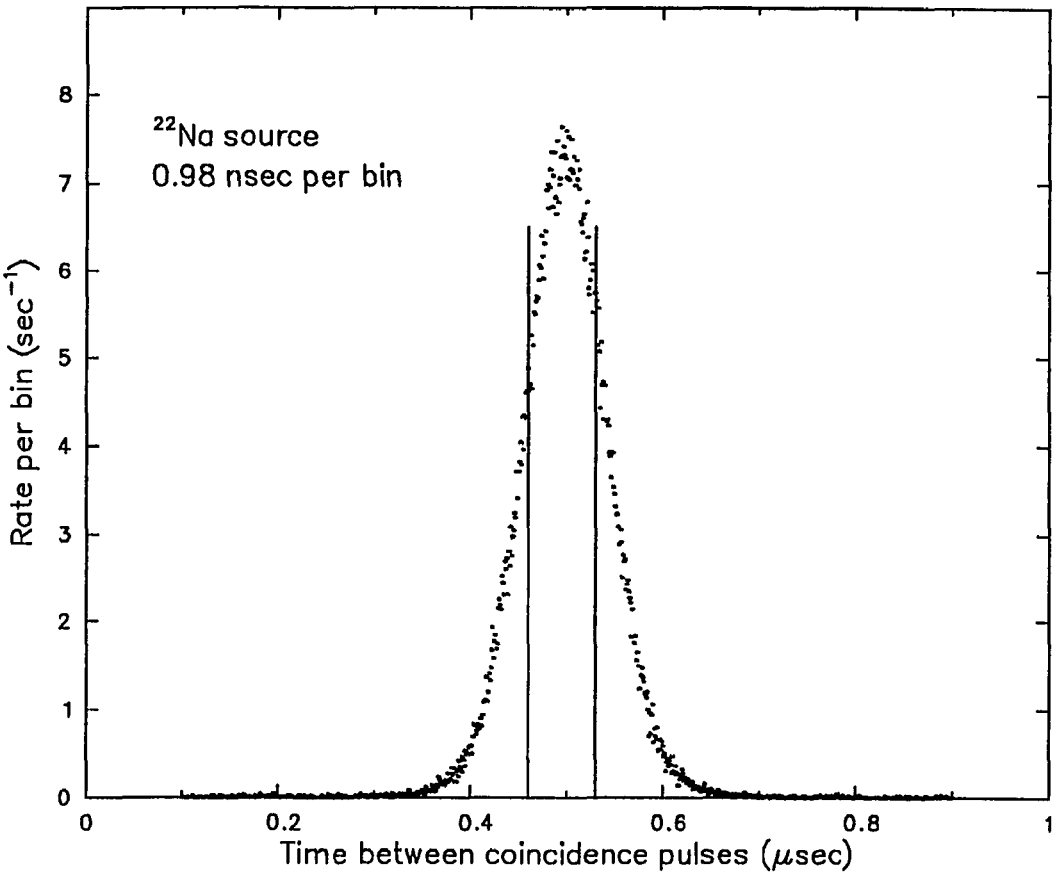

Figure 3.12 — Plot of the coincidence rate per time bin of the MCA as a function of the time delay between the pulses from the two BGO detectors as they monitor positron annihilations in a ^{22}Na source. The vertical bars indicate the 2τ time window set by for the coincidence unit (see text).

that occurs within the 2τ period of the coincidence window. This can be estimated by

$$\frac{N_c^{random}}{\Delta t} = 2\tau \frac{N_1}{\Delta t}\frac{N_2}{\Delta t}. \tag{99}$$

A second source of coincidence background occurs when a third γ-ray is emitted almost simultaneously with the positron in the β decay. This is the case for the ^{22}Na source. The $1.27MeV$ photon is emitted when the decay product nucleus of ^{22}Ne relaxes into the ground state. The $3psec$ lifetime of this state cannot be resolved with my system. An appropriate Compton event of the high energy photon in one detector can be registered as a $511keV$ annihilation event in coincidence with

the photon from a "true" event. The contribution to the total coincidence rate can be estimated to be the product of the probabilities to observe these events in coincidence.

$$\frac{N_c^{mix}}{\Delta t} = (2b\Omega s\epsilon_1)(\Omega s_h \epsilon_h)R_0, \tag{100}$$

where $s_h\epsilon_h$ relate to the observation of the high energy γ-ray in the right energy window. Since the high energy photon is emitted isotropically this contribution is independent of the alignment of the detectors. Thus by turning one detector out of the coincidence region this can be measured.

If the detectors are placed close together it becomes likely that photons scatter between them. This is a third cause for distortions of the coincidence system. High energy cosmic ray showers can trigger a $511keV$ signal in both BGO detectors and thus cause a coincidence event. On average this effect should cancel out if background measurements are taken. It is difficult to shield the scintillators against this source of noise if it is due to cosmic rays. They are too energetic to be attenuated appreciably by lead. $511keV$ annihilation photons on the other hand can Compton scatter in one detector each and then one of the photons could be registered in the other detector. The two events in one detector may pile up in the following amplification and then be registered in the $511keV$ energy window. This would artificially increase the peak count rate in either detector and distort the result of a simple calculation of the efficiencies based on the three counting rates. Thus the random coincidence rate is an underestimate.

In figure 3.13 a typical spectrum of one of the BGO scintillators is shown. Two vertical bars represent the selected energy window that is used for the coincidence unit. It does not cover the total photo peak because in the "wings" the ratio of signal to background becomes much smaller.

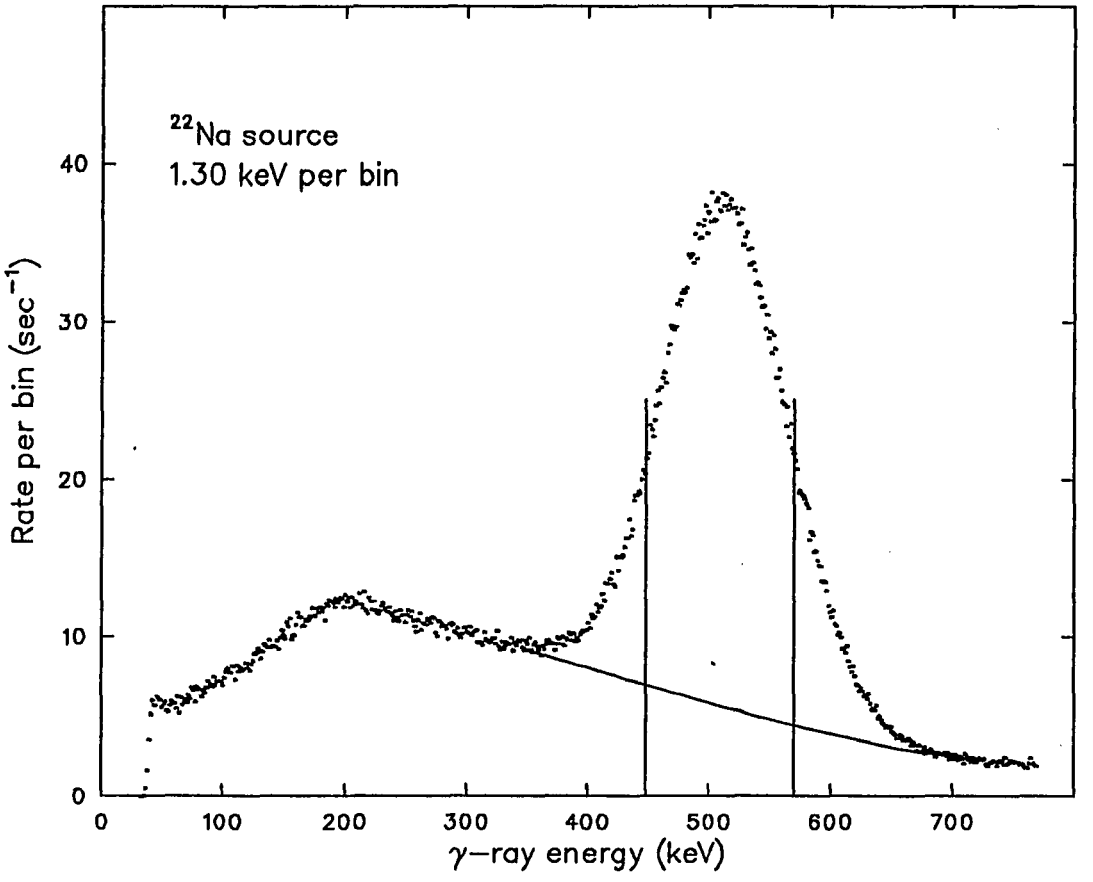

Figure 3.13 — Energy spectrum of a ^{22}Na source seen by a BGO detector. The counting rate per energy window per second is plotted versus the energy. The vertical bars indicate the selected energy window around the photo peak. The background without the source has been subtracted. Note the much broader photopeak ($\approx 120keV$ FWHM) compared to the (3 × 3)NaI detector. The solid line represents the estimate of the background under the photopeak.

Using these spectra I can evaluate the solid angle and the efficiencies. The number of accumulated counts for the two BGO detectors and also the NaI detector are listed in table 3.3 below together with the calculated efficiencies.

In order to avoid the various background contributions to the coincidence measurements I use only the counts in a narrow window around the $511keV$ peak. I match the background counts on either side of the peak to obtain an estimate of the background under the peak itself. With the use of a cubic spline fitting routine this can easily be done.[76,77] A qubic spline is fitted to the count rates on either side of the peak and extended through the peak region (see the solid line in figure 3.13).

Table 3.3: Efficiency of the detectors

Parameter	Detector			
	NaI	BGO I	BGO II	Coinc.
FWHM of the				
$511keV$ photopeak (keV)	49.5	123.0	121.5	
coinc. window (nsec)				103
SCA window width				
photopeak (keV)	56.3	121.4	117.3	
coincidence (nsec)				50
Counts in 100sec	4354.2	295257	279572	46987
Background in 100sec*)	242.8	53485	53275	135
Fraction r	0.944	0.819	0.809	0.997
Factor f				0.586
Solid angle Ω 10^{-3}	2.87	0.107	0.107	0.107
Efficiency in %†)	0.141	7.8	7.3	1.56
Conversion factor	707.7	12.8	13.7	64.27

*) This is an estimate that includes Compton events from $1.27MeV$ γ-rays.

†) The intensity of the used source was $2.932 \times 10^4 e^+/sec.$

For the calibration of the three detectors and the coincidences (coinc.) a small (0.878μCi) ^{22}Na source was mounted on the annihilation plate. The BGO detectors were mounted above and below the bulge and the (3×3)NaI detector at $14inches$ from the plate, just as during positron beam measurements. The magnets were turned on, to resemble the actual experimental conditions as close as possible. The natural background was subtracted only in the case of the NaI detector.

I determine the ratio r_i of the background corrected rate (count rate above the line) in the window to the total rate in the window. This is repeated for each detector and the coincidence output and the values are included into the evaluation of the solid angle.

$$\Omega = \frac{1}{2} f \frac{N_1 N_2}{N_c} \frac{r_1 r_2}{r_c} R_0 \Delta t \tag{101}$$

Once Ω is known I can evaluate the overall efficiency of the coincidence channel and need not worry about the singles channels any more. All the values which are relevant for these calculations are listed in the table.

3.4.4. Ps decay in flight — As I discussed earlier Ps is not a stable atom but will decay depending on which state it is in. The half-life of para Ps is so short that essentially all will decay already within the gas cell. As for the ortho Ps, which amounts to 3/4 of the Ps formed in the ground state a certain fraction will decay before it can reach the detector located at about $31cm$ from the gas cell exit. The fraction that survives F_s the distance depends on the time it takes to reach the detectors, which is proportional to the square root of the energy of the Ps atom. Thus

$$F_s = exp\{-\frac{l}{{}_3\tau v}\} \quad \text{, and} \quad v = \sqrt{\frac{E_{Ps}}{m_e}} \tag{102}$$

where l is the distance to the detectors, v the velocity of the Ps atom, E_{Ps} its energy and $m_e = \frac{1}{2} m_{Ps}$ the electron rest mass. Shown in figure 3.14 is this surviving fraction F_s as a function of the Ps energy. A distance of $l = 0.4m$ was chosen. The fraction of 3/4 for the ortho Ps fraction was included.

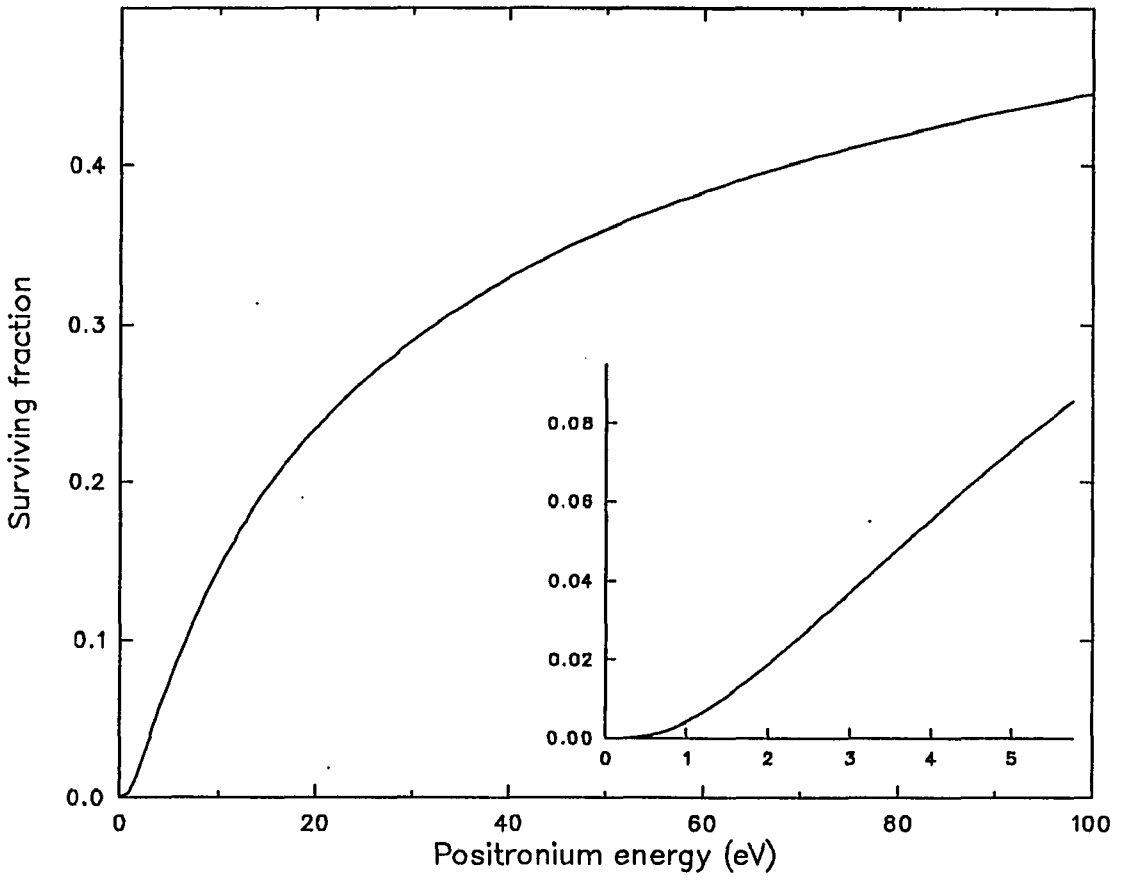

Figure 3.14 — Fraction of Ps that does not decay in flight from the gas cell to the detectors (about $31cm$) as a function of the Ps energy. Only 3/4 of the Ps formed in the ground state is formed in the longer lived ortho state. This fraction is included in the values. The insert illustrates the low energy behavior.

3.5. Positronium Beam Results

To measure the efficiency of the gas cell the annihilation plate and the detectors are rotated to the $\psi = \theta_i + \theta_r = 180°$ position. No sample is in the beam line. The gas cell is filled with $10^{-3} torr$ of Ar. Positrons with a total energy of $150eV$ enter the gas cell and are prevented from proceeding into the experimental chamber by a potential of $200V$ on the tube V_3. The number of detected Ps atoms reaching the annihilation plate are then measured as a function of the potential on the gas cell and thus indirectly as a function of the Ps energy. To obtain the radiation background the positron beam is turned off periodically at the entrance of the gas

cell by floating V_1 to $200V$. The results for a typical run are shown in figure 3.15 for the singles counts of one of the BGO detectors and in figure 3.16 for the coincidence channel between the two BGO detectors.

In spite of considerable shielding of the scintillators the background signal for the singles rate is about as large as that from Ps atoms annihilating on the annihilation plate. This is very much improved in the case of the coincidence channel. Above $150V - 8.9V = 141.1V$ the positrons do not carry enough kinetic energy to form Ps. A small signal above the background can be observed in the singles channels which is due to annihilations occurring in the gas cell. This contribution is too small to play a significant role in the coincidence channel which I will use in the further analysis. Included in the background is a small signal due do high energy positrons. The $\vec{E} \times \vec{B}$ filter does not completely separate the moderated positrons from the fast positrons. The remaining fast positrons will pass both potential barriers before and after the gas cell and are registered in the "beam on" and the "beam off" mode.

The background signal is subtracted from the total. Following the data are corrected for the effects of the decaying source to a reference time when the intensity of the positron beam is known. The rate of detected Ps atoms in the coincidence channel per initial positron intensity is obtained by taking the ratio. This function still includes the efficiency of the detection system. The apparatus was designed in such a way that this efficiency did not change when the detectors were rotated around the center of the experimental chamber. Thus the knowledge of the absolute efficiency of the gas cell is not required for the measurement of a reflection coefficient of a sample located in the center of the chamber. The efficiency will drop out when the ratio of initial Ps intensity and reflected intensity is calculated. The detected intensity per initial positron rate is shown in figure 3.15 as a function of the inferred Ps energy.

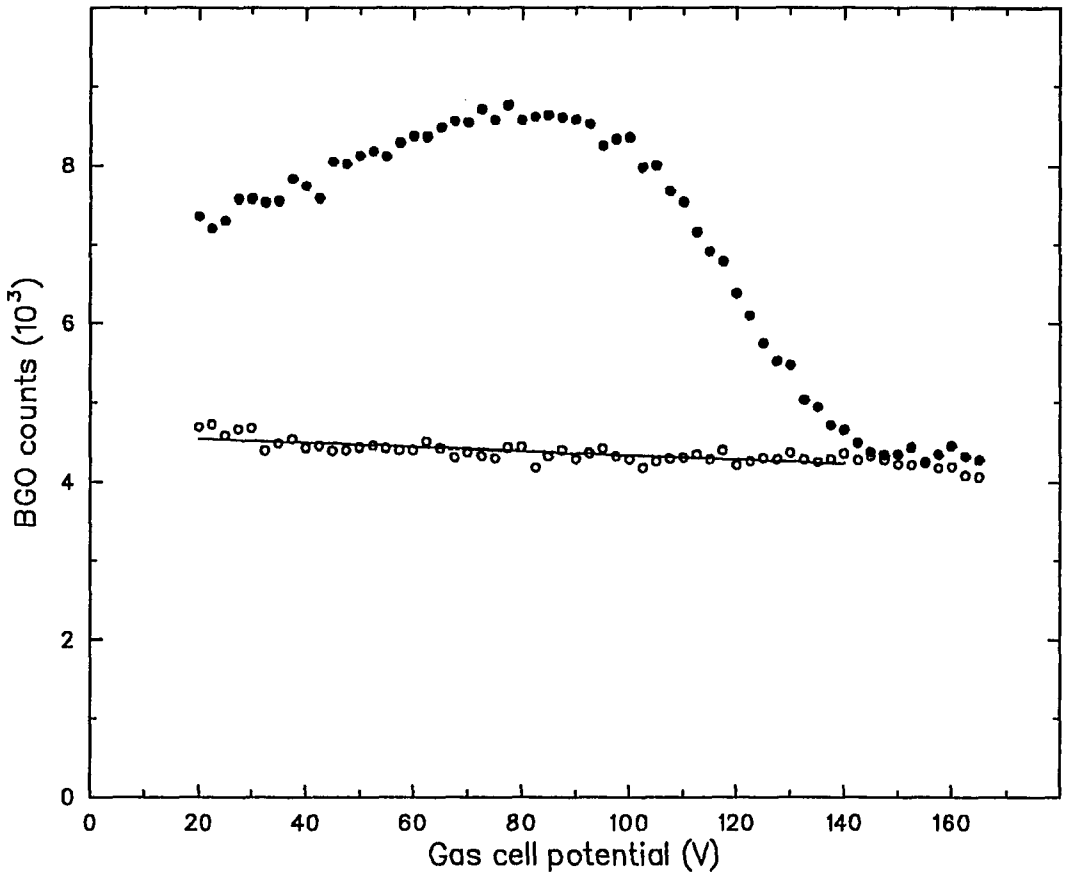

Figure 3.15 — Counts detected by one of the BGO detectors during the course of one Ps formation measurement as a function of the potential on the gas cell. The total positron energy was $150eV$ and the gas cell was filled with $10^{-3}torr$ Ar. The full circles are the results when positrons enter the gas cell. In the case of the open circles the positron beam was repelled at the grid V_1. The solid line represents a fit of a straight line to the "beam off" data.

To improve on the statistical error a series of measurements were made emphasizing the region of low Ps energies below $10eV$. Here the effect of Ps decay in flight is much more severe than at higher energies. The obtained data were binned in 1eV bins and weighted by their statistical error values. The result is shown in figure 3.18. The insert shows the efficiency for the energy range up to 10eV on an expanded scale.

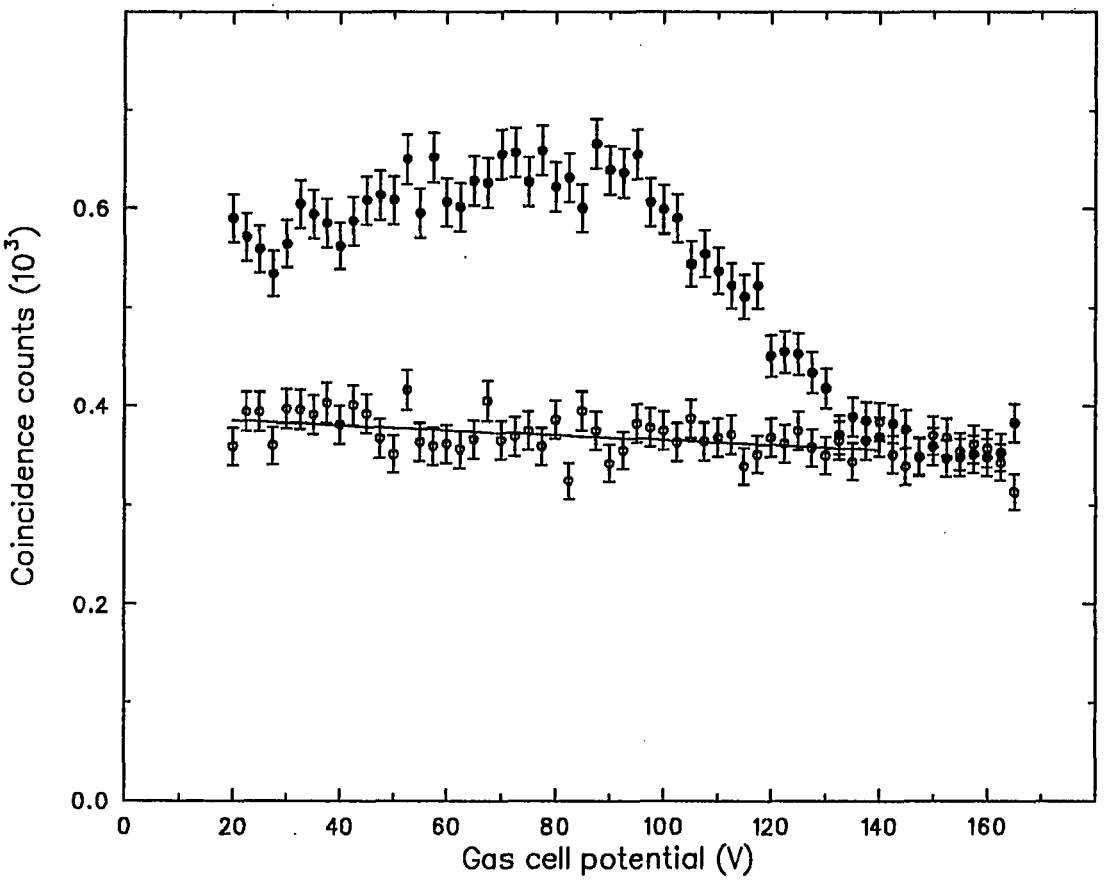

Figure 3.16 — Coincidence counts for the same measurement as in the previous figure. Again the full circles represent the data with positrons in the cell and the open circles the background data. The error bars are statistical.

The solid line in the figure was obtained by the following procedure. The detected Ps intensity is corrected for the decay in flight from the gas cell by dividing the data values by the fraction of Ps surviving the flight. This normalization function approaches zero with $E_{Ps} \rightarrow 0$. At small energies ($E_{Ps} < 5eV$) the statistical error becomes very large, and the result will diverge. On the other hand the Ps formation cross section has to approach zero near the threshold of formation. Assuming a linear dependence at low enough Ps energies this divergency can be eliminated. A polynomial that has to cross zero at $0eV$ Ps energy is fitted to the data. The fit is then multiplied with the fraction of Ps surviving the decay in flight to and plotted as a solid line in the figure.

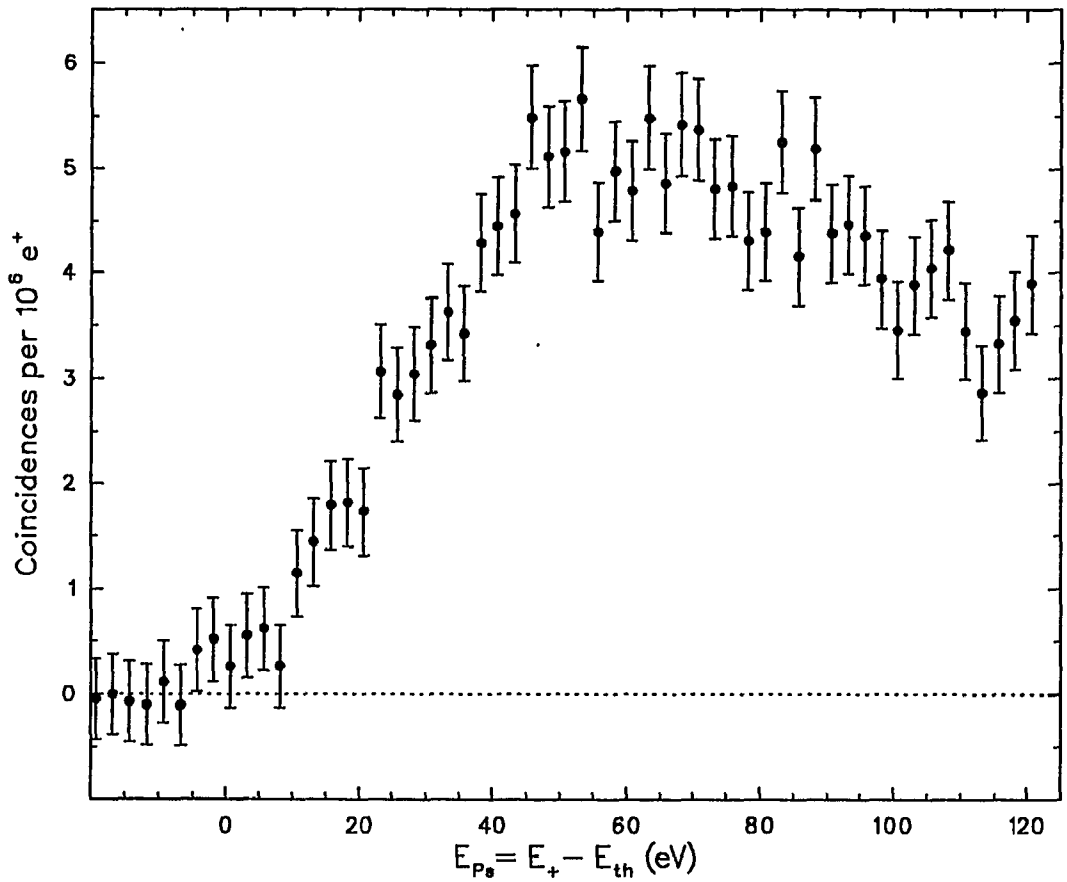

Figure 3.17 — Rate of Ps atoms detected in coincidence per positron intensity entering the gas cell as a function of the Ps energy. Here the results of the raw data shown in the previous figure are used. The error bars are a combination of the statistical error values from the "beam on" and the "beam off" data. In case of the "beam off" data the fitted line is used.

I did not fit the data with the cross section for Ps formation because a number of relevant factors have not been measured or calculated. No differential Ps formation cross sections have been calculated for Ar, and they have not been measured either. In addition the formed Ps atoms can scatter from the Ar atoms and either break up or scatter out of the solid angle subtended by the detectors. only now are such Ps atom cross sections being measured[73] In addition most of the positrons will not move parallel to the beam axis but rather spiral around axes parallel the the beam axis. At any time their momentum vector will have a radial component. This radial component will tend to broaden the effective differential

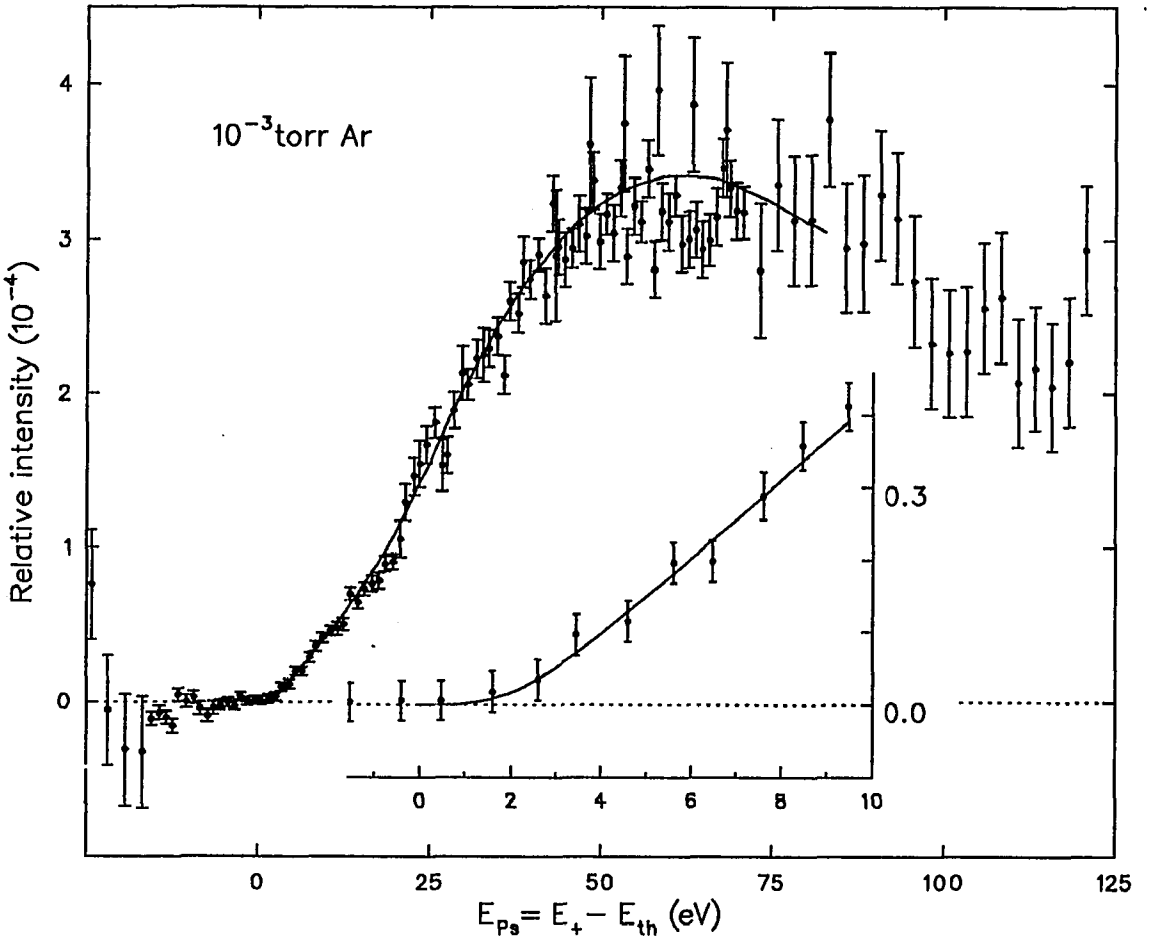

Figure 3.18 — The relative intensity of the Ps beam at the annihilation plate. Shown is the Ps intensity per positrons versus the Ps energy. This reflects the efficiency of the gas cell to form ortho Ps in a 2.5° cone and the decay in flight of the initial Ps beam. The cell was filled with 10^{-3}torr Ar. Here several measurements have been added to obtain improved statistics. The solid line represents a fit (see text). Above an energy of $70eV$ only one measurement with poor statistics was available. Hence the larger error bars than at lower energies were the average of several measurements is shown.

cross section. This becomes even more severe in the less probable but possible case of double collisions where the first one is an elastic collision.

I will use the fitted result of the Ps formation measurements in the final calculation of the reflection coefficient. In that case the detector efficiency and the effect of one 90% transmission grid after the gas cell (a factor of $64.27/0.9 = 71.14$ according to table 2.3) will not be included.

4. Reflection of Ps

To my knowledge no theoretical predictions exist on the topic of Ps reflection or Ps diffraction from surfaces for energies above $1eV$. For lower energies an estimate was made by Pendry for copper.[15] As was pointed out in the introduction, positron beams of high intensities are required to perform reasonable measurements. However a number of considerations can be made to enhance the chances for a successful measurement. The Ps atom is only weakly bound with half a Rydberg ($E_b = 6.8eV$ for the ground state). Atoms with a larger kinetic energy may break up upon collision with the surface of a solid. This will be even more likely with increasing energy. Interactions with phonons would alter the Ps energy only by small amounts. Electronic interactions like the excitation of an electron into the conduction band will be inelastic. Also the positron of the Ps atom may annihilate with an electron from the surface. A sample crystal with large lattice parameters should display diffraction peaks at energies near or below the band gap energy to enhance the reflected intensity. Ward and collaborators[78] performed simple calculations of s-wave cross sections for elastic scattering of free electrons from Ps. They found values for energies below $10eV$ of on the order of $228\pi a_0^2 \approx 10^{-14}cm^2$. Typical densities for conduction electrons in metals range around $10^{22}cm^{-3}$. This results in a mean free path of on the order of 1Å. The majority of the Ps atoms that penetrate deeper into the solid will loose some energy due to the recoil from Ps electron scattering and be lost for elastic reflection measurements.

Ionic crystals, where all the electrons are bound and which feature large lattice constants seem to be good candidates. Further to simplify the experimental requirements a first sample should have a simple structure and remain clean over extended periods of time. Stern,[79] LiF is a good candidate. Besides the Ps atoms the sample surface will be "bombarded" with large amounts of atoms from the gas cell. In the case of noble gasses that is not too serious, but the gas will contain some impurities which may stick to the surface and alter the results. For example I used Ar of 99.995% nominal purity. If the gas cell is filled with $10^{-3}torr$, the background pressure in the experimental chamber is near $10^{-5}torr$ and somewhat larger at at the sample. The partial pressure of contaminations on the sample may be in the $10^{-9}torr$ range, which is no longer UHV. Just like for the first experiments on He atom diffraction by

In the following I will consider a number of additional systematics involved in the reflection measurements. In the second part I shall present the obtained data and discuss them. It will be followed by an attempt to explain the results in term of a simple theory of plane waves reflecting from a potential step.

4.1. Experimental Considerations

The experimental apparatus designed to be used for the measurement of the Ps beam intensity as well as for the reflected beam strength is shown in figure 4.1. The detectors shown already in figure 3.9 can be rotated around the center of the chamber. At that location the sample, which is mounted on a heating stage on a rotary linear feedthrough, can be inserted into the Ps beam line. The normal of the sample surface and the beam axis form the incident angle θ_i and the angle from the sample normal to the direction towards the center of the detector system is called θ_r. I will refer to the total reflected angle as ψ. ψ can be changed from somewhat less than 100° to 180°, while any angle is possible for θ_i. As mentioned before the

used photomultiplier tubes are designed to be almost unaffected by magnetic fields on the order of $80 gauss$. Thus as long as the configuration between the annihilation plate and the two BGO scintillators does not change the detection efficiency for this system will remain constant for all angles ψ. Such a design eliminates the need to determine the absolute efficiency of the detectors for the measurement of reflection fractions. For the reflection coefficient it suffices to obtain the ratio of the intensity scattered into the direction ψ and the intensity of the undisturbed, primary beam with $\psi = 180°$ and the sample removed.

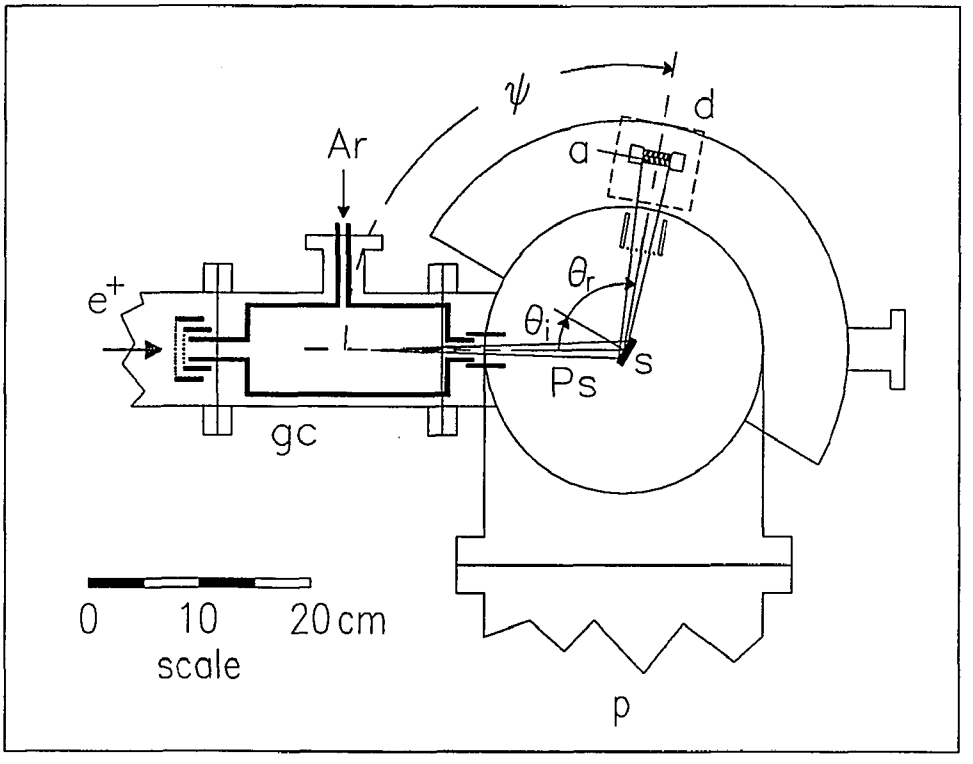

Figure 4.1 — Top view of the experimental chamber as in figure 3.9 but in the configuration for Ps reflection measurements. Again variable Ps energies can be achieved by biassing the gas cell (gc). The tubes and grids (t) on either side can be charged to positive potentials to control the flux of positrons (before the gas cell) and to prevent the positrons from entering the experimental region. A third tube at the detector has the same function for the cases when the annihilation plate intercepts the primary beam. The sample angle is θ_i to the beam axis and θ_r to the direction of the detector. Not shown is considerable lead and tungsten shielding around the detectors (See text for more).

One way to measure the specular reflection of Ps would be to turn the sample in steps $\Delta\theta$ and simultaneously the detectors by twice the amount to maintain the specular condition $\psi = 2\theta_i$. This was not done because of the large amounts of lead and tungsten shielding around the scintillators. To improve the efficiency for coincidence detection of 2γ annihilations of Ps atoms at the plate the BGO crystals were placed close together (only $3inches$ apart). Inter-detector scattering of more energetic radiation can become a severe problem for such a configuration. This is even more so the case because BGO scintillator feature a rather broad photopeak region. To prevent this I had to shield each scintillator against radiation from sources other than the annihilation plate as much as possible. Up to $4inches$ of lead was piled around the detectors on the outside of the experimental chamber, while a $2inches$ thick lead block shielded against annihilation radiation of para-Ps in the gas cell. Blocks of dense tungsten alloy reduce the background of annihilation radiation produced at the sample.

In addition to these passive measures the γ-ray background can be determined experimentally and subtracted from the total signal. Two possibilities exist. The first one has already been used for the Ps beam intensity measurements. the grid potential V_1 is elevated high enough to prevent positrons from entering the gas cell and thus from forming Ps. The remaining counts registered by the detection system stem from the radiation background that is independent from the positron beam. Such sources are: the natural background; cosmic rays; the nearby nuclear reactor; and any Ps that may be formed in the residual gas before the gas cell. The background radiation without the fraction due to the positron beam is largest at an energy of $150keV$. At higher energies it drops off like an exponential. These Ps atoms are not desired since they usually carry more kinetic energy. Another contribution stems from "fast" unmoderated positrons coming from the source. The $\vec{E} \times \vec{B}$ filter does not eliminate all of these energetic positrons. The cross section to

form Ps in a gas becomes negligible at energies above several hundred eV but these positrons can form Ps at the sample which can reach the detectors. Evidence for this effect was found when comparing "beam off" background rates with a distant beam line valve open and closed.

Any background radiation resulting from positron and Ps annihilations in and after the gas cell cannot be eliminated by this method. For this the second method becomes more effective. I can rotate the sample away from the detectors in the opposite direction by the same amount θ_i. Now any reflected Ps intensity will move away from the annihilation plate. On the other hand the above mentioned source of background will remain almost constant. Annihilations at at the sample will be somewhat attenuated and Ps decays in flight from the sample to the detectors will no longer be present. However this method will not distinguish the effect of "fast" positrons from the signal due to Ps reflection. Both will be turned on and off when the sample is rotated.

The use of a ^{64}Cu source of positrons with a relatively short half-life on the other hand makes the use of both background measurement methods undesirable because 3/4 of the measurement would be devoted to background measurements. The Ps rate from high energy positrons should be independent of the sample angle and rather small. Once that has been verified I consider the second method of two sample angles to be sufficient.

One last effect needs to be considered when measuring the reflected fraction. As the sample is turned to larger angles $\theta_i \rightarrow 90°$ it will intercept less and less of the initial Ps beam. The sample used in this work was $2s = 7/8inch$ wide and $1inch$ high. The cone of the ps beam that is intercepted by the $1inch$ diameter annihilation plate has the radius R_B at the sample. The cone of the Ps beam intercepted by the annihilation plate measures $\approx 5°$ across. Up to a certain threshold angle of θ_i the value $x = s\cos\theta_i$ will remain larger than the radius R_B. Given the accuracy of the

differential Ps formation cross section I assume a homogeneous intensity distribution in this cone. Then simple geometric considerations lead to the following fraction f (as illustrated in figure 4.2)

$$f = \frac{2}{\pi}\Big(\sin\beta\cos\beta + \beta\Big); \quad \sin\beta = \frac{x}{R_B}. \tag{103}$$

The Ps beam intensity needs to be corrected by this fraction to accurately calculate the reflection coefficient. Figure 4.3 shows the fraction of the Ps beam intercepted by a sample of 7/8 width by $1inch$ height as a function of the sample angle.

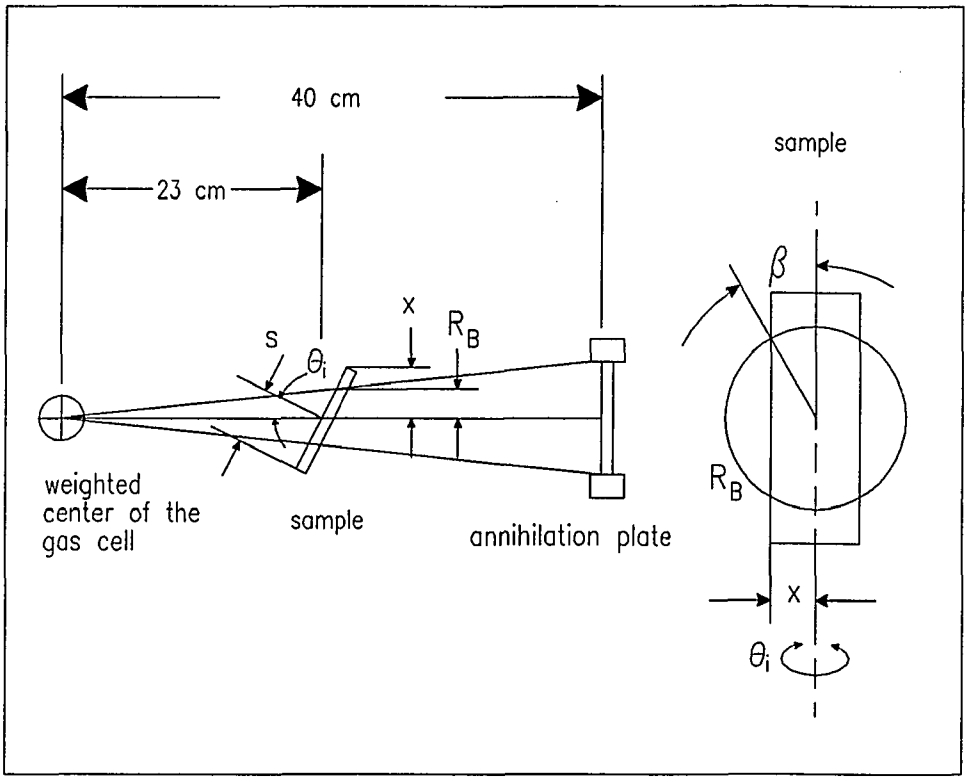

Figure 4.2 — Illustration for the calculations to evaluate the fraction of the Ps beam intercepted by the sample as a function of the sample angle θ_i. The left part shows the arrangement from above and the right section of the figure shows the sample as seen by the approaching Ps atoms. The cone of the Ps beam is given by the dimensions of the annihilation plate at $40cm$ from the center of the gas cell and has the radius R_B at the sample. Beyond a certain threshold angle the sample will no longer intercept all of the beam. The angle β is used in equation (103) to evaluate this fraction.

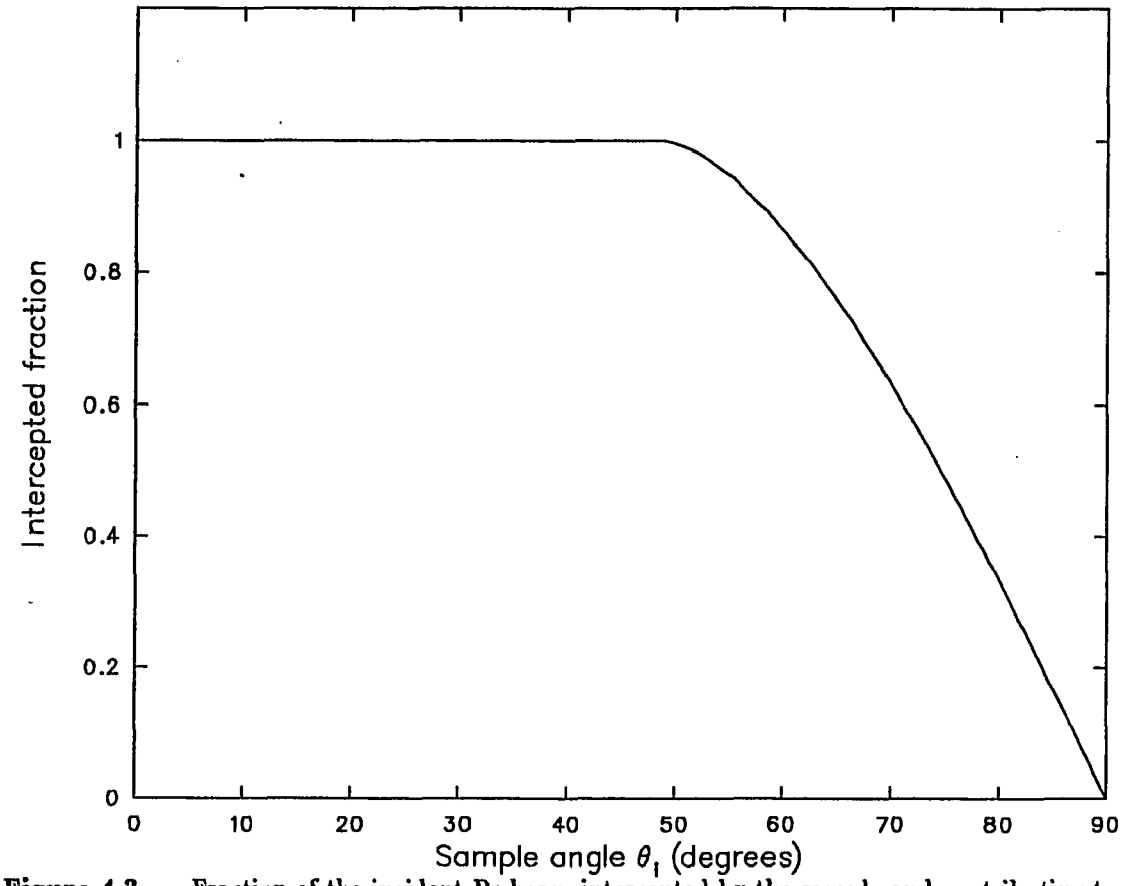

Figure 4.3 — **Fraction of the incident Ps beam intercepted by the sample and contributing to the reflection process as a function of the sample angle.**

4.2. The Reflection Data

In this section I will discuss my data and the individual steps leading to reflection fractions. I shall outline the two ways used to collect data in the first part. Using one experimental run as an example I will explain all the steps taken to obtain the reflected fraction from the raw data. Finally I will present all results from the various runs and discuss them. A simple theory to explain some of the results will be presented in the following section.

4.2.1. Two ways of data collection — As I explained before the large amounts of lead shielding around the scintillators make any changes in the position of the detectors during a run impractical. Instead they were kept fixed for each run and the sample was rotated, i.e. the angle θ_i was changed, while the Ps beam energy was also kept constant. In the second type of runs the Ps energy is ramped by changing the bias on the gas cell. In that case all angles remain unchanged.

Except for in one case LiF(100) was used as the sample. A crystal purchased from the Harshaw company of 7/8th of an inch by $1 inch$ area was cleaved in air and mounted on the manipulator in the vacuum system within an hour. The sample was mounted with a (100) axis in the plane formed by the positron beam and the sample detector axis. Prior the the experiments no surface analysis was performed but a later study revealed a sharp LEED pattern.

In most cases the sample was rotated through the specular condition and in a second run the energy dependence of specular reflection was measured. To further reduce the amount of contaminations on the sample surface and prevent the

adsorption of water the sample was heated to $160°C \pm 10°C$. The sample mount also includes a heater stage employing a resistive heating method.

4.2.2. Angle scans — In this case the detectors were held in a fixed position and also the Ps beam energy was constant. The sample was turned through a number of angles. Some of them were negative angles, where any reflected Ps moved away from the detectors. In some of the runs the data collection program alternated between periods of "beam on" and "beam off". In the "beam on" mode Ps was allowed to form in the gas cell, while in the "off" situation the positron beam was repelled in front of the gas cell by a large potential V_1. A computer program controlled the actual measurement. It sent pulses to the various power supplies that provided the potentials for the gas cell and the "beam off" grid. Via a third link the program directed the rotation of the sample with a stepping motor. The minimum step size was 1.8°. The accumulated counts in energy windows of the two BGO scintillators and in the coincidence channel were stored for each gas cell potential and a selected number of sweeps. If measured, the "beam off" counts were stored separately. A piezoelectric leak valve regulated the pressure in the gas cell according to feedback from the ionization gauge controller. Examples are shown in figure 4.4 and figure 4.5 for one singles channel and the coincidence channel of the same run. The parameters for this run are given in table 4.1.

It becomes obvious in the singles channel that only a small fraction of the background signal can be attributed to sources other than positron or Ps related ones. On the other hand almost all of the positron or Ps related counts appear to

Table 4.1: Parameters of an "angle scan"; $\psi = 120°$

Reference time t_0	12:00; 5/16/88
Positron intensity at t_0	$3.85 \times 10^6 e^+$/sec
Beam energy	149.6eV
Gas pressure and type	10^{-3}torr of Ar
Sample	LiF(100) heated to $\approx 160°$C
Start time	17:57; 5/16/88
Stop time	09:29; 5/17/88
Gas cell potential V_2	122V
Ps energy E_{Ps}	18.7eV
Gas cell efficiency at E_{Ps}	1.394 counts seen per 10^6 e^+
Total angle ψ	120°
Counting mode	Beam on and off
Number of sweeps	13

be not reflection related since the rates remain as high when the sample is turned the other way (negative angles). Only in the coincidence channel can a sharp peak with a width of about 5° be observed. The background counts are greatly reduced. While the difference between "beam on" and "beam off" counts is the same for positive and negative angles (except for the actual peak area) the absolute number of counts is slightly larger for the positive angles. This can be attributed to high energy positrons from the source reaching the sample and forming Ps at the surface.

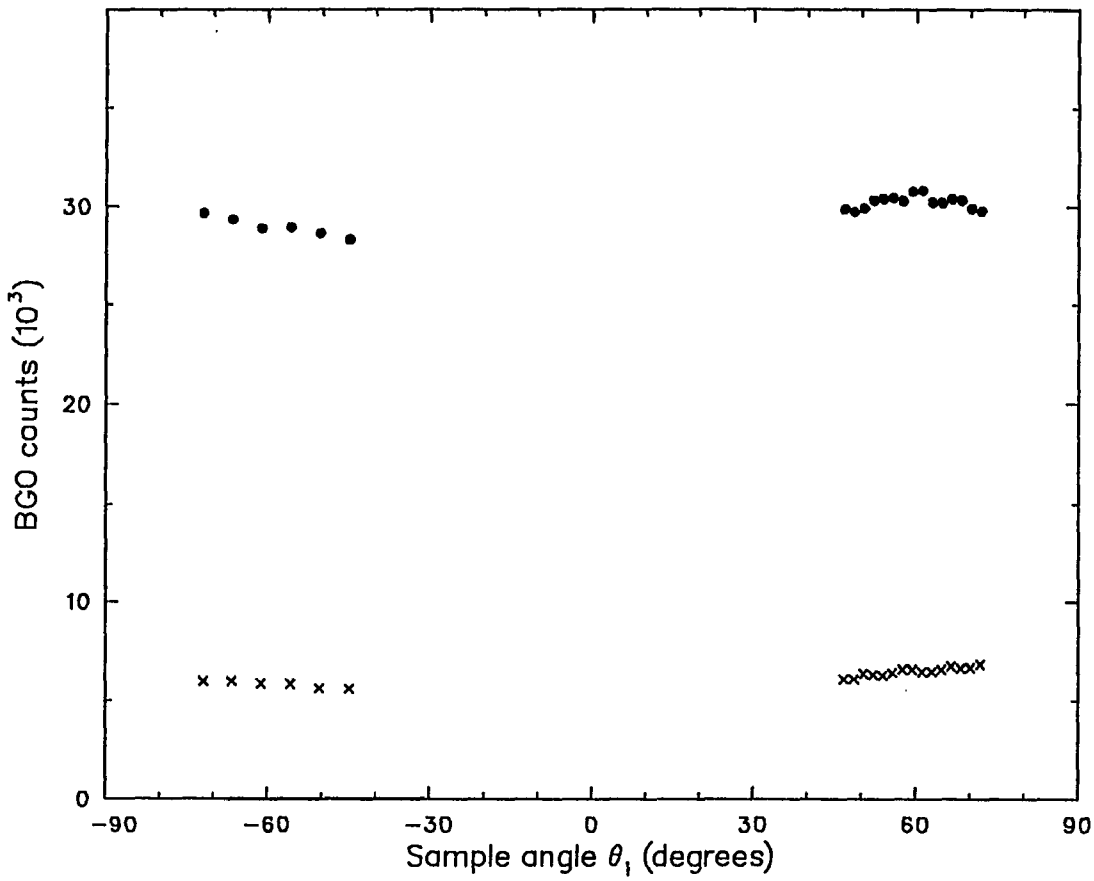

Figure 4.4 — Raw data of a Ps reflection measurement. Show are the counts in the $511keV$ window of one of the BGO scintillators versus the sample angle. • "beam on" data; × "beam off" data. The statistical errors are smaller than the symbols.

This effect is independent of turning the beam "off" but should disappear when the sample is turned away.

The best way to eliminate the background is to subtract the "beam off" data for all angles and the reverse the sign of the negative angle data. This was done in the next figure (fig.: 4.6). The dashed line represents the average of all of the formerly negative angle values. That value lies at 17.01 counts ±2.38 counts. The errors have been calculated from the "on" and the "off" data using the sum of the squares and then taking the square root again.

For the next step I subtract the average of the negative angle values and correct the error values accordingly. The result is shown in figure 4.7. Now any

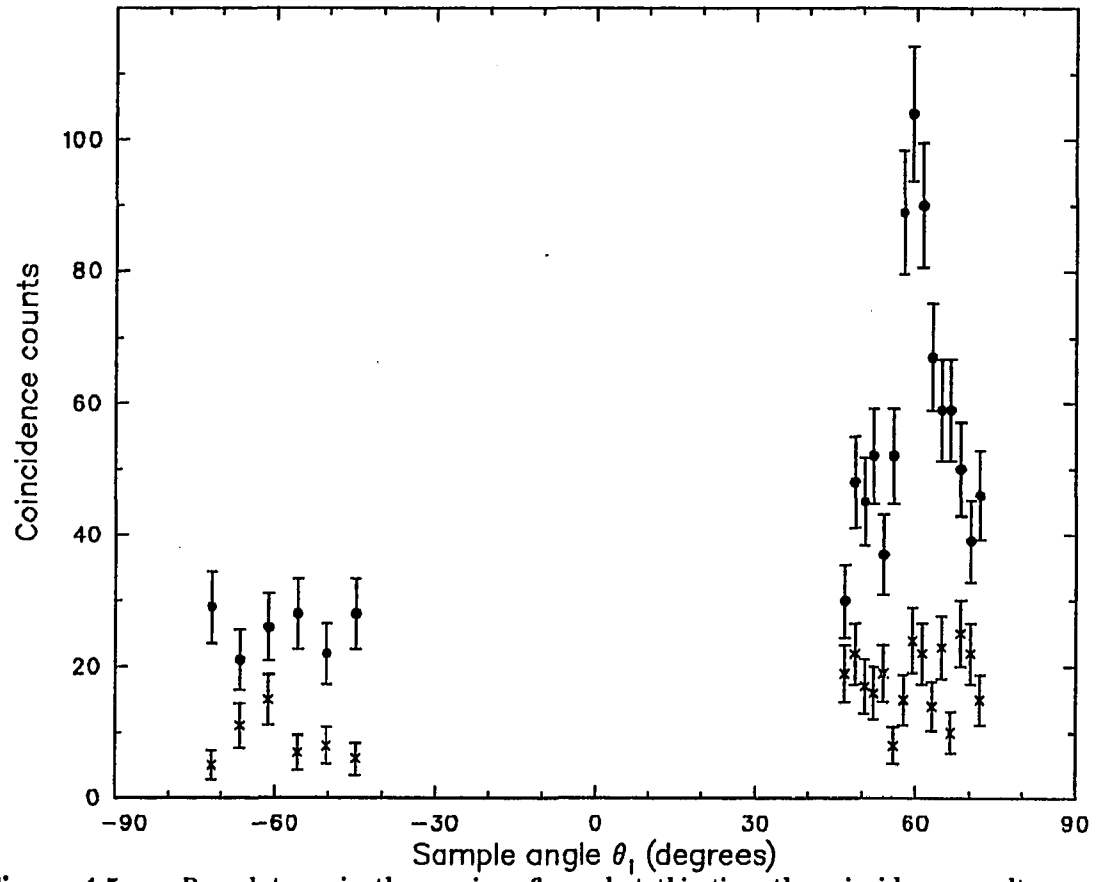

Figure 4.5 — Raw data as in the previous figure but this time the coincidence results are shown.

background is eliminated from the measured signal. Most of all any time independent counts are gone. Only now can I correct the signal for the effects of the decaying source according to the method described earlier. Using the known decay rate of the ^{64}Cu source I can calculate the the rate that I would have obtained if the measurement was performed at the reference time t_0. This result can then be normalized by the established positron rate at that time and the Ps formation efficiency for the energy (see table 4.1). Finally the count rate needs to be corrected for the fraction of Ps atoms that miss the sample and cannot contribute to the reflection process. The thus obtained reflection fraction is presented in figure 4.8.

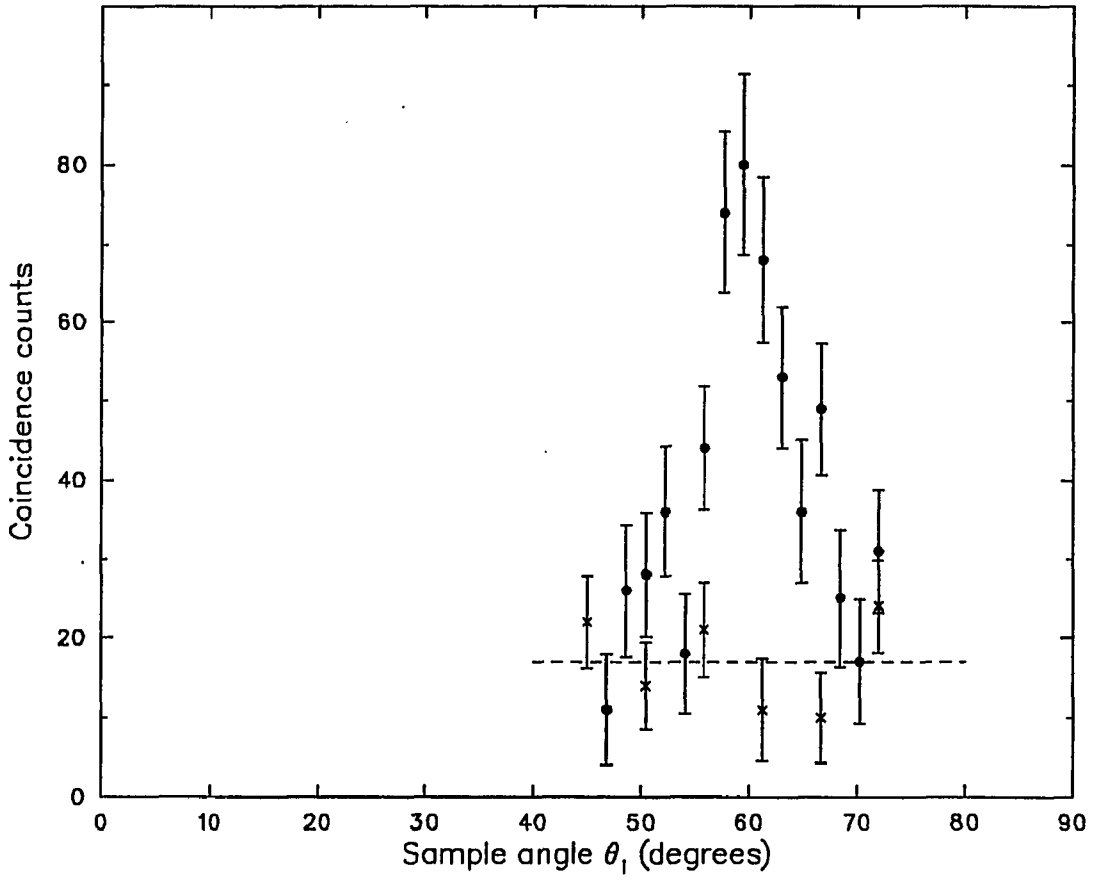

Figure 4.6 — Coincidence counts of the same reflection measurement. The "beam off" values have been subtracted. • Positive angle data, and × negative angle data for which the sign of the angle was reversed. The errors are a combination of the "on" and "off" data errors.

Shown is the reflection coefficient versus the sample angle. No error due to the various normalizing values was not included into the displayed error values.

In this measurement the background signal was obtained with the positron beam turned off. They are different depending on the sign of the sample angle, but make up only a fraction of the background (about 1/3 of the background with the sample in the negative angle position). Also I assume that this difference is roughly constant. On the other hand half of the actual measuring time was invested on the "beam off" part. In order to estimate the error made when I do not measure "beam off" rates I repeat the analysis without the "beam off" data. The outcome is shown

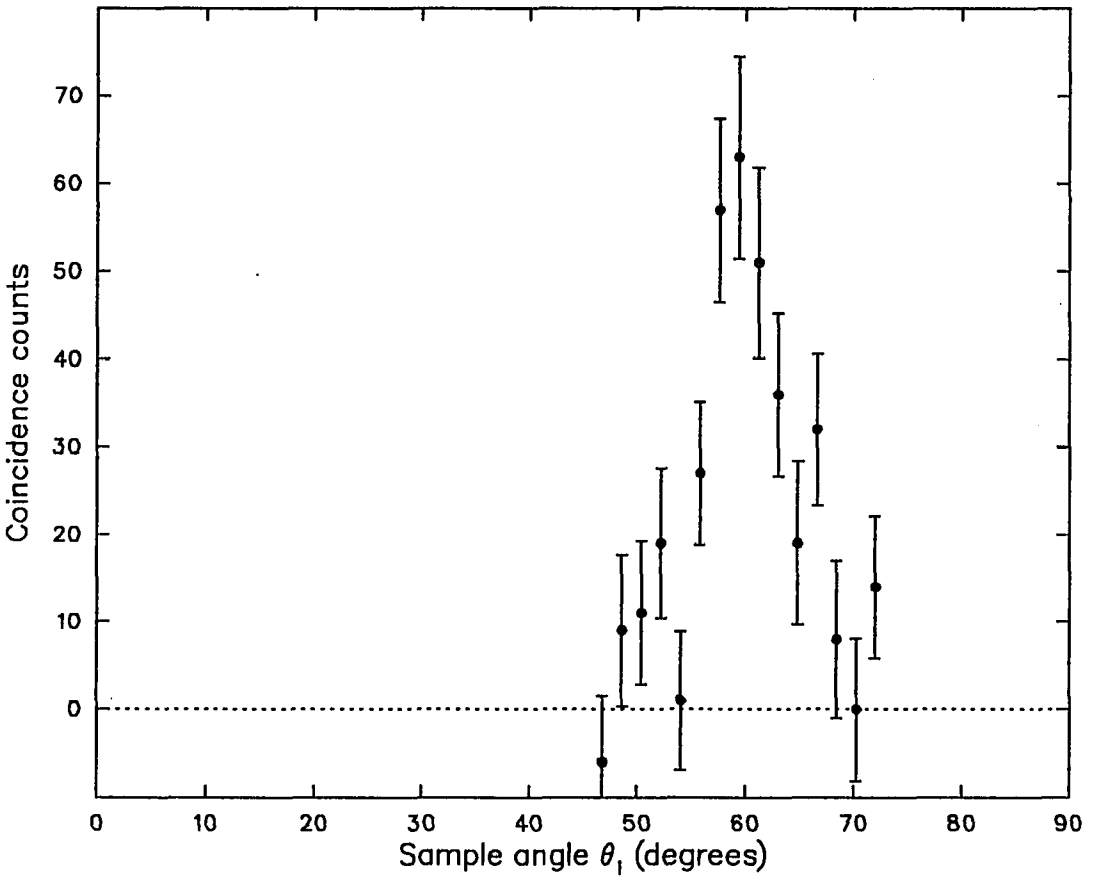

Figure 4.7 — The coincidence data that have been obtained by subtracting the average of the negative angles. The error of the average value of 17.01 counts (2.38 counts) and the original statistical errors have been combined.

in the next figure (fig.: 4.9). In this case the difference is on the order of a quarter of a percent. The errors of either values still overlap. This fact has to be kept in mind when no "beam off" data are available and constant reflection fractions are observed which are on this order of magnitude.

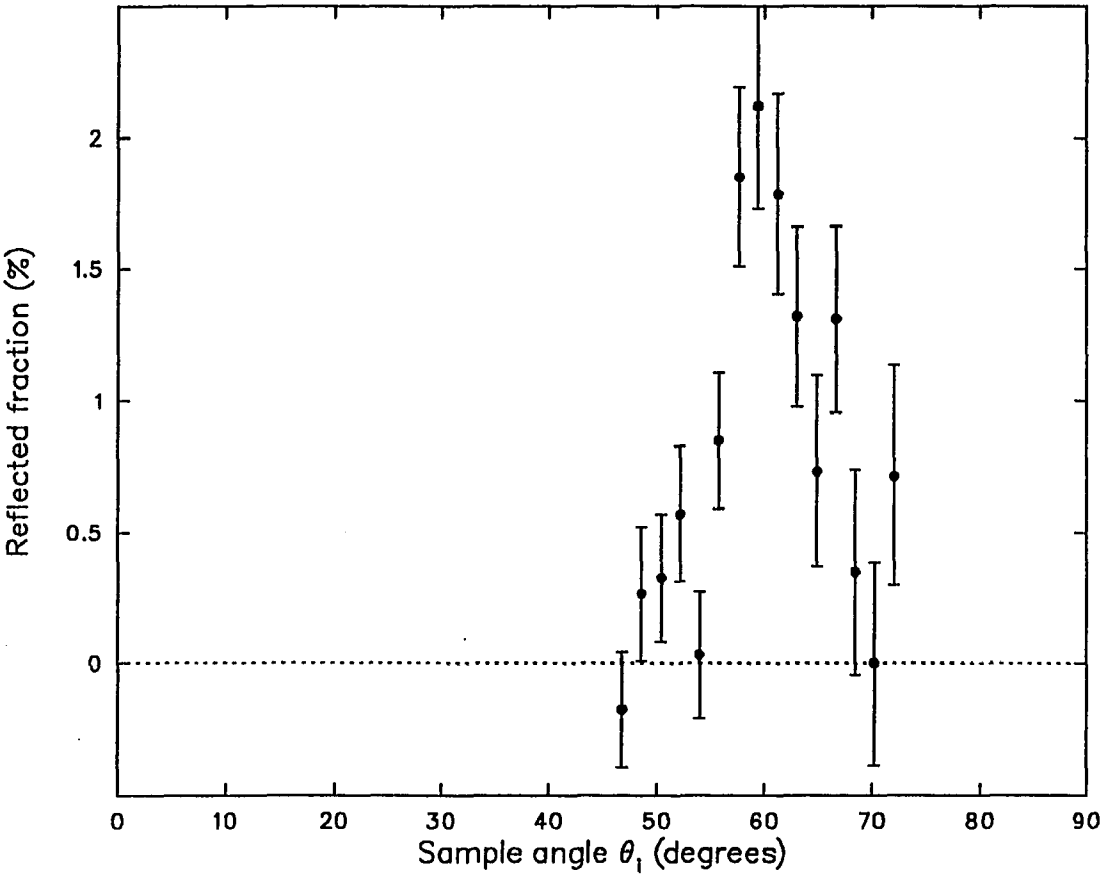

Figure 4.8 — Ps reflection from LiF(100) as a function of the sample angle. A beam of 18.7eV Ps atoms was directed at the sample and the fraction scattered through a total angle of $\theta_i + \theta_r = \psi = 120°$ was measured. The fraction peaks at the specular condition.

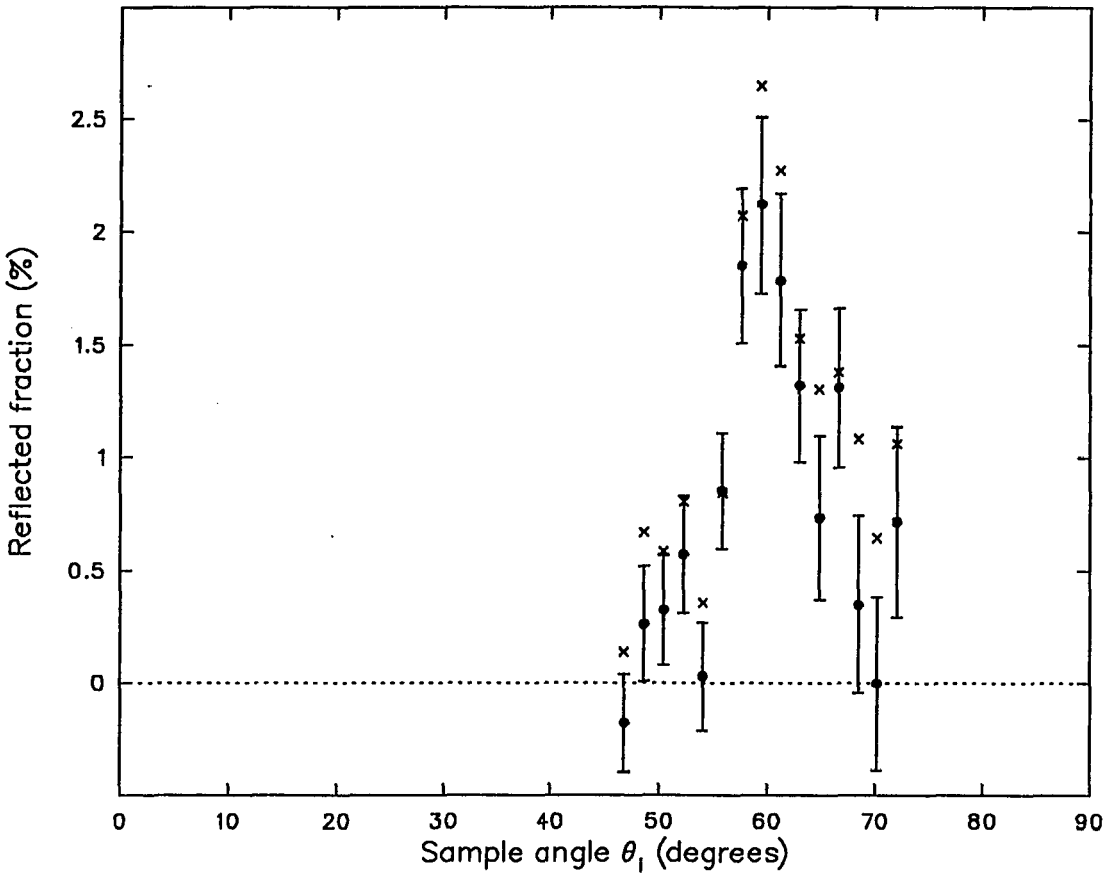

Figure 4.9 — Comparison of the results of an analysis with (•) and without (×) the "beam off" data. Only one set of error bars is shown. The other set has about the same magnitude.

Results of such a measurement without the "beam off" data are shown in the following set of figures. The parameters for this run are shown in the table 4.2 below.

Table 4.2: Parameters of an "angle scan"; $\psi = 100°$

Reference time t_0	15:00; 5/02/88
Positron intensity at t_0	$4.57 \times 10^6 e^+$/sec
Beam energy	149.6eV
Gas pressure and type	10^{-3}torr of Ar
Sample	LiF(100) heated to $\approx$ 160°C
Start time	17:18; 5/02/88
Stop time	12:09; 5/03/88
Gas cell potential V_2	130V
Ps energy E_{Ps}	10.7eV
Gas cell efficiency at E_{Ps}	0.649 counts seen per 10^6 e^+
Total angle ψ	100°
Counting mode	Beam on only
Number of sweeps	30

This time the singles counts reveal a broad peak above the roughly constant background for negative angles. The width of the peak is basically due to the poor angular resolution of a single detector. The coincidence result on the other hand is

much sharper with about 5° FWHM. The analysis along the same lines reveals a specular reflection coefficient of about 10% for the $10.7eV$ Ps beam.

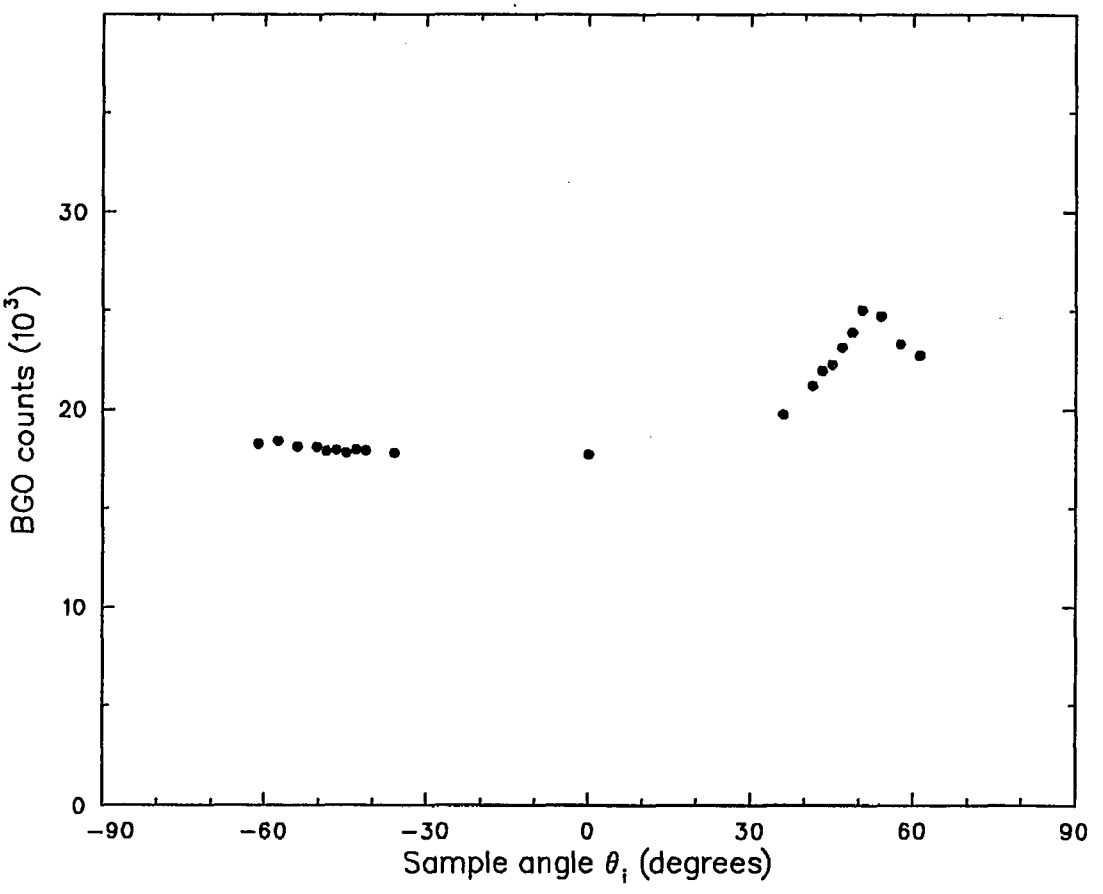

Figure 4.10 — Raw data for Ps reflection seen in the $511keV$ window of one BGO scintillator. The data are versus the sample angle. The detectors were located at $\psi = 100°$.

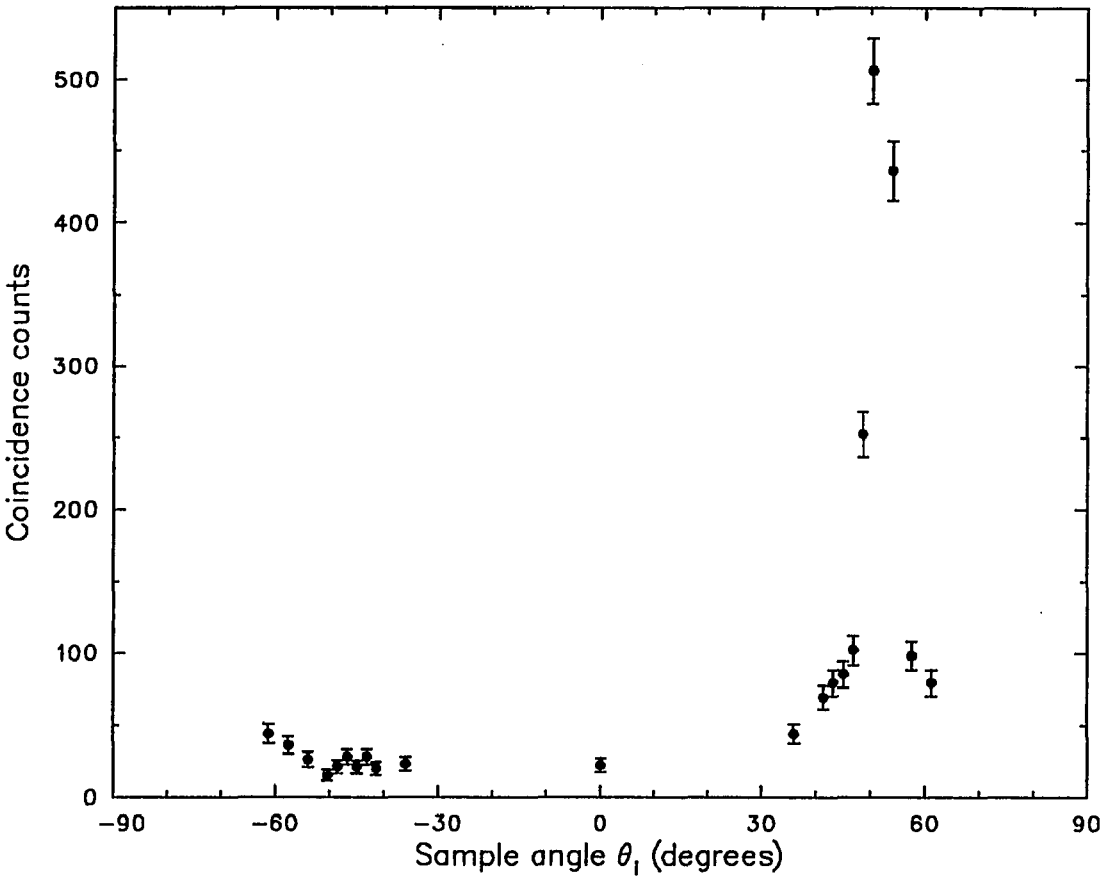

Figure 4.11 — Same measurement as in the previous figure. Shown is the result from the coincidence channel.

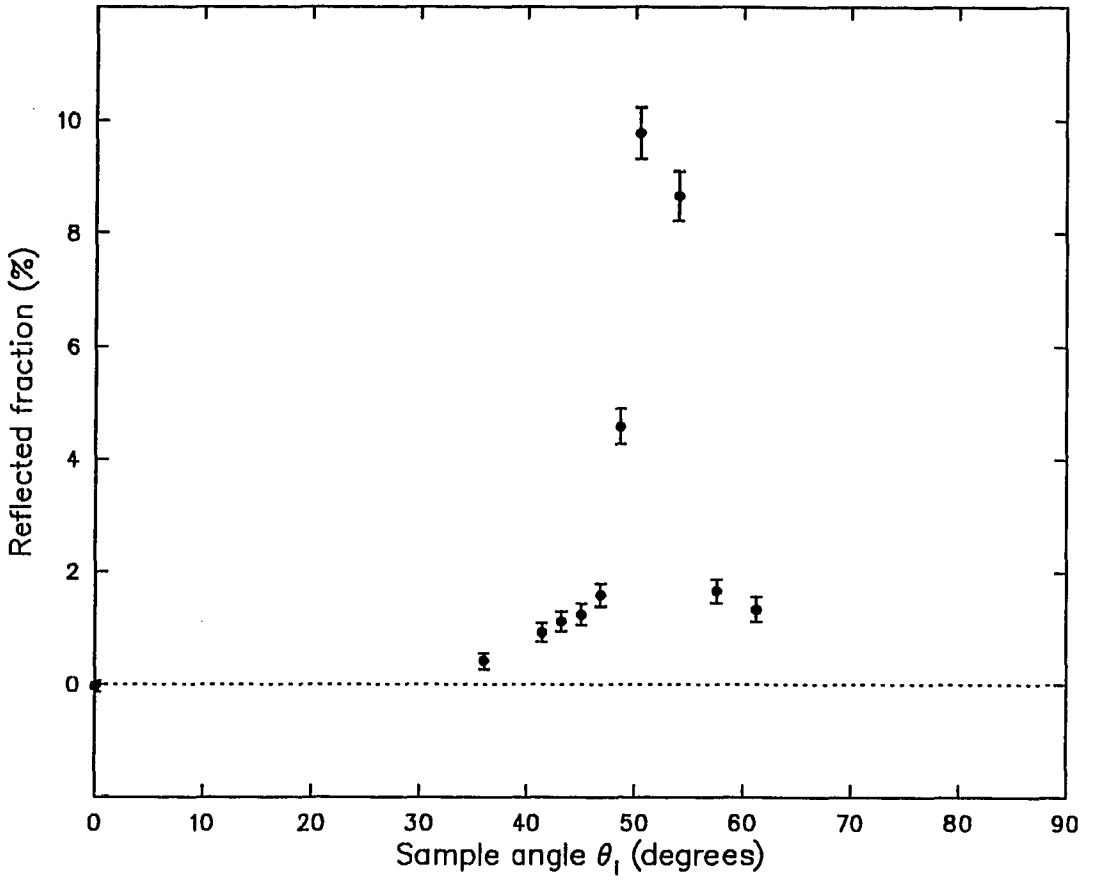

Figure 4.12 — Ps reflection through 100° from LiF(100). Shown is reflected fraction versus the sample angle. (Same measurement)

4.2.3. Energy scans — During these measurements both angles θ_i and θ_r are held constant. In all but one case they are selected to comply with the condition for specular reflection. The Ps beam energy is then changed by varying the potential on the gas cell. One experimental run consists of several sweeps of the gas cell potential. For each point data are accumulated in the two singles channels of the $511keV$ peak windows of the BGO scintillator and their coincidences both for the "beam on" mode and the "beam off" mode. Once all voltages have been swept the sample is turned to the negative angle position and the same is repeated in the second half of the sweep. Thus both ways of measuring the background are included into a measurement. The systematic error due to a slightly reduced beam intensity for the negative angle position can be kept below 5% as long as the duration of one sweep remains below 1hour. A slightly modified version of the program described above controls this process. The parameters for such a run are shown in table 4.3 and the raw data in figure 4.13 for one singles channel and in figure 4.14 for the coincidence channel.

Just like in the angle scans the "beam off" data are constant and slightly larger when the sample is in the positive angle position (Ps reflected towards the detectors). In addition to the effect of high energy positrons generating Ps at the sample this is also due to the time shift and the resulting lower beam intensity of the negative angle measurements. The difference in the singles rates amounts to 271 ± 10 counts total. The reflection data show one broad peak on top of a roughly linear background which decreases with increasing gas cell potential. A second "bump" appears above $141V$. This cannot be due to Ps reflection because here the positrons do not have enough kinetic energy in the cell to form Ps. Since it shows

Table 4.3: Parameters of an "energy scan"; $E \leq 20.7eV$

Reference time t_0	15:00; 5/05/88
Positron intensity at t_0	$3.95 \times 10^6 e^+$/sec
Beam energy	149.6eV
Gas pressure and type	10^{-3}torr of Ar
Sample	LiF(100) heated to $\approx 160°$C
Start time	15:46; 5/05/88
Stop time	09:42; 5/06/88
Total angle ψ	100°
Sample angle θ_i	$\pm 50.4°$
Correction for Ps missing the sample	1.0063
Counting mode	Beam on and off; two sample positions
Number of sweeps	5

up for both sample positions it must come from annihilations of positrons in the gas cell. Near the threshold of Ps formation the total positron atom cross section rises sharply. Less positrons will reach the exit of the gas cell. A reduced background is the result. This can be confirmed by measuring the positron transmission through the gas cell as a function of its potential and comparing data from a run with gas in the cell with one without gas. Such a comparison is shown in figure 4.15.

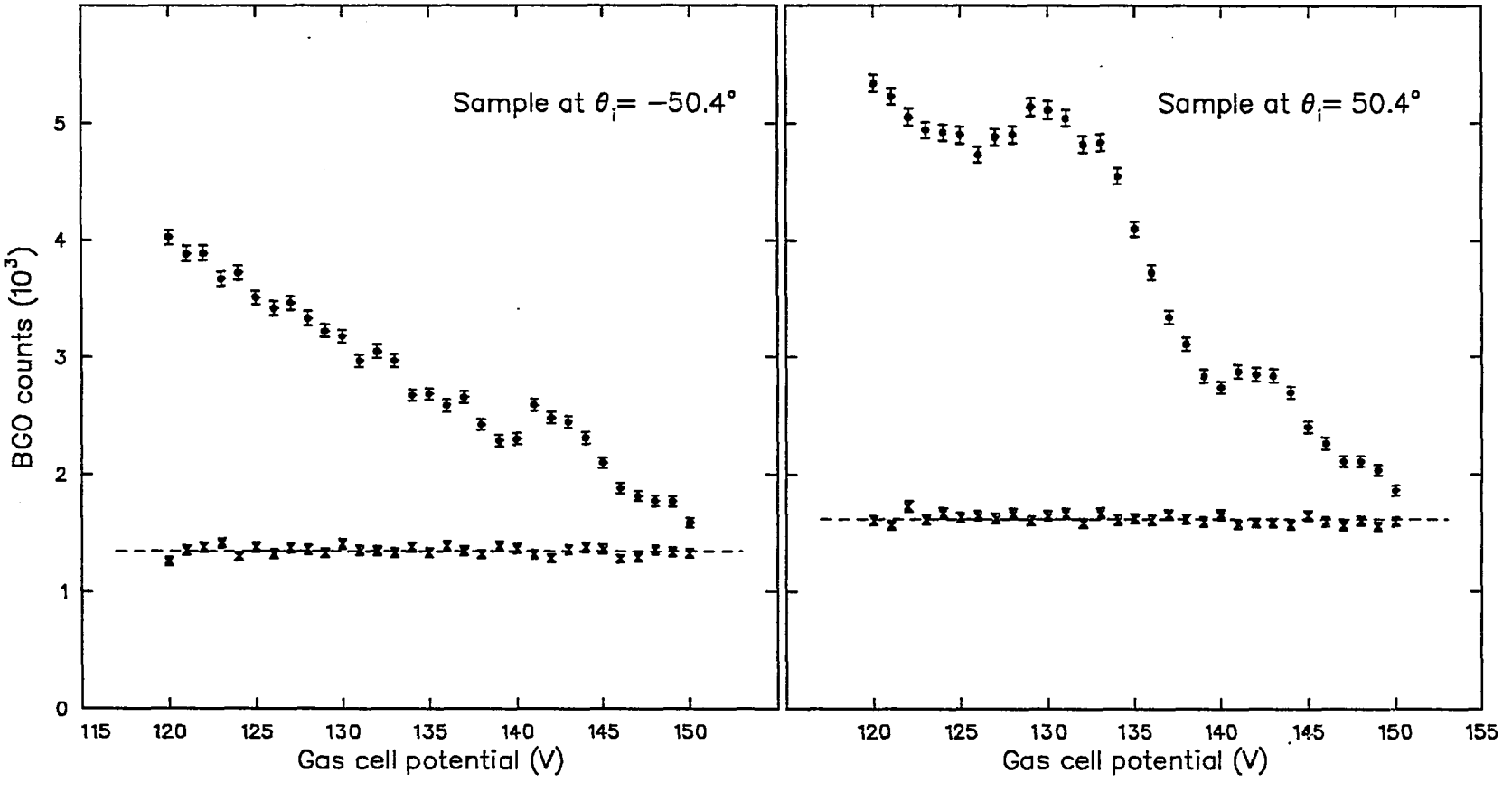

Figure 4.13 — Raw data of a BGO singles channel from an energy scan. The right figure shows the result for the sample in the position for reflection towards the detectors and the left figure in the background position for reflection away from the detectors. The scintillators and the annihilation plate were located at $\psi = 100° \pm 4°$. • represent the "beam on" data, and × the "beam off" data. The dashed lines are drawn at the respective level of the average of the "beam off" data.

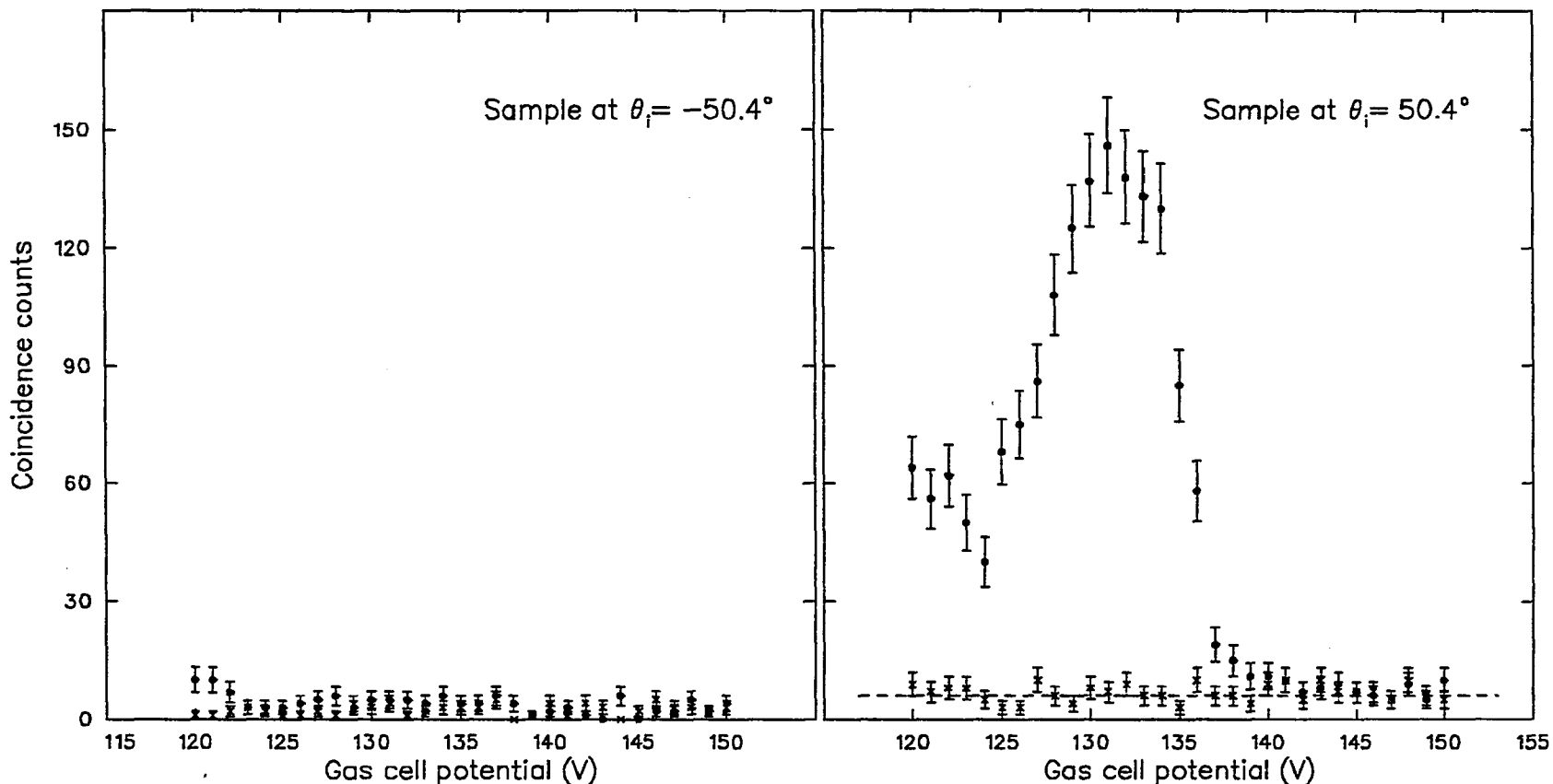

Figure 4.14 — Raw data of the coincidence channel for the same run as in the previous figure. Again the right side shows the results from the sample in the reflection position, and the left those from the background position. "Beam on" data are indicated as •, and "beam off" data as ×. The dashed line indicates the "beam off" averages.

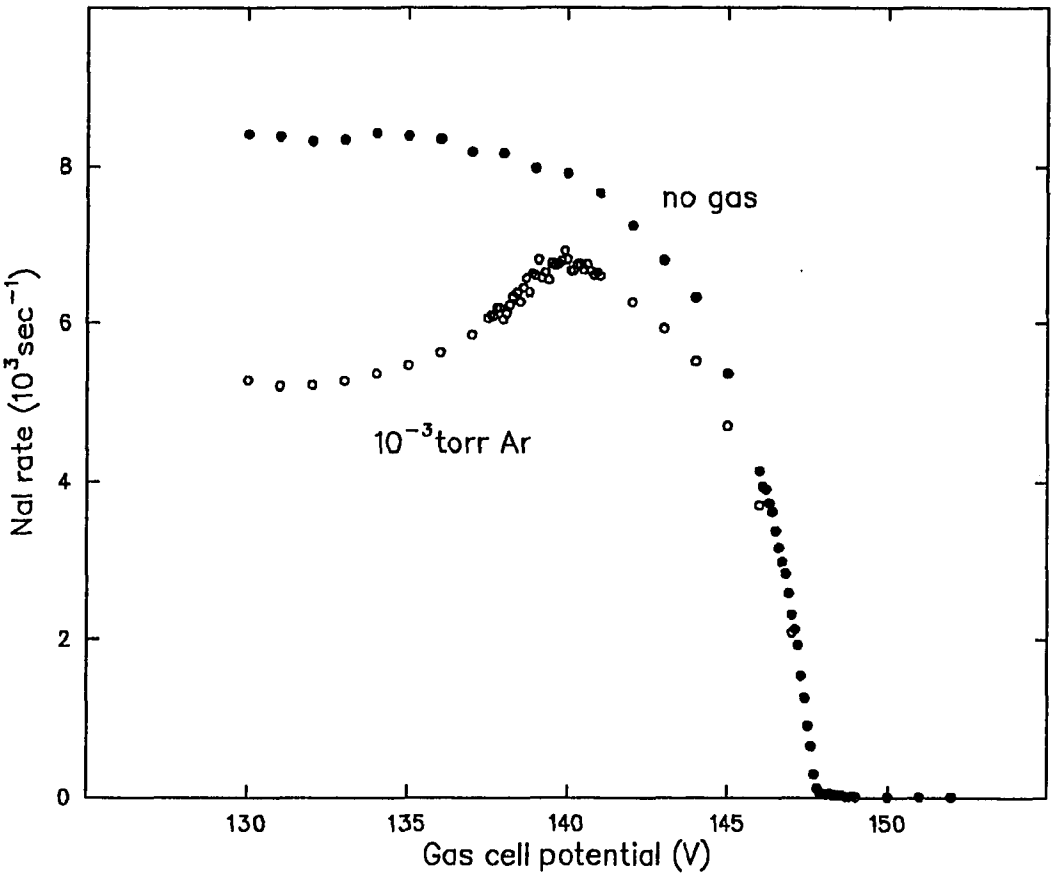

Figure 4.15 — Positron transmission through the gas cell without and with $10^{-3} torr$ Ar in the gas cell. Show is the transmitted rate as detected by the (3 × 3)NaI detector versus the gas cell potential. The positron beam energy was $147eV$. • are for the no gas case, and o for the gas case.

All the reflection features are repeated in the figure showing the coincidence results but are much more distinct. Also the background rate is greatly reduced. Here the "beam off" background accounts for all of the signal in the region where no Ps is formed in the gas cell (i.e. the gas cell potential is $> 141V$).

Again I will use the coincidence results for the further data analysis. As in the angle scans I subtract the negative angle data from the positive angle data and also subtract the average of the difference of the "beam off" data. The latter amounts to 5.94 ± 0.44 counts. Now the effect of the decaying source and the intensity of the positron beam at the reference time can be taken into account. At last I normalize

the data with the Ps formation efficiency of the gas cell and consider the fraction of Ps that miss the sample at this angle of 50.4°. The resulting reflection coefficient as a function of the Ps beam energy for specular reflection is shown in figure 4.16. Below 3eV Ps energy the data and error bars become very large. This is due to the very small initial Ps intensity. Most of the Ps will decay in flight before it can reach the annihilation plate. The data points have to be normalized by small numbers. In later figures I will omit the data points at low energies when the error bars become unreasonably large or the reflection fractions increase above unity. In this case the reflection coefficient peaks near $7eV$ Ps energy at 28% and then drops to about 2% from $17eV$ on.

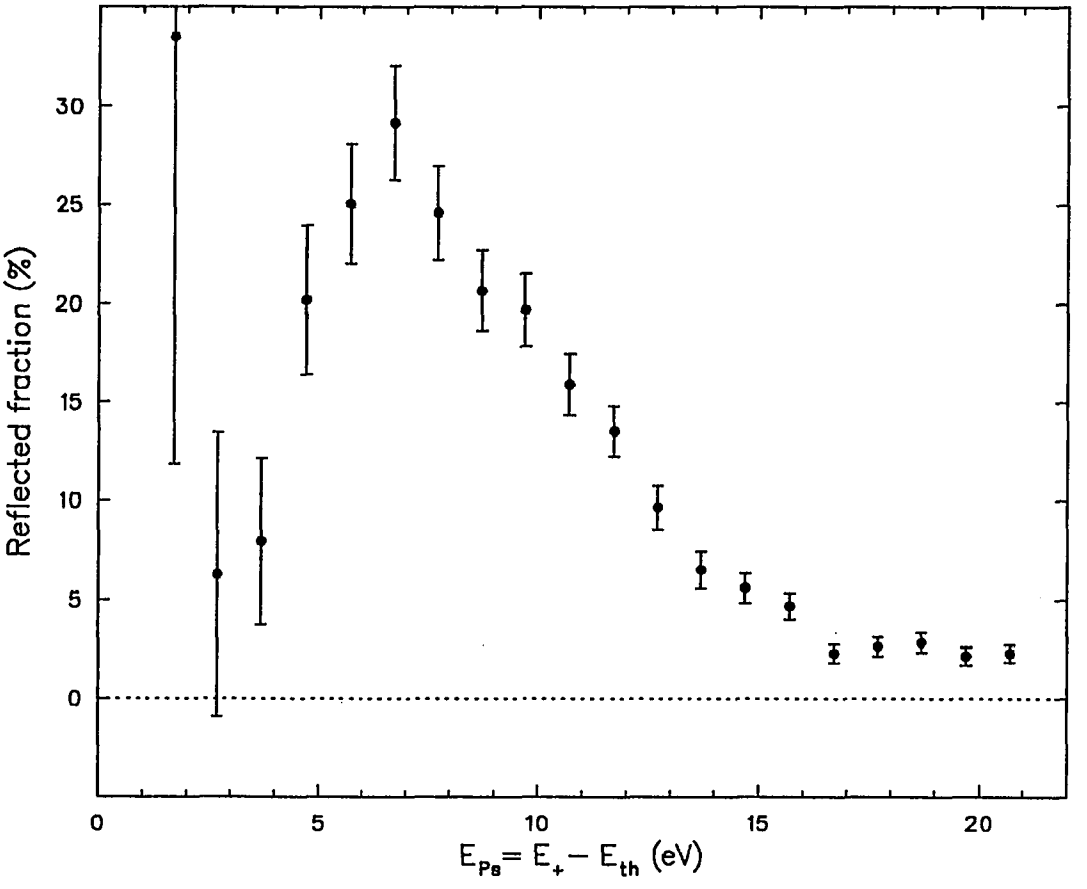

Figure 4.16 — The reflection coefficient as a function of the Ps energy. The values are calculated from the coincidence measurements shown in the previous figure for specular reflection through $\theta_i = \theta_r = 50.4°$ from LiF(100) heated to $\approx 160°$C. The error values are statistical only.

In a second measurement the Ps energy range has been extended to almost $60eV$. The parameters for that run are listed in table 4.4. In this case I omitted the measurement of "beam off" rates.

Table 4.4: Parameters of an "energy scan"; $E \geq 10.7eV$

Reference time t_0	15:00; 5/05/88
Positron intensity at t_0	$3.95 \times 10^6 e^+$/sec
Beam energy	149.6eV
Gas pressure and type	10^{-3}torr of Ar
Sample	LiF(100) heated to $\approx 160°$C
Start time	11:28; 5/06/88
Stop time	14:07; 5/07/88
Total angle ψ	100°
Sample angle θ_i	$\pm 50.4°$
Correction for Ps missing the sample	1.0063
Counting mode	Beam on only; two sample positions
Number of sweeps	19

In the following figures the results are shown just like for the previously discussed run.

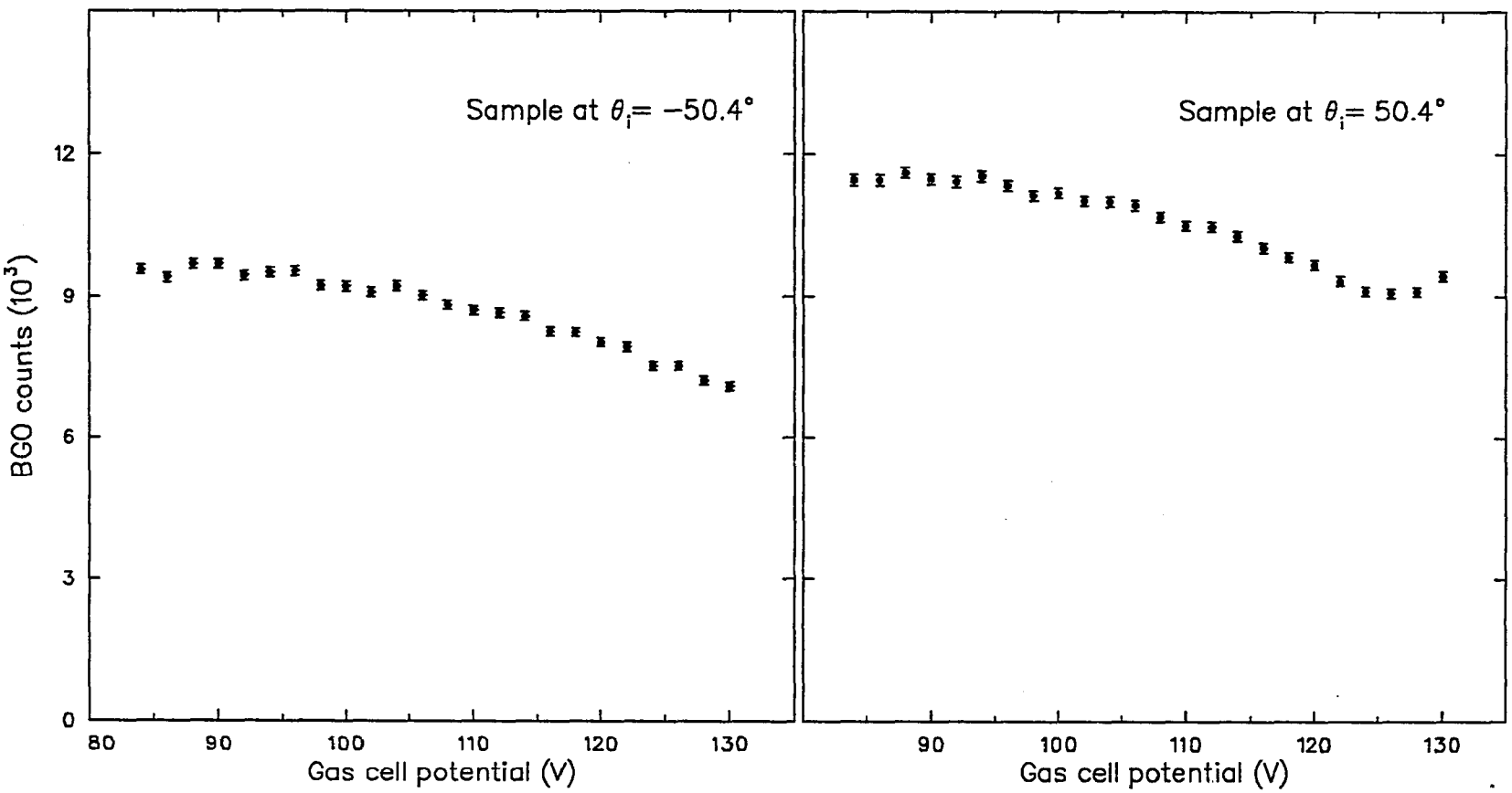

Figure 4.17 — Raw data from one of the BGO detectors versus the gas cell potential. Specular reflection through 50.4° was measured. (For more data see table 4.4.)

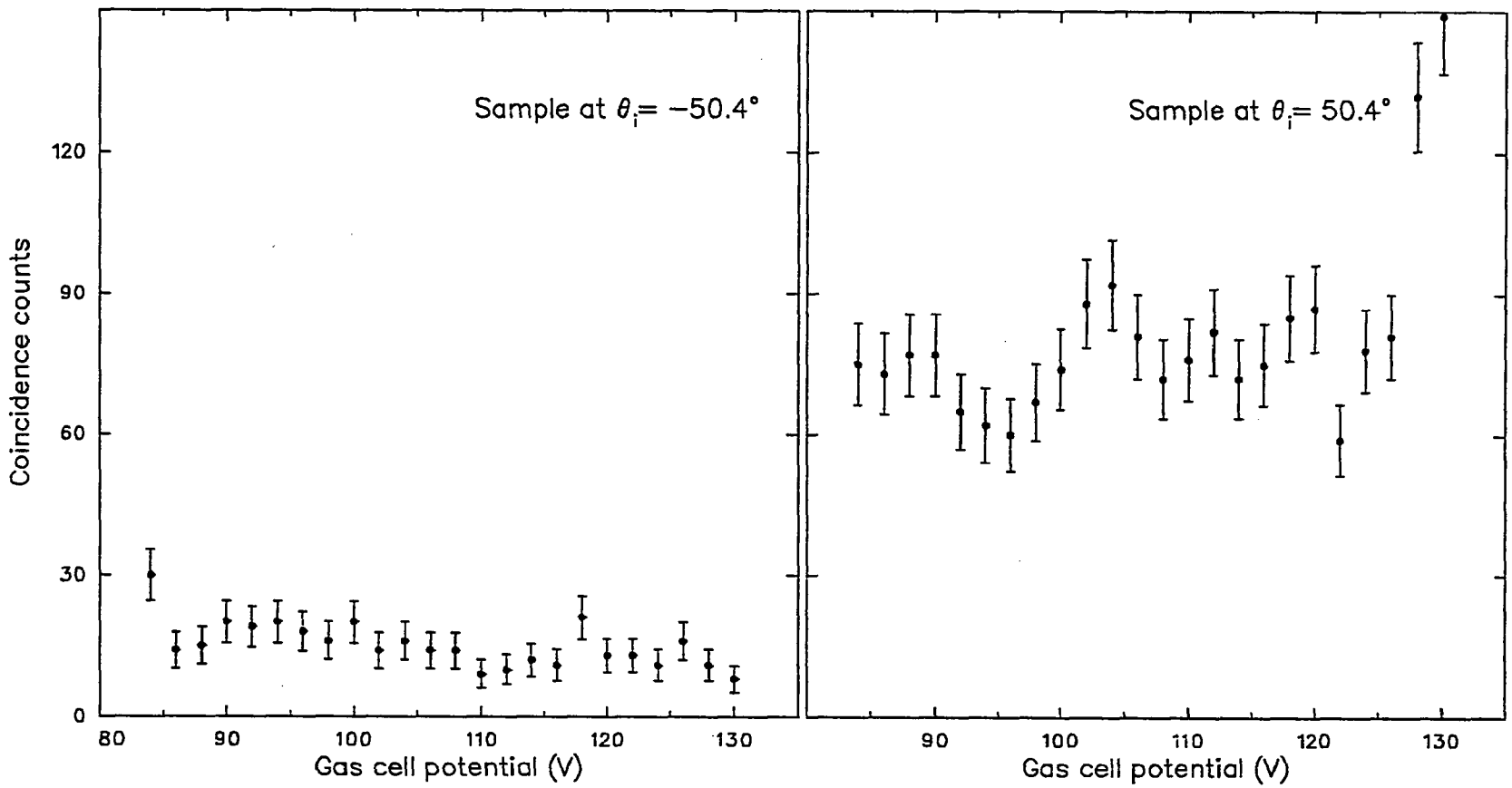

Figure 4.18 — Coincidence data for the same measurement as in the previous figure. (Specular reflection through 50.4°.)

I subtracted the negative angle results and then correct for the various effects and combined the results of the coincidence rate of this run with those from the previous run. The average of the data in the region where the two runs overlap is slightly larger for the latter run by $0.232 - 0.186 = 0.046 \pm 0.017$ counts/sec (see figure 4.19). This must be due to the fact that the difference in "beam off" counts could not be taken into account. Thus I subtract this amount from the second data set. Now I can combine the runs and evaluate the reflection coefficients which are shown in figure 4.20. Where two data points were available they have been averaged.

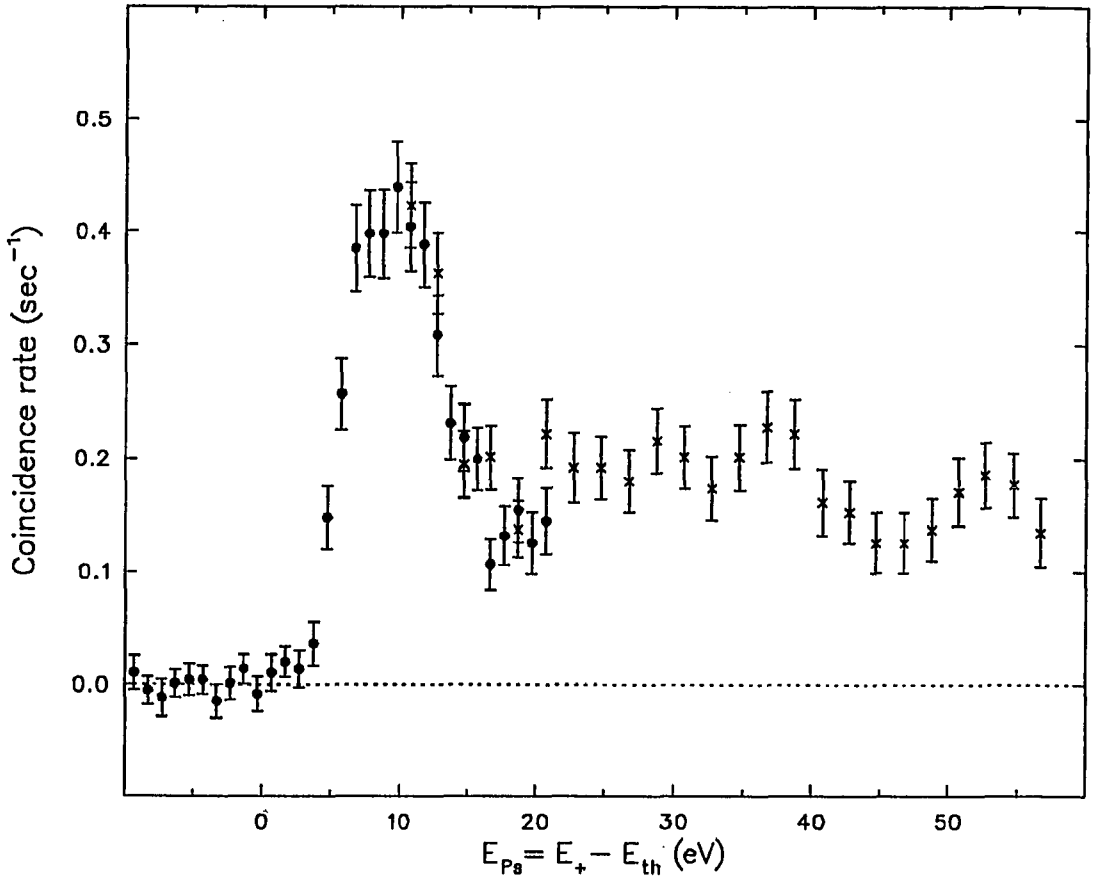

Figure 4.19 — The coincidence rates for Ps reflection through $\theta_i = \theta_r = 50.4°$ for the discussed two measurements. In the case of • "beam off" data were taken, and for × they were not available. (See text)

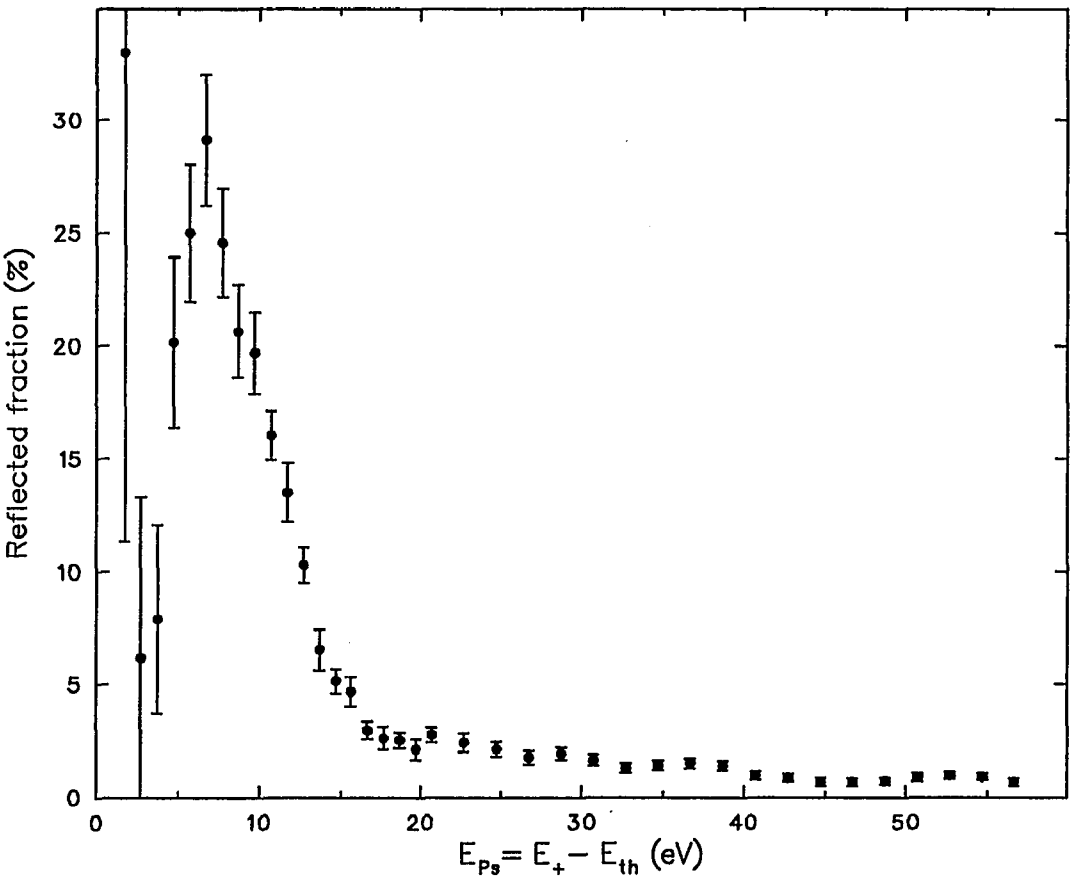

Figure 4.20 — Ps reflection coefficients as a function of the Ps energy. An estimate of the difference in the "beam off" rate for the higher energies above 20eV was included.

The same data are also shown on a double log scale in the next figure.

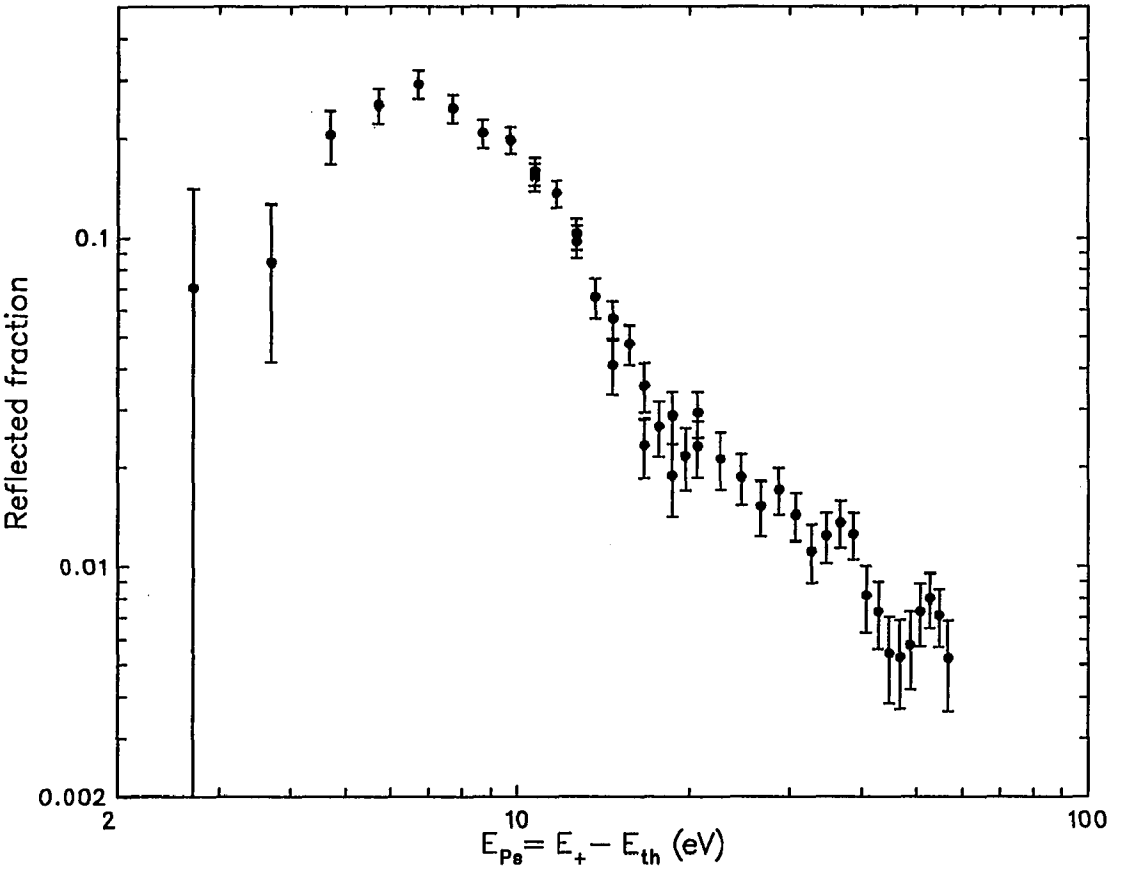

Figure 4.21 — The same Ps reflection results versus the Ps energy on a double log scale.

4.2.4. The data — The results of all other measurements have been analysed in the same fashion. Data were taken for various total angles ψ in angle scans as well as energy scans. For the angle scans the Ps beam energy was also varied. In the case of energy scans all but one measurement were made at the specular condition. They are listed below in tables 4.5 and 4.6 for an overview. In all cases the gas cell was filled with 10^{-3}torr of Ar gas. The same LiF(100) crystal was used. The calibration of the detector electronics was kept constant.

The smallest total angle possible was $\psi = 100°$. The energy scans for that angle with the sample located near the specular condition of $\theta_i = 50.4°$ were already shown and analyzed in the previous section as an example. I show it here once more on a log-log scale in figure 4.22. Along with this measurement come three angle scans at various energies. These energies are $10.7eV$, $17.7eV$ and $40.0eV$ and are shown in figure 4.23.

I estimate the uncertainty in the sample position to about $\pm 2°$ and that for the total angle to about $\pm 4°$. Within these errors the angle scans all show a peak at the specular condition of $\theta_i = \frac{1}{2}\psi$. As a function of energy the reflected fraction is about 28% at $7eV$ and drops sharply to 2 to 3% near $20eV$. Even at $55eV$ still about 1% of the incident Ps beam is reflected into the detectors. The latter raises strong hopes that a diffraction pattern can be observed.

Below $7eV$ the picture is less clear. Some data points indicate that the reflection coefficient drops also. At very low energies the values begin to become very uncertain and large. That behaviour can be explained by the uncertainty in

Table 4.5: Ps reflection "angle scans"

Angle $\psi(°)$	Angle $\theta_i(°)$	Ps energy (eV)
100	36.0 to 61.2	10.7
100	32.4 to 63.0	17.7
100	32.4 to 63.0	17.7
100	37.8 to 52.2	40.0
120	30.6 to 77.4	6.8
120	46.8 to 72.0	18.7
130	30.6 to 79.2	25.7
130	55.8 to 72.0	27.2

Table 4.6: Ps reflection "energy scans"

Angle $\psi(°)$	Angle $\theta_i(°)$	Ps energy (eV)	Comments
100	46.8	-12.9 to 20.1	Off specular
100	50.4	-9.3 to 20.7	
100	50.4	10.7 to 56.7	Continuation of above run
120	59.4	-8.3 to 30.7	
120	61.2	-5.3 to 15.7	
130	70.2	-1.3 to 40.7	
98	19.8	-4.3 to 60.7	Surface diffraction

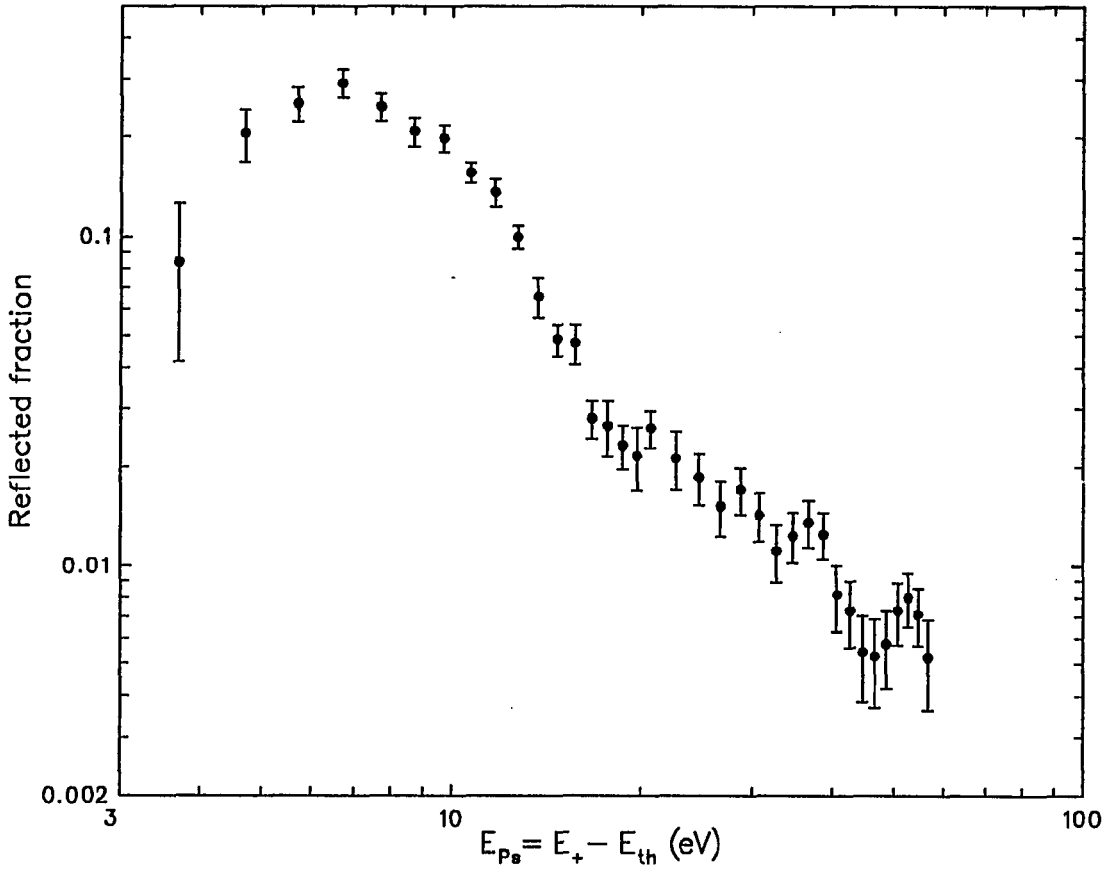

Figure 4.22 — Specular Ps reflection from LiF(100) with the sample at $\theta_i = 50.4°$ on a double log scale. shown is the fraction reflected into the detector solid angle versus the energy of the Ps beam. I estimate the error in the detector position to be $\Delta\psi = 4°$. The error in θ_i is 2°.

the normalization curve. Very little of the formed Ps reaches the detectors due to the decay in flight. For the evaluation of the reflection coefficient that means that the measured reflected amount has to be divided by a equally small formed amount.

Prior to the measurements I expected the reflection coefficient to be large at low energies when no inelastic channels are open. Above the threshold for excitations of electrons into the band gap and for Ps break up the reflected portion should drop.

In a second energy scan I positioned the sample 3.6° off the specular condition at $\theta_i = 46.8°$ (see figure 4.24). The very uncertain low energy values ($\leq 4eV$) aside the reflected fraction starts out near 3% and drops to less than 1% above $13eV$.

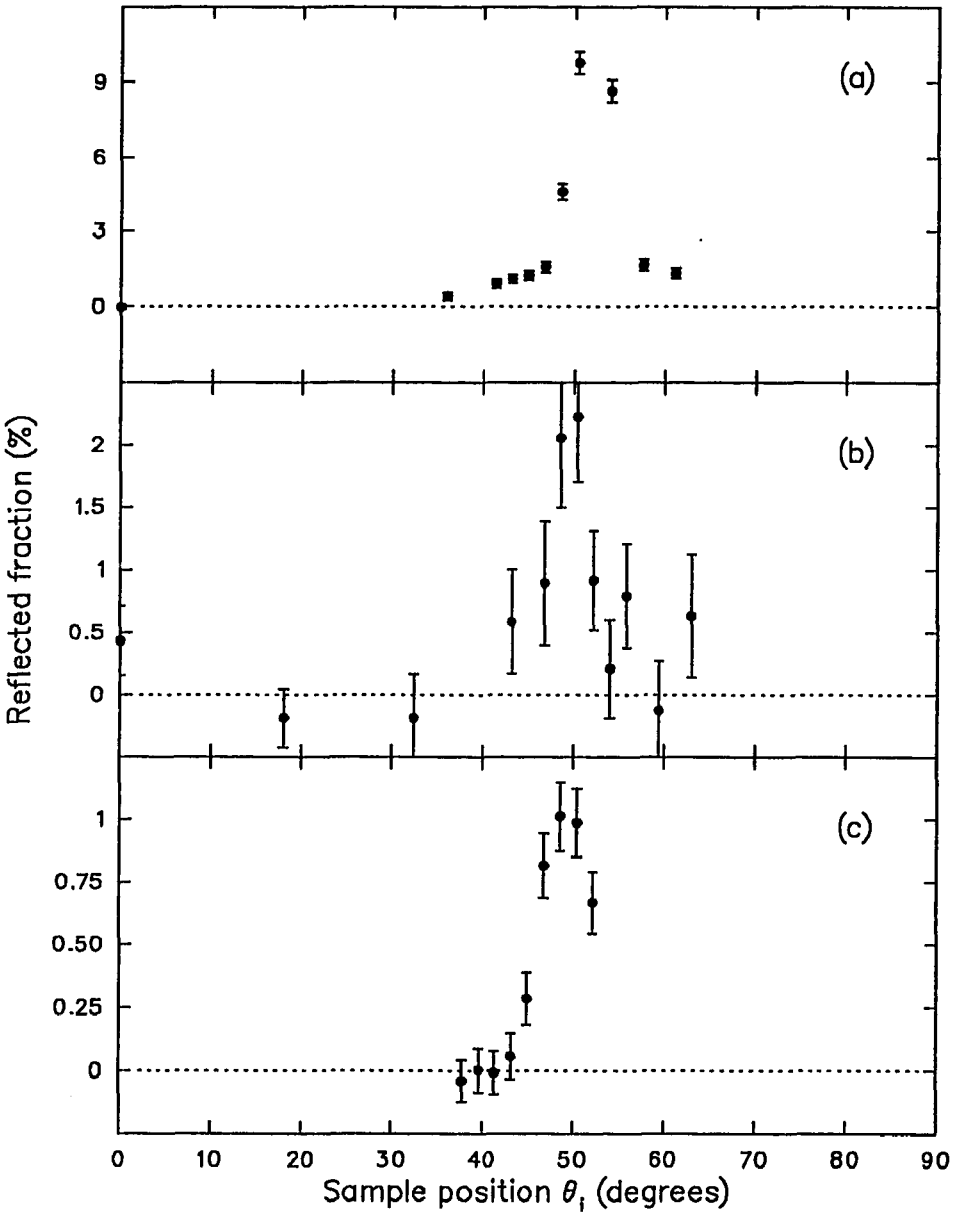

Figure 4.23 — The reflected fraction of the Ps beam as a function of the angle θ_i of the sample. The three figures represent the results for various Ps energies. In the case (a) it is $E_{Ps} = 10.7eV$, in (b) $E_{Ps} = 17.7eV$, and in the last case (c) $E_{Ps} = 40.0eV$. The detector system was located at $\psi = 100°$. Within the error bar of $\Delta\theta_i = 2°$ the peak appears at the specular condition.

Slightly larger values were the results of a repetition. Possibly the detectors were located not in the exact same position.

In the next set of data (see figure 4.25 and figure 4.26) I increased the total angle to $\psi = 120°$. In two runs the sample was first turned to 59.4° and then to

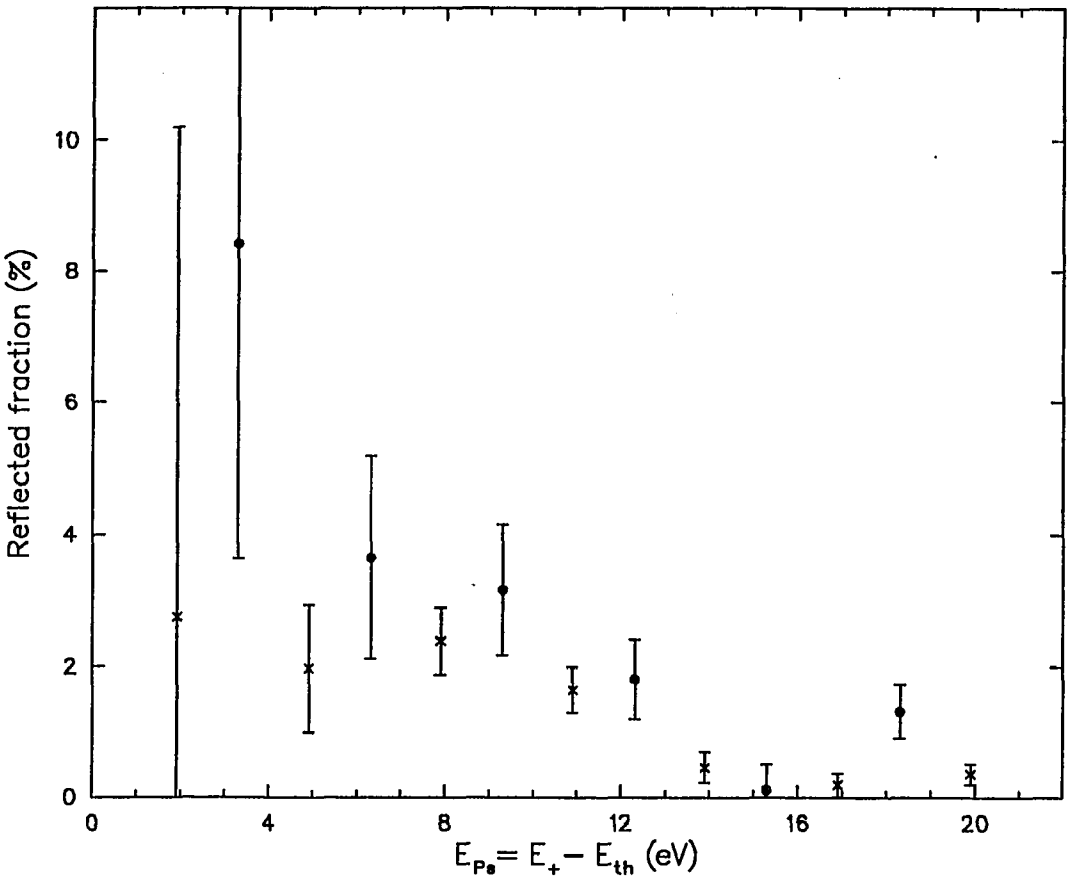

Figure 4.24 — Ps reflection from LiF as a function of the Ps beam energy. In this case the sample was rotated just off the specular condition by $\Delta\theta_i = 3.6°$ at $\theta_i = 46.8°$. The detectors are at $\psi = 100°$. With the exception of the first two points the reflected values are at about 10% of the specular results. This is further confirmation of the sharpness of the specular feature. The first two values are very uncertain due to the lack of Ps beam intensity. The two symbols represent the results of two different measurements.

61.2°. The same errors in angle apply. The energy scans show both a very similar dependence compared to the 100° data. Only the drop at low energies seems to be non existent. In the angle scans, this time measured at $6.8eV$ and $18.7eV$ the same sharp peak can be observed.

I measured one last set at a total angle of $\psi = 130°$ and a single angle scan for $25.7eV$. A second energy scan was taken 5.4° off the specular condition. All runs are shown in figure 4.27 and figure 4.28. Data below $10eV$ for the specular

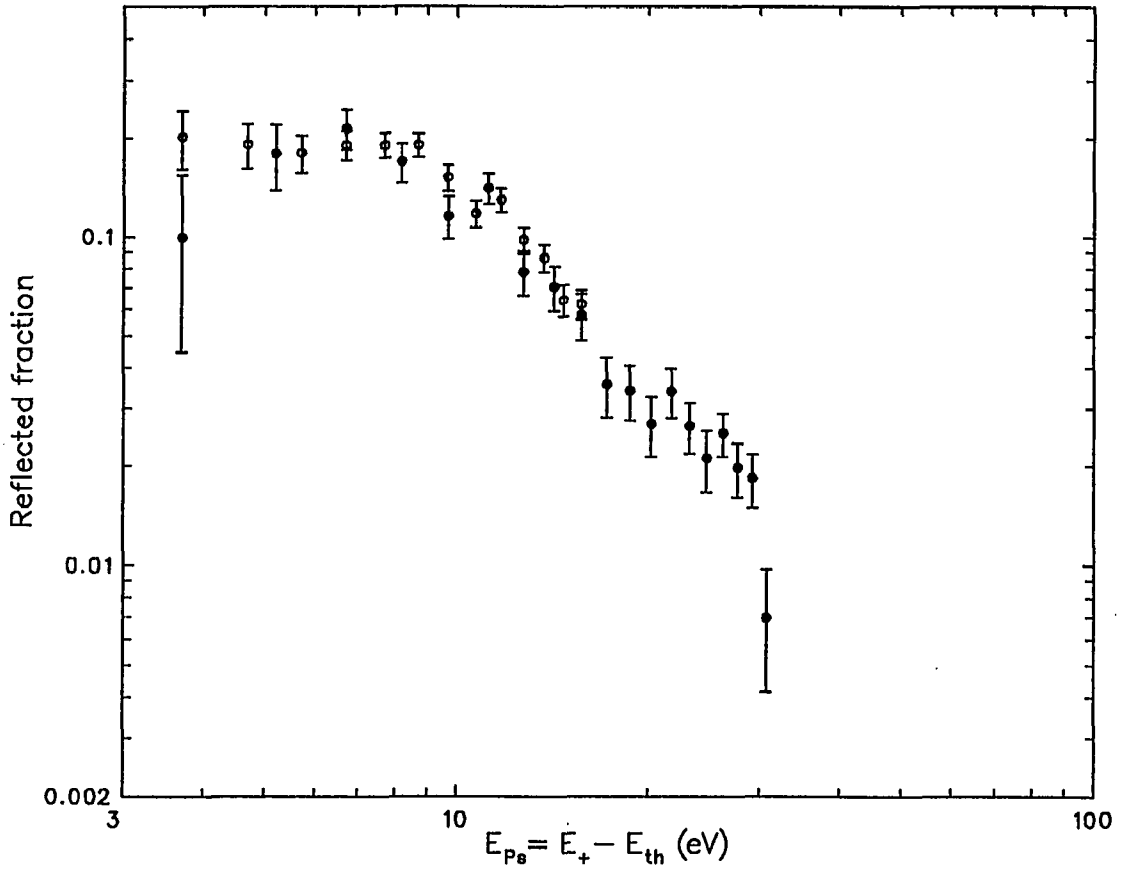

Figure 4.25 — Ps reflection from LiF with the detector system at $\psi = 120°$ on a double log scale. In the first of the two measurements shown (•) the sample was rotated to $\theta_i = 59.4°$ and in the other one (o) to $\theta_i = 61.2°$. Both cases are at specular condition within the error.

condition are missing. In the range of $10eV$ to $20eV$ their values are very similar to those for the off specular run. Only above this energy the off specular data drop off more to below 1% while the specular data remain near 3 to 4%. That is much higher than for the $\psi = 100°$ and $120°$ data. Below $10eV$ the off specular values rise to about 13%.

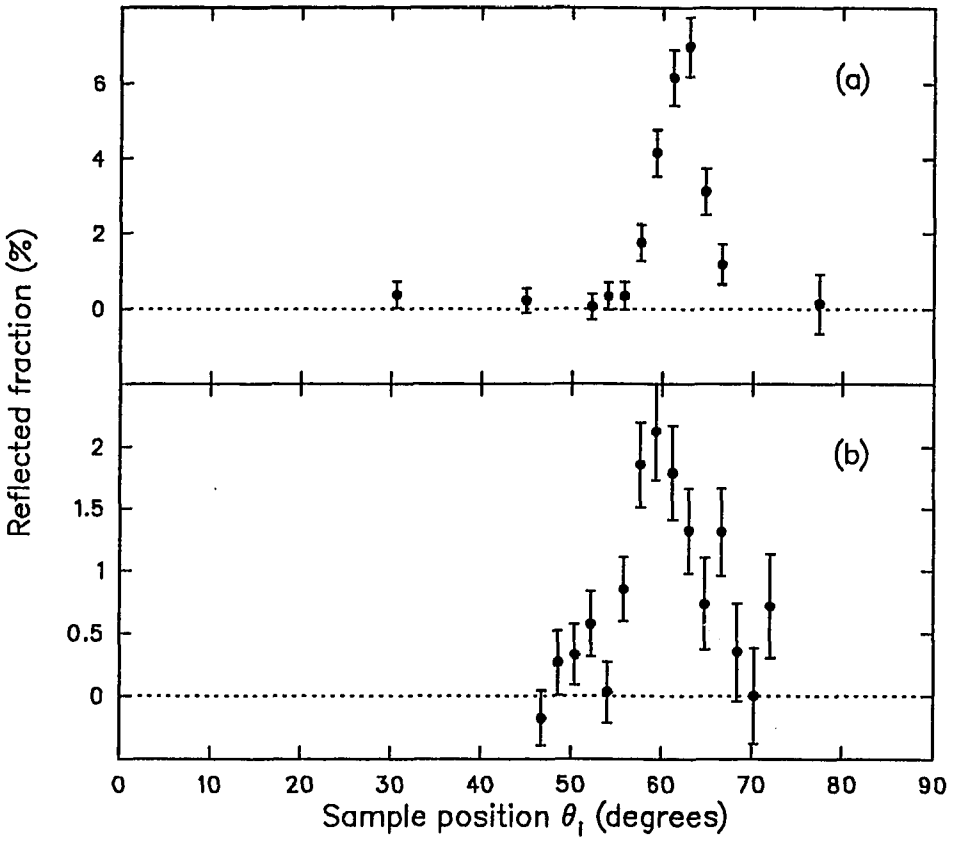

Figure 4.26 — Ps reflection as a function of the sample rotation. The detectors were located at $\psi = 120°$. The Ps beam had an energy of $E_{Ps} = 6.8eV$ in the case (a) and $18.7eV$ in the case (b).

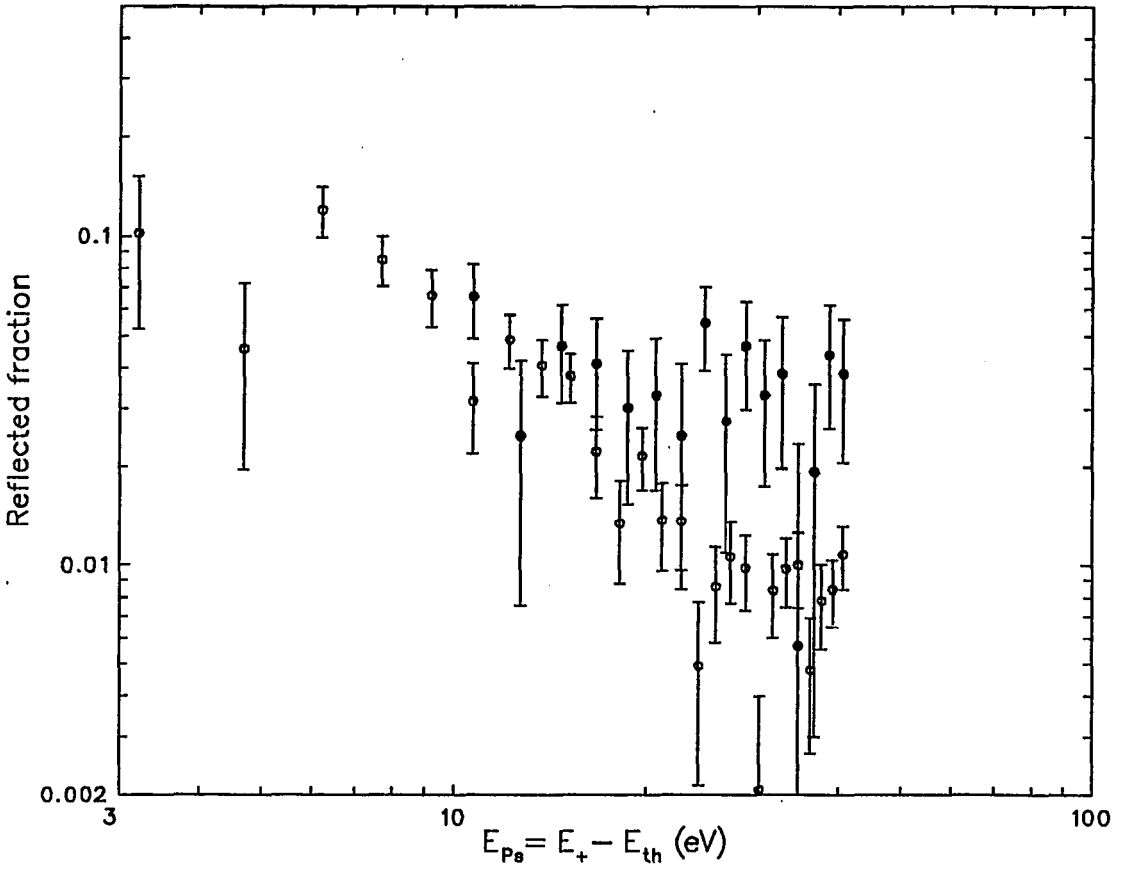

Figure 4.27 — Ps reflection from LiF versus the Ps energy on a log-log scale. The detector was positioned at $\psi = 130°$. In the case of • the sample was very near specular at $\theta_i = 64.8°$. The other measurement (see o) was made with $\theta_i = 70.2°$ off the specular condition. Other than for the 100° data the reflected fractions merge below about $20eV$.

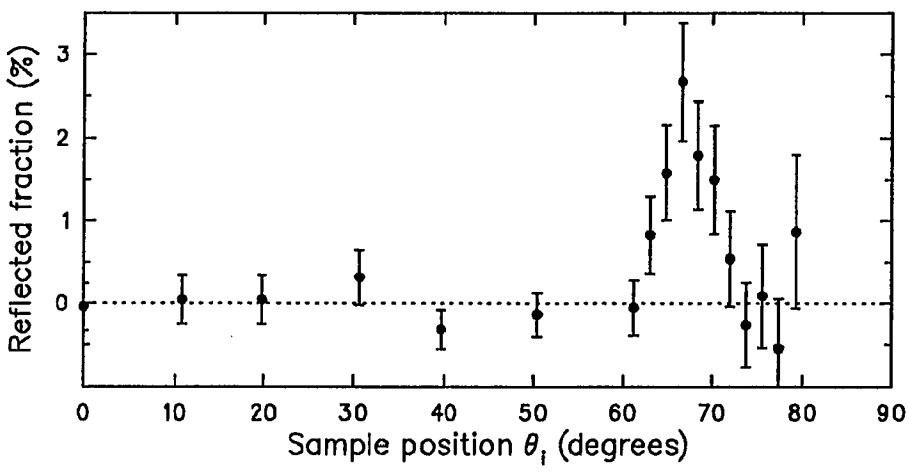

Figure 4.28 — Ps reflection versus the sample angle θ_i. The detector was at $\psi = 130°$. The Ps beam energy in this case was $25.7eV$.

4.3. Theoretical Considerations

One of the next steps after the measurement of a reasonably large reflection coefficient for Ps is to search for diffraction peaks in the data. Some of the measurements display a couple of "wiggles" which might coincide with specular Bragg diffraction peaks. Another possibility is diffraction along the surface of the sample. If Ps is as surface sensitive as one might expect, then this might be the only kind of observable diffraction given the present beam intensity. I made only one measurement to search for this surface diffraction, which turned out to be much too noisy to observe anything. Besides a too weak beam intensity and surface contamination the sample may not be oriented well enough for the diffracted beam to fall in the detector direction.

On the other hand even without the presence of Bragg diffraction the shown energy dependence of the reflection coefficient needs to be explained. In this section I will discuss briefly the attempts to identify any Bragg peaks. In a second part I will present calculations to explain the observed behavior in terms of plane waves reflecting from a potential step which has a complex component.

4.3.1. Diffraction — Following Huyghen's principle a small amount of the incident beam will scatter from each atom. In well defined directions the spherical waves spreading from the atoms interfere constructively and a diffracted beam can be observed in that direction. The Bragg condition describes when this is the case.

$$n = \frac{d}{2\lambda}(cos\theta_i + cos\theta_r), \quad n = 1, 2, 3, ... \tag{104}$$

The angles θ_i and θ_r are those of the incident and reflected beam directions with respect to the sample normal as sketched in figure 4.29. d is the lattice parameter of the sample crystal and λ is the deBroglie wavelength of the incident Ps beam. In all the experiments the sample normal (which coincides with the (100) direction) lies in the plane formed by the Ps beam axis and the detectors.

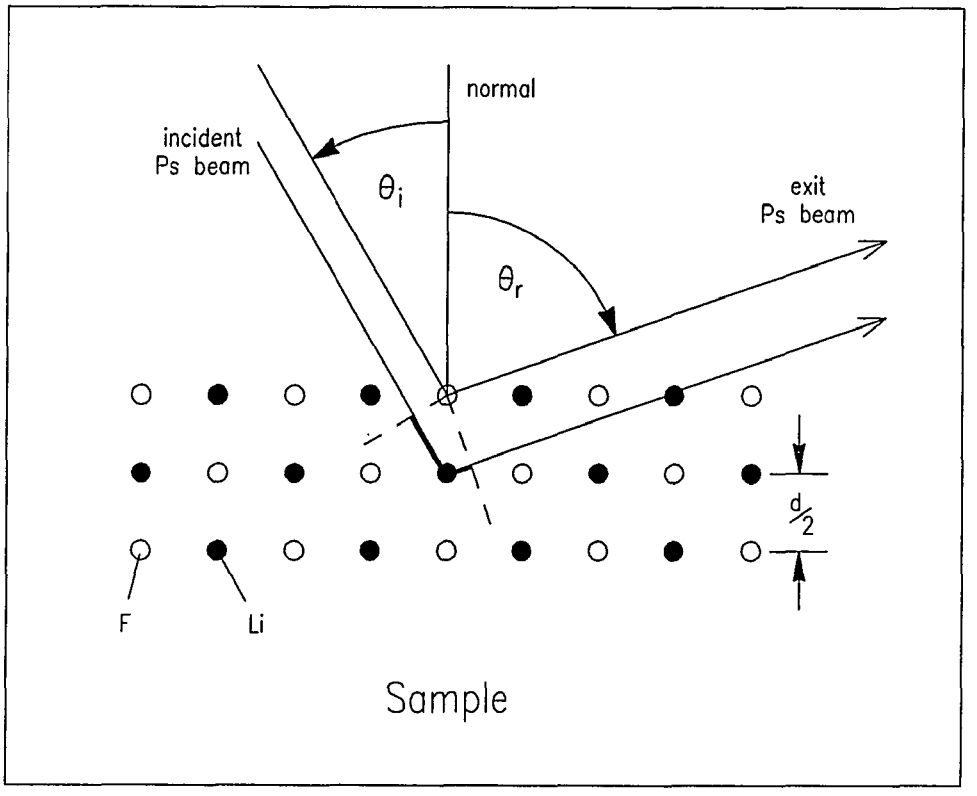

Figure 4.29 — Sketch to define the angles and to illustrate the Bragg condition. The heavy lines represent the additional path of a beam scattering from the second layer. This will result in a phase shift and cause interference.

λ depends on the energy of the Ps atoms.

$$\frac{1}{\lambda} = \frac{\sqrt{2m_{Ps}}}{h}\sqrt{E_{Ps}} \tag{105}$$

Bragg diffraction is expected to be largest for specular conditions when

$$\theta_i = \theta_r = \frac{\psi}{2}. \tag{106}$$

Combining equations (104) to (106) I can evaluate the energies E_n when to expect a diffraction peak of order n as a function of the angle.

$$E_n = \frac{1}{2}n^2 \frac{h^2}{d^2 m_{Ps}} \frac{1}{cos\frac{\psi}{2}} \tag{107}$$

The lattice parameter for LiF is[80]

$$d = 4.02\text{Å} \tag{108}$$

Table 4.7 contains some of the lower order Bragg peak energies for the angles used during some of the measurements. These values are only correct when no inner potential is present. In the case of an inner potential the energies will be shifted by a constant amount to higher energies. It can be determined from the data if two or more peaks are observed. If the lattice parameter is known the measurement of one diffraction peak is enough.

Table 4.7: Energies for Bragg diffraction

	Energy (in eV) for the angle $\frac{\psi}{2} = \theta_i = \theta_r$		
n	50°	60°	65°
1	11.26	18.62	26.06
2	45.05	74.46	104.23
3	101.37	167.54	234.50

Initially the peak in the data for 50.4° specular reflection was assumed to be a diffraction peak. But due to the strongly energy dependent Ps beam intensity the

peak shifted during the normalization and this interpretation proved to be false (see fig. 4.14). No Bragg diffraction could be observed (within the experimental limits of $\approx 2\%$). This may be due to a variety of reasons. Most importantly the surface conditions may not be good enough to permit diffraction. This becomes even more important for surface diffraction which is discussed below. Inelastic reflection may take place and broaden features beyond recognition. This argument can be ruled out because of the relatively sharp specular reflection peaks that I observed during angle scans. I estimate the angular resolution of the detection system to be on the order of 5° which is about the width of the peaks in the angle scans. In such a case the reflected intensity would diminish and a broad background should be observable. Finally the intensity of Bragg diffraction peaks will diminish if the Ps atoms are very surface sensitive and not penetrate the surface much beyond the first layer. Evidence supporting this was found and is discussed in the next section.

Diffraction peaks can also occur when beams scattered from the surface atoms interfere constructively. The condition for this is

$$n = \frac{d}{2\lambda} |sin\theta_i - sin\theta_r| \tag{109}$$

and illustrated in figure 4.30. In the specular case no structure can be expected since the right side of equation (109) will vanish. As for Bragg diffraction the angles will appear in the denominator.

$$\begin{aligned} E_n &= E_0 \frac{4n^2}{(sin\theta_i - sin\theta_r)^2} \\ E_0 &= 4.65eV \quad \text{for Ps and} \quad d = 4.02\text{Å} \end{aligned} \tag{110}$$

Diffraction at lowest energies can be observed when one of the angles becomes small (normal incidence for example) and the other approaches 90° (glancing angle). I made one attempt to observe surface diffraction with $\theta_i = 19.8°$ and $\psi = 98°$. For

this angle combination the lowest order peaks should occur at

$$E_1 = 11.26eV, \quad \text{and}$$

$$E_2 = 45.05eV.$$

The available beam intensity at the time was too low to draw any conclusions.

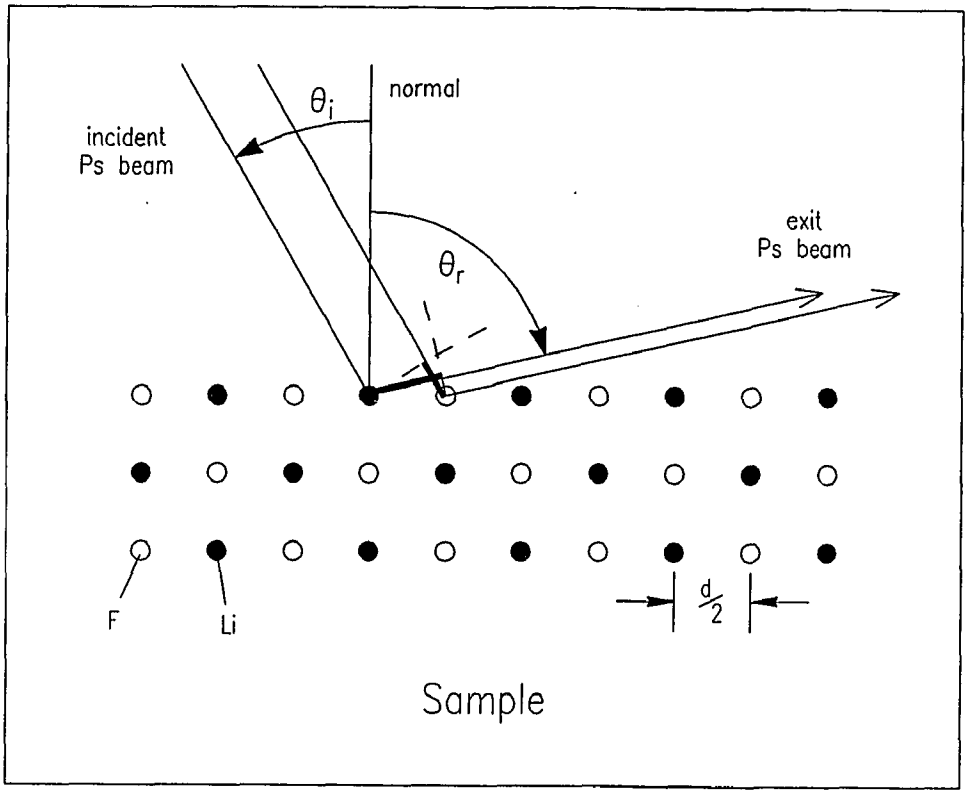

Figure 4.30 — Illustration for surface diffraction. Again the differences in path are accentuated by heavy lines.

4.3.2. Plane waves reflecting from a potential step — I make the very simple assumption that the Ps beam approaches the sample as a plane wave with a total wave vector $\vec{k}_i$ forming the incident angle θ_i with the sample normal. only the normal component will interact with the potential step. In the following I will

regard only the normal component of $\vec{k}_t$. Repeating simple quantum mechanics I start with the one dimensional Schrödinger equation in its time independent form.[81]

$$i\hbar\frac{\partial}{\partial t}\psi_t = -\frac{\hbar^2}{2m}\frac{\partial^2}{\partial x^2}\psi_t + V(x)\psi_t \tag{111}$$

will simplify to

$$E\psi(x) = -\frac{\hbar^2}{2m}\frac{\partial^2}{\partial x^2}\psi(x) + V(x)\psi(x) \quad \text{with} \tag{112}$$
$$\psi_t = \psi(x)exp\{-i\omega t\} \quad \text{and} \quad E = \hbar\omega.$$

I consider a trial potential of

$$V(x) = 0 \quad \text{for} \quad x < 0 \tag{113}$$
$$V(x) = V_r + iV_i \quad \text{for} \quad x \geq 0.$$

Both V_r and V_i should be independent of x. The second order differential equation (equation (112)) has two solutions

$$\psi_1 = exp\{+ikx\} \tag{114}$$
$$\psi_2 = exp\{-ikx\}$$

Outside of the sample where $V(x) = 0$ there is the incident wave of a normalized amplitude and the reflected wave with the amplitude r.

$$\psi = exp\{ik_{out}x\} + r\,exp\{-ik_{out}x\} \tag{115}$$

and k_{out} is determined by

$$k_{out}^2 = \frac{2m}{\hbar^2}E. \tag{116}$$

Since the energy of the Ps beam is real that is also true for the wave vector k_{out}. Here the energy E represents the energy of a Ps atom that only has the momentum component normal to the surface, thus it is not the total energy of the Ps beam E_{Ps}. Inside of the sample the situation is a little more complicated because the

complex part of the potential necessitates a corresponding complex component for the wave vector k_{in}. I assume that only a transmitted wave with amplitude t that moves away from the surface exists. I get

$$\psi = t\, exp\{ik_{in}x\} \quad \text{with} \quad k_{in} = k_{re} + ik_{im}$$
$$\frac{2m}{\hbar^2}\Big(E - V_r\Big) = \Big(k_{re}^2 - k_{im}^2\Big) + i\Big(2k_{re}k_{im} + \frac{2m}{\hbar^2}V_i\Big) \tag{117}$$

The boundary conditions require that the values of ψ and of $\partial/\partial x\ \psi$ inside and outside the surface have to match. That can only be met when

$$r = \frac{k_{out} - k_{in}}{k_{out} + k_{in}}. \tag{118}$$

The reflected intensity R of the emerging plane wave is then

$$R = |r|^2 = \left|\frac{k_{out} - k_{in}}{k_{out} + k_{in}}\right|^2$$
$$= \frac{(k_{out} - k_{re})^2 + k_{im}^2}{(k_{out} + k_{re})^2 + k_{im}^2}. \tag{119}$$

The wave with the complex wave number can also be rewritten as

$$\psi(x) = t\, exp\{-k_{im}x\}\, exp\{ik_{re}x\} \tag{120}$$

The wave decays as the depth into the sample increases. A mean depth λ can be calculated

$$\lambda = \frac{\int_0^\infty dx\ x|\psi|^2}{\int_0^\infty dx\ |\psi|^2} = \frac{1}{2K_{im}} \tag{121}$$

The wave number in equation (119) can be expressed in terms of the energy and the real potential and the imaginary wave number. I solve the equation for the unknown variable k_{im} and get

$$k_{im}^2 = 2\frac{m}{\hbar^2}E\left[\frac{1}{2}\rho^2\Big(1 + \sqrt{1 - 2\frac{V_{re}}{E\rho^2}}\Big) - 1 + \frac{V_{re}}{2E}\right] \tag{122}$$

and

$$\lambda = \frac{1}{2k_{im}}; \quad \text{and} \quad \rho = \frac{1+R}{1-R}. \tag{123}$$

In these calculations I assume that the parallel component of $\vec{k}_{Ps}$ will not change and considered only the normal component. To obtain the value E from the Ps incident on the sample at an angle θ_i with respect from the sample normal I calculate

$$k_{out} = k_{Ps}\, cos\theta_i \quad \text{and} \quad E = E_{ps}\, cos^2\theta_i \tag{124}$$

The mean depth corresponds to a free path of the Ps atom which will continue to move in the original direction to a depth λ over a distance of

$$\lambda_m = \frac{\lambda}{cos\theta_i}. \tag{125}$$

The equations contain one more unknown. That is the magnitude of the real part of the potential step V_r. A trial fit of the reflection data was made by setting the imaginary part of the potential to zero. Then the shape of the reflection function is determined and only the cut off where it becomes energetically possible to enter the sample will be free to adjust. The reflection data do not follow this shape as illustrated in figure 4.31.

In the next step I allow for a complex potential inside the crystal and hold the real part fixed. I assume that it corresponds to the magnitude of a Ps work function, the energy needed (or the energy released if a negative value applies) to move a Ps atom from just under the surface to just above it. This value depends on the material and in general lies around a few eV. As a trial value I assume

$$V_r = 4eV \tag{126}$$

From the measurement with the largest amount of data I calculate the mean free paths λ_m. They are show in figure 4.32. Since the reflection coefficient does not reach unity I assume that only a fraction of the surface is clean enough for the reflection of Ps and normalize the reflection coefficients with their peak value. After an initial rise the mean free path levels off at about 0.75Å. This value is less than

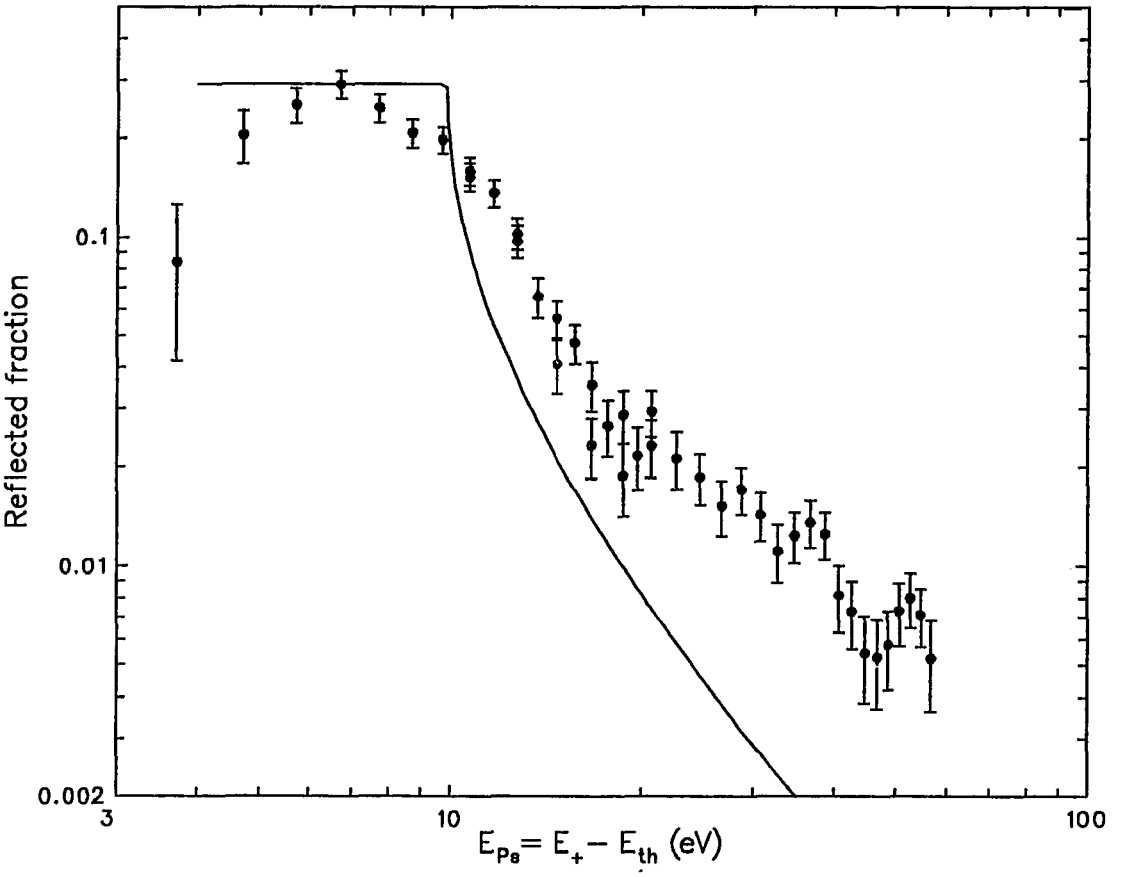

Figure 4.31 — Comparison of the reflection data with the result of plane waves reflecting from a real potential step. The data for specular reflection through 50.4° were used.

the separation of the nearest neighbours in LiF (about 2Å) and very much supports the hypothesis that Ps only interacts with the outermost surface layer. The lack of any Bragg patterns could be explained by this fact.

Whether the "wiggles" near $40eV$ Ps energy are real and if so what causes them will have to wait until more data with better statistics are available. On the other hand I have to bear in mind that the plane wave approach may be over simplifying the problem. The average of the data points for energies above $18eV$ and weighted with their errors is

$$\bar{\lambda}_m = 0.7 \pm 0.02\text{Å} \tag{127}$$

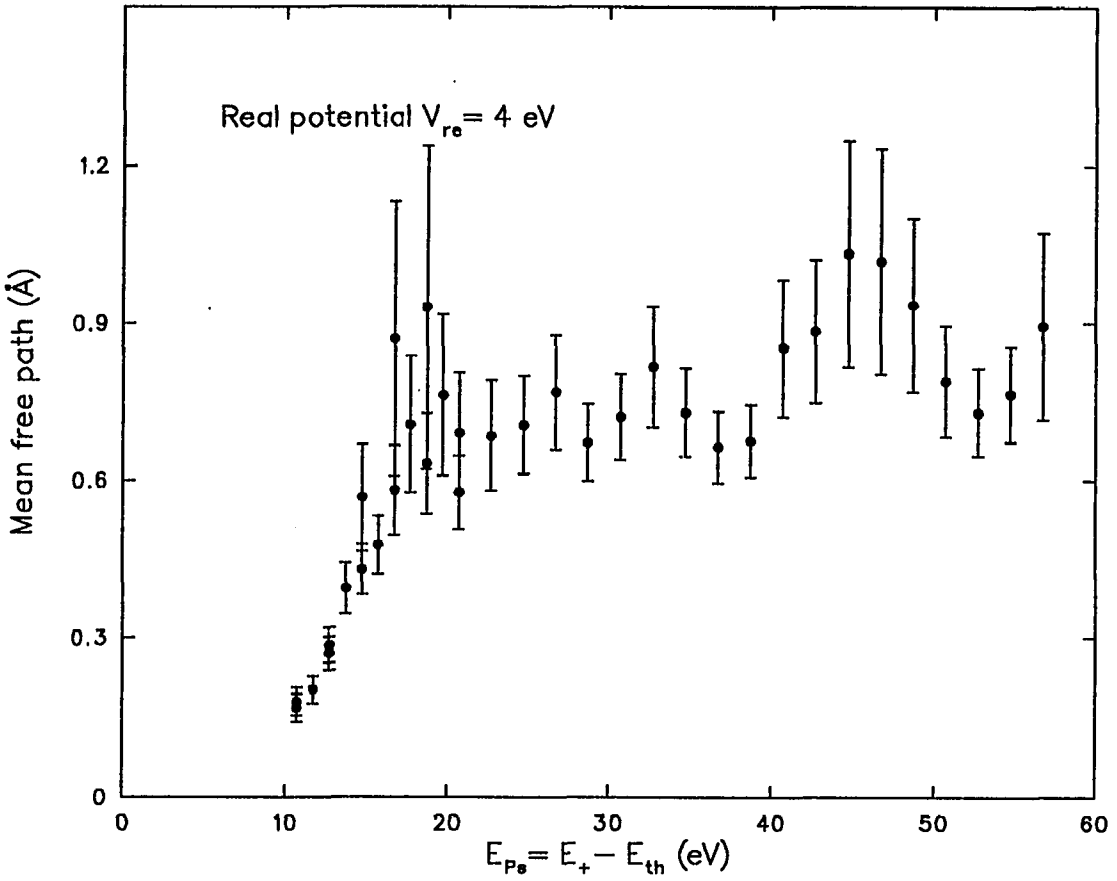

Figure 4.32 — Mean free path λ_m of Ps at the surface of LiF(100) as a function of the Ps beam energy. The values have been calculated from the specular reflection measurements through 50.4° incident angle. The error values stem only from the statistical uncertainties of the original measurements.

and the reduced χ^2 is 0.85 ± 0.25. A fit to a straight line of the same data yields a smaller value for the reduced χ^2.

$$\lambda_m = (0.57 \pm 0.06)\text{Å} + (4.4 \pm 1.7) \times 10^{-3}\text{Å}/eV \times E_{Ps}; \quad \chi^2 = \frac{15.3}{24} \qquad (128)$$

Again the error in χ^2 based on 24 degrees of freedom is about 30%. The fit of linear functions to the mean free path data is shown in figure 4.33 along with the data points. A fit of data is considered to be good when the deviation of the calculated points from the data matches the errors of the data, i.e. the reduced χ^2 should approach unity.

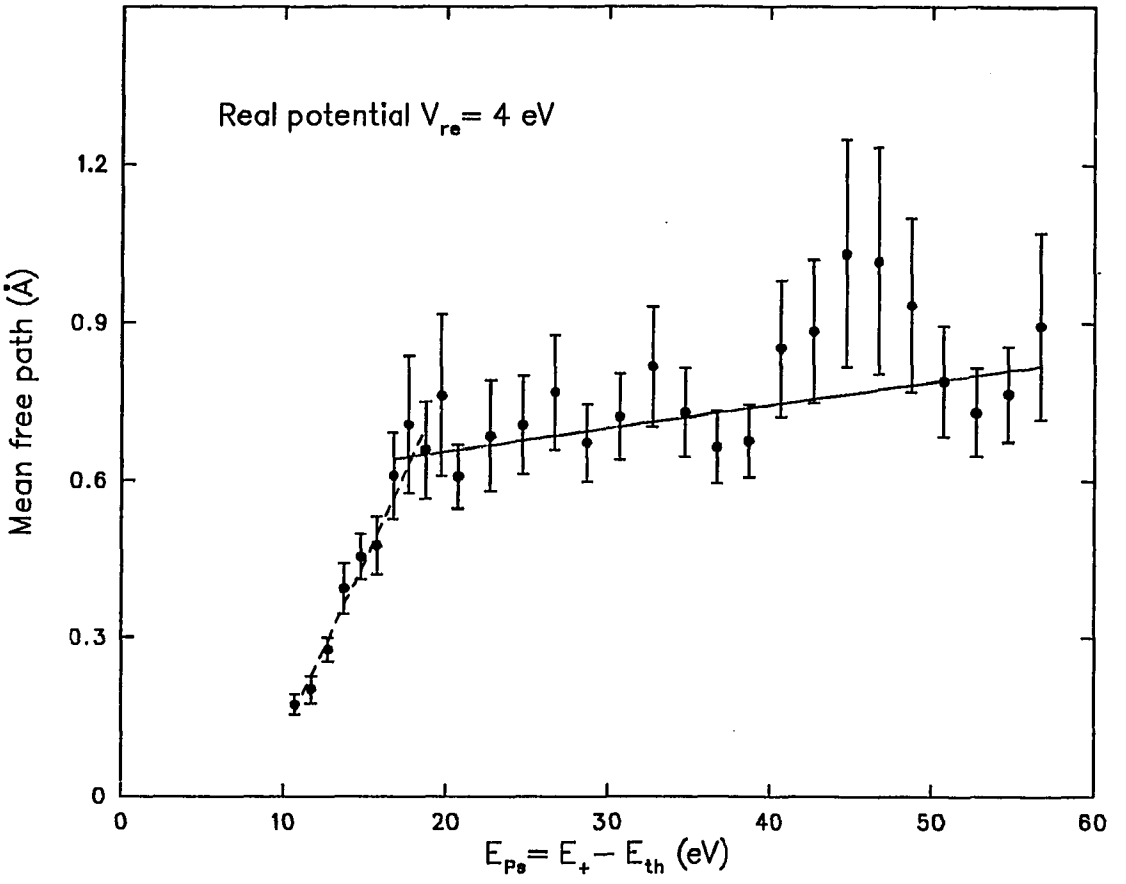

Figure 4.33 — The mean free path as a function of the incident Ps energy. A linear function was fitted to the data below $18eV$ (- - -), and above that energy (—).

Another cause for concern is the absolute value of the real potential V_r. The choice of $4eV$ is somewhat arbitrary. I varied this value and found that the results do not change very much given the present error values when V_r is lowered. Higher values on the other hand (above $V_r = 4.5eV$) will cause the mean free path to increase rapidly. Also more and more data points become inaccessible for these calculations because the normal momentum component becomes too small to overcome the potential step.

The fitted results shown in figure 4.33 can be used to calculate the reflection coefficient. These are shown in figure 4.34 together with the original data and the trial function for a real potential step.

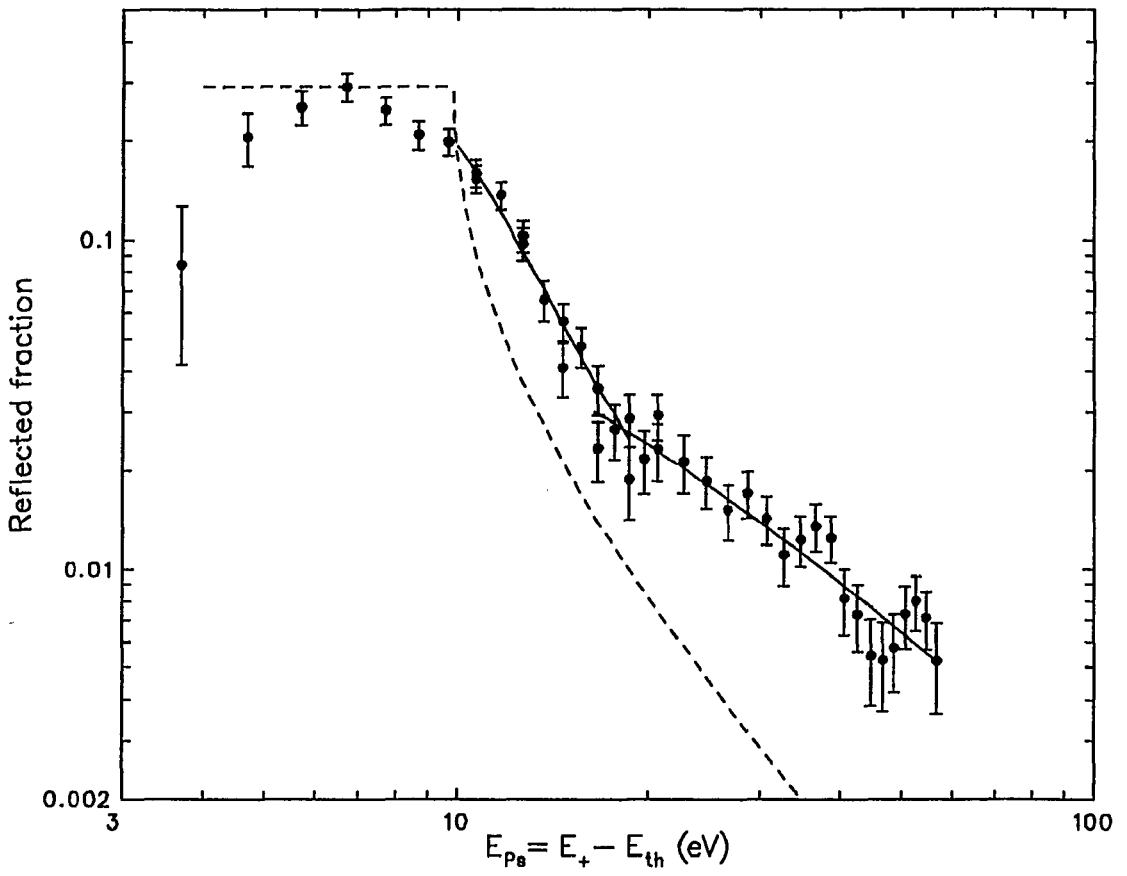

Figure 4.34 — Ps reflection from LiF as a function of the ps beam energy on a log-log scale. Also shown are the two attempts to fit a simple theory of plane waves scattering off a real potential step (- - -) and a complex step (—) to the data.

5. Summary

I have been involved in the development and construction of a high intensity low energy positron beam at the High Flux Beam Reactor (HFBR) at Brookhaven National Laboratory (BNL). The beam was used as the monoenergetic source of positrons for the formation of a beam of positronium atoms. The beam is directed into a differentially pumped cell filled with a gas. Positrons pick up an electron from gas atoms in a transfer reaction to form Ps. This idea was suggested by B.L. Brown[9] and independently realized by a group of scientists in London.[10] I then proceeded to utilize this Ps beam for Ps reflection measurements to investigate the possibility of Ps diffraction experiments.

The idea of simultaneously utilizing the source of positrons as their moderator was implemented into the design of the positron beam. Such a self moderating configuration eliminates the shadowing effect of standard "backscattering" geometries where the thermalized positrons are extracted from the moderator on the source side and have to pass the source holder. The source material consists of high purity copper metal, which has been enriched in the isotope ^{63}Cu. After a two day irradiation in the HFBR with thermal neutrons about one in 4000 atoms have been converted to ^{64}Cu. A fraction of 19% of ^{64}Cu decays to ^{64}Ni while emitting energetic positrons. The remaining atoms either undergo electron conversion or β^- decay to ^{64}Zn. The activated copper is carefully evaporated under high vacuum conditions onto a single crystal of W(110). Epitaxial growth is enhanced for the optimum orientation of Cu (in the Cu(111) orientation) for the moderation process.

Calculations which I presented in the first chapter show that slow positron beam intensities in excess of $10^8 e^+/sec$ can be expected. During a number of runs an intensity on the order of $10^8 sec^{-1}$ has been observed. Unforseen problems with the moderator have reduced this intensity during the Ps beam experiment. It is expected that the implementation of the newly developed solid neon moderator will boost the beam strength back to and beyond the originally expected rate.

The positron beam is optimized for a fixed energy of $150eV$ and directed into a gas cell filled with $10^{-3} torr$ of Ar gas. Differential pumping is achieved with large pumps and small diameter tubes on either side of the cell. The background pressure in the experimental chamber drops to below $10^{-5} torr$. To vary the kinetic energy of the positron beam and thus of the formed Ps the gas cell is floated electrically to various potentials. Depending on the incident energy of the positron beam up to a tenth of a percent of the beam will be converted into a beam of ortho Ps with an angular divergency of 2.5°. Tests showed that the Ps intensity will not increase much further when the Ar pressure is raised.

In the experimental chamber the Ps beam intensity can either be measured directly or as a function of incident and exit angles after reflection from a sample. Thus the reflection coefficient can be evaluated from the ratio of the two measurements. LiF(100) was used as a first sample. Reflected fractions as large as 30% were observed for specular reflection and energies below $15eV$. Beyond that and up to $57eV$, the largest considered energy, 1 to 3% were reflected into the detector which subtends a cone with 2.5° half angle.

At all investigated energies the reflected Ps beam strongly peaks in the specular direction. I performed the experiment for three incident angles (measured from the sample normal) of 50°, 60°, and 65°. All peaks exhibit a FWHM of about 6°, which is not much larger than the cone opening subtended by the detector. I cannot measure the energy of the reflected Ps beam directly but the narrow specular peaks

indicate towards mostly elastic reflection. Inelastic events would spread the beam out and result in a broader angular dependence.

The relatively large reflection coefficient of 1% and the narrow angular dependence strongly encourage a search for diffraction peaks in the data. At present non could be identified. To be observable they need to be larger than 1% of the incident intensity given current statistics. The anticipated large increase in beam intensity will push this limit much lower. On the other hand a simple theory of plane waves reflecting from a potential step at the sample surface yields a mean free depth of Ps of less than 1Å for the studied LiF(100) surface. If that is the case then Ps is indeed a very surface sensitive probe. The investigation of very open structures should become possible.

As I have shown in this work the reflection fraction of Ps from ionic surfaces can be measured with present beam intensities the effort should continue. Many questions remains unanswered. I have indications that the reflection coefficient is not independent from the sample temperature. A raise in Ps reflection with temperature may simply be due to the desorption of contaminants on the surface. R.H. Howell pointed out recently[82] that LiF is a rather unique material among the alkali halides. Consequently Ps reflection from other ionic crystals like NaF needs to be measured. Simple metals and semiconductors are other obvious candidates. The question of Ps diffraction aside the reflectivity for Ps below $5eV$ remains unanswered. Some of my results indicate a drop with lower energies, while the reflected fraction remains constant at a different angle. More data with better statistics are needed in this region.

Eventually it will become necessary to measure the energy of the Ps atoms directly, rather than infer it from the positron energy in the gas cell. A time-of-flight apparatus should be included. Also the angular resolution, which is large at present to increase the efficiency, should be improved. Although less efficient,

other methods of Ps formation should not be ruled out. The beam foil method or the glancing angle method offer the advantage of ultra high vacuum conditions. Also when the positron beam strikes the foil or the surface secondary electrons are released. They can be used to "tag" the Ps beam and thus obtain a start signal for timing experiments. Such a "start" signal can be obtained in the gas cell method, if the positron beam is remoderated in front of the gas cell. This approach was taken by Laricchia *et. al.*[83] I expect exciting results from the work ahead that will enhance our understanding of surfaces in general and on how Ps interacts with them.

References

1. See for example in the collection of lectures in "*Positron Solid-State Physics*", Proc. of E. Fermi School of Physics, Course LXXXIII, ed. by W. Brandt and A. Dupasquier (North Holland, 1983).

2. A.P. Mills, Jr., *ibid.* p.432.

3. I.L. Rosenberg, A.H. Weiss, K.F. Canter, *Phys. Rev. Lett.*, 44, 1139 (1980).

4. K.F. Canter, in "*Positron Scattering in Gasses*", edited by J.W. Humberston, M.R.C. McDowell (Plenum Press, New York, London), p. 219 (1984).

5. W.E. Frieze, D.W. Gidley, K.G. Lynn, *Phys. Rev. B.* 31, 5628 (1985).

6. W. Raith, in "*Positron Scattering in Gasses*", *op. cit.*, p. 1.

7. L.M. Diana, P.G. Coleman, D.L.Brooks, R.L. Chaplin, in "*Atomic Physics with Positrons*", edited by J.W. Humberston, E.A.G. Armour, (Plenum Press, New York, London) p. 55 (1987).

8. For example P. Mandal, S. Guha, N.C. Sil, *J. Phys. B.* **12**, 2913 (1979).

9. B.L. Brown, in "*7th International Conference on Positron Annihilation*", edited by R.M. Singru, P.C. Jain, K.P. Gopinathan, (World Scientific Publ. Co., Singapore), p. 328 (1985).

10. G. Laricchia, M. Charlton, T.C. Griffith, F.M. Jacobsen, in "*Positron (Electron)-Gas Scattering*", edited by W.E. Kauppila, T.S. Stein, J.M. Wadehra, (World Scientific Publ. Co., Singapore), p. 303 (1986).

11. K.G. Lynn, W.E. Frieze, in "*Positron Scattering in Gasses*", *op. cit.*, p. 165.

12. S. Berko, K.F. Canter, K.G. Lynn, A.P. Mills, Jr., L.O. Roellig, M. Weber, in "*7th International Conference on Positron Annihilation*", *op. cit.*, p. 961.

13. A review is given in H. Hoinkes, *Rev. Mod. Phys.* **52**, 933 (1980).

14. For example S. Berko, H. Pendleton, *Ann. Rev. Nucl. Part. Sci.* **30**, 543 (1980).

15. J.B. Pendry in "*Positron Solid-State Physics*" and references therein, *op. cit.*, p. 408.

16. P.J. Schultz, K.G. Lynn, *Phys. Rev. B* **26**, 2390 (1982).

17. B.L. Brown, Ph.D. dissertation (Brandeis University), 1987.

18. C.D. Anderson *Phys. Rev.* **43**, 491 (1933).

19. See for example P.J. Schultz, K.G. Lynn, *Rev. Mod. Phys.* **60**, 701 (1988) and references therein for a discussion of positron beams and solid state research applications of them.

20. D.E. Groce, D.G. Costello, J.W. McGowan, D.F. Herring, *Bull. Am. Phys. Soc.* **13**, 1397 (1968).

21. A.P. Mills, Jr., E.M. Gullikson, *Appl. Phys. Lett.* **49**, 1121 (1986).

22. K.F. Canter, P.G. Coleman, T.C. Griffith, G.R. Heyland, *J. Phys. B*, **5**, L167 (1972).

23. D.M. Chen, K.G. Lynn, R. Pareja, B. Nielsen, *Phys. Rev.* **31**, 4123 (1985).

24. H.E. Hansen, E.S. Linderoth, K. Petersen, *Appl. Phys.* A **29**, 99 (1982).

25. K.G. Lynn, M. Weber, L.O. Roellig, A.P. Mills, Jr., A.R. Moodenbaugh, in "*Atomic Physics with Positrons*", *op. cit.* p.161.

26. R. Engleman, Jr., R.A. Keller, C.M. Miller, N.S. Nogar, J.A. Paisner, *Nucl. Instrum. Methods* **B26**, 448 (1987).

27. R.H. Howell, R.A. Alvarez, in "*Positron Scattering in Gases*", *op. cit.*, p. 155.

28. C.S. Cook, L.M. Langer, *Phys. Rev.* **73**, 601 (1948).

29. A.F. Makhov, Fiz. Tverd. Tela (Leningrad) **2**, 2161 (1960);
[Sov. Phys. Solid State **2**, 1934 (1960)].

30. A.F. Makhov, Fiz. Tverd. Tela (Leningrad) **2**, 2172 (1960);
[Sov. Phys. Solid State **2**, 1942 (1960)].

31. A.F. Makhov, Fiz. Tverd. Tela (Leningrad) **2**, 2176 (1960);
[Sov. Phys. Solid State **2**, 1945 (1960)].

32. M. Mourino, H. Löbl, R. Paulin, it Phys. Lett. **71A**, 106 (1979).

33. A. Vehanen, J. Mäkinen, *Appl. Phys.* **A36**, 97 (1985).

34. In "*Table of Isotopes*", sixth edition, edited by C.M. Lederer, J.M. Hollander, and I. Perlman, (John Wiley & sons, Inc., New York, London, Sydney), p. 198.

35. In "*HFBR Handbook*", S. Shapiro, D.C. Rorer, H. Kuper editors., Informal Report Brookhaven National Laboratory (1983).

36. See for example the review by M. Charlton *Reports on Progress in Physics* **48**, 737 (1985) and references therein.

37. R.J. Drachman, K. Omidvar, J.H. McGuire *Phys. Rev. A* **14**, 100 (1976).

38. P. Khan, A.S. Ghosh *Phys. Rev. A* **27**, 1904 (1983).

39. P. Khan, A.S. Ghosh *Phys. Rev. A* **28**, 2181 (1983).

40. D.W. Gidley, W.E. Frieze, R. Mayer, K.G. Lynn, in "*Positron (Electron)-Gas Scattering*", *op. cit.*, p. 299.

41. D.W. Gidley, R. Mayer, W.E. Frieze, K.G. Lynn, *Phys. Rev. Lett.* **58**, 595 (1987).

42. A.P. Mills, Jr., W.S. Crane *Phys. Rev. A* **31**, 593 (1985).

43. A.P. Mills, Jr. *Phys. Rev. Lett.* **46**, 717 (1981).

44. K.G. Lynn, private communication. Upton

45. M.A. Stroscio *Phys. Lett. C: Phys. Reports* **22**, 215 (1975).

46. A. Rich, *Rev. Mod. Phys.* **53**, 127 (1981).

47. C.N. Yang, *Phys. Rev.* **77**, 242 (1950).

48. A. Ore, J.L. Powell, *Phys. Rev.* **75**, 1696 (1949).

49. J.A. Wheeler *Ann. NY Acad. Sci.* **48**, 219 (1946).

50. C.I. Westbrook, D.W. Gidley, R.S. Conti, A. Rich, *Phys. Rev. Lett.* **58**, 1328 (1987).

51. See for example A.P. Mills, S. Berko, K.F. Canter, *Phys. Rev. Lett.* **34**, 1541 (1975).

52. See also in "*Electronic and Ionic Impact Phenomena*", by H.S. W. Massey, E.H.S. Burhop, H.B. Gilbody, second edition, volume V, (Clarendon Press, Oxford, 1974) p. 3126.

53. G.S. Adkins, *Annals of Physics*, **146**, 78 (1983).

54. Chang Tianbao, Tang Hsiaowei, Li Yaoqing, in "*7th International Conference on Positron Annihilation*", *op. cit.*, p. 212..

55. A.P. Mills, Jr., *Phys. Rev. Lett.* **41**, 1828 (1978).

56. D. Fromme, G. Kruse, W. Raith, G. Sinapius, *Phys. Rev. Lett.* **57**, 3031 (1986).

57. L.S. Fornari, L.M. Diana, P.G. Coleman *Phys. Rev. Lett.* **51**, 2276 (1983).

58. L.M. Diana, S.C. Sharma, L.S. Fornari, P.G. Coleman, P.K. Pendleton, D.L. Brooks, B.E. Seay, in "*7th International Conference on Positron Annihilation*", *op. cit.*, p. 431.

59. L.M.Diana, S.C. Sharma, L.S. Fornari, P.G. Coleman, P.K. Pendleton, D.L. Brooks, B.E. Seay, *ibid.*, p. 428.

60. A brief review of Ps formation cross sections can be found in T.C. Griffith, in "*Positron Scattering in Gasses*", *op. cit.*, p. 53.

61. L.S. Fornari, L.M. Diana, P.G. Coleman, *Phys. Rev. Lett.* **51**, 2276 (1983).

62. L.M. Diana, et.al., in "*Positron (Electron)-Gas Scattering*", *op.cit.*, p.296.

63. S.N. Nahar, J.M. Wadehra, in "*7th International Conference on Positron Annihilation*", *op.cit.*, p. 413.

64. P. Khan, P.S. Mazumdar, A.S. Ghosh *Phys. Rev. A* **31**, 1405 (1985).

65. P. Khan, P.S. Mazumdar, A.S. Ghosh *J. Phys. B: At. Mol. Phys.* **17**, 4785 (1984).

66. T.C. Griffith, private communication, Gent (1988).

67. D. Fromme, W. Raith, G. Sinapius, in "*7th International Conference on Positron Annihilation*", *op.cit.*, p. 333.

68. R.J. Drachman, S. Houston, *Phys. Rev.* **A14**, 894 (1976).

69. B.A.P. Page, *J. Phys. B* **9**, 111 (1976).

70. R.J. Drachman, S. Houston, *J. Phys. B* **3**, 1657 (1970).

71. G. Peach, presented at NATO Advanced Workshop of e^+-gas Collisions in 1984.

72. B.L. Brown, in "*Atomic Physics with Positrons*", *op.cit.*, p. 241.

73. M. Charlton, private communication, Upton (1988).

74. In "*Harshaw Radiation Detectors*" published by Harshaw/Filtrol Partnership, Solon 1984.

75. G. Laricchia, S.A. Davies, M. Charlton, T.C. Griffith, in "*Atomic Physics with Positrons*", *op. cit.*, p. 223.

76. The routine E02BAF in the "*Fortran Library Mark 11*" by the Numerical Algorithms Group, (1984) was used and references in the manual.

77. A theoretical description of splines can be found in "*Numerical Methods*" by G. Dahlquist, Åke Björck, (Prentice-Hall, Inc., 1974), chapter 4.6.

78. S.J. Ward, J.W. Humberston, M.R.C. McDowell, *J. Phys. B.* **18**, L525 (1985).

79. O. Stern, *Naturwissenschaften*, **18**, 391, (1929).

80. For example in "*Solid State Physics*" by N.W. Ashcroft, and N.D. Mermin (Saunders College, Philadelphia 1976), p. 80.

81. See for example in "*Quantum Mechanics*" by C. Cohen-Tannoudji, B. Diu, and F. Laloë (John Wiley & Sons, New York, London, Sydney, Toronto 1977), volume 1 in chapter 1.

82. R.H. Howell, in "*8th International Conference on Positron Annihilation*" in Gent, 1988 (to be published by World Scientific Publ. Co., Singapore), and in the program and abstracts of the conference, poster C18. They pointed out that LiF exhibited a different behavior from other alkali halides. The Ps energy and angular distributions was measured when the surfaces are bombarded with monoenergetic positrons.

83. G. Laricchia, S.A. Davies, M. Charlton, T.C. Griffith, *J. Phys. E.*, **21**, 886, (1988).